



THE HONG KONG  
POLYTECHNIC UNIVERSITY

香港理工大學

Pao Yue-kong Library

包玉剛圖書館

---

## Copyright Undertaking

This thesis is protected by copyright, with all rights reserved.

**By reading and using the thesis, the reader understands and agrees to the following terms:**

1. The reader will abide by the rules and legal ordinances governing copyright regarding the use of the thesis.
2. The reader will use the thesis for the purpose of research or private study only and not for distribution or further reproduction or any other purpose.
3. The reader agrees to indemnify and hold the University harmless from and against any loss, damage, cost, liability or expenses arising from copyright infringement or unauthorized usage.

### IMPORTANT

If you have reasons to believe that any materials in this thesis are deemed not suitable to be distributed in this form, or a copyright owner having difficulty with the material being included in our database, please contact [lbsys@polyu.edu.hk](mailto:lbsys@polyu.edu.hk) providing details. The Library will look into your claim and consider taking remedial action upon receipt of the written requests.

ELECTROMAGNETIC TRANSIENT  
ANALYSIS FOR LIGHTNING STRIKES ON A  
GROUNDED STRUCTURE

YUXUAN DING

PhD

The Hong Kong Polytechnic University

2020

**The Hong Kong Polytechnic University**

**Department of Building Services Engineering**

**Electromagnetic Transient  
Analysis for Lightning Strikes on a  
Grounded Structure**

---

**YUXUAN DING**

**A thesis submitted in partial fulfilment of the requirements for the degree  
of Doctor of Philosophy**

**JUL, 2020**

## CERTIFICATE OF ORIGINALITY

I hereby declare that this thesis is my own work and that, to the best of my knowledge and belief, it reproduces no material previously published or written, nor material that has been accepted for the award of any other degree of diploma, except where due acknowledgment has been made in the text.

Signed:

Name of Student: YUXUAN DING

# Abstract

thesis entitled: Electromagnetic Transient Analysis for Lightning Strikes on a Ground Structure

Submitted by : Yuxuan Ding

For the degree of : Doctor of Philosophy

Lightning is a powerful natural phenomenon. It could cause fatal casualties, severe damage to the facilities, and mal-function of electrical or electronic systems. Lightning protection, therefore, is imperative for the facilities and systems on the ground. To design efficient and effective protection measures, transient analysis, and evaluation of lightning strikes on a ground structure is considered essential.

This thesis firstly introduces an extended time-domain traveling-wave (TDTW) theory which can be applied to the lightning transient analysis. It is based on the wave equation for scalar potential and vector potential and the retarded Green's equation. The traditional traveling wave theory assumes the constant impedance and reflection coefficient of the transverse electromagnetic (TEM) traveling wave. This is not in coincidence with the non-TEM propagating behavior of the lightning current surge along the lightning path. The proposed TDTW theory introduces time-and-spatial-variant impedance and time-variant reflection coefficient in a simple format. Furthermore, the traveling waves can be divided into primary waves and secondary waves in the presence of discontinuities or lumped circuit elements. The overall solution is simple and analytical under the ramp waveform source. To adapt it to arbitrary waveform excitation, a convolution technique is adopted. The TDTW theory would benefit in constructing a more reasonable lightning engineering model to obtain the corresponding lightning-induced electromagnetic field. Meanwhile, the TDTW theory can be used in determining the transient of a traveling wave antenna with lumped loading.

This thesis also proposes a novel lightning electromagnetic model, which is the hybrid model of distributed circuit (DC) model and the partial element equivalent circuit (PEEC) method. It is well known that most of the physical characteristics of the lightning channel evolution can be reproduced by the DC model in the simplest way, while the electrical circuit behavior of complicated wire ground systems can be dealt with by the PEEC method. Thus, this hybrid electromagnetic and circuit model can be used to model the physical behavior of the lightning channel and the circuit characteristics of a complicated ground structure together. Most recently, the physical dynamic characteristics of the lightning corona effect are well established. Thus, in this thesis, the existed DC model is extended to include the non-linear and non-uniform behavior of the dynamic corona effect. Meanwhile, because the initial charge also plays an important role in the physical evolution, the modified charge simulation method (CSM), which is modified to involve the dynamic corona effect, is proposed to obtain the initial charge distribution beneath the thundercloud. The modified CSM is solved with Newton's iterative method. The hybrid electromagnetic and circuit model is solved with Piecewise Linearization (PL) Method and march on-in-time technique. The simulation results are well matched with the experimental measurement data. This model exhibits the influence of various ground structures and dynamic corona effect on the lightning current surge and corresponding LEMP.

In general, this thesis proposes an extended traveling wave theory and a hybrid electromagnetic and circuit model. Both can be used in lightning strikes on a ground structure issue. The former is of simple and closed-form expression and would benefit from giving a more reasonable engineering model. The latter is based on the electromagnetic numerical method and aims at proposing a novel electromagnetic model to include both the physical behavior and circuit characteristics of a lightning strike. The choice of an appropriate model highly depends on the research objective and specific engineering application.

# Publications

## I. Papers in Journals

- Y. Du and Y. Ding, "Lightning Surge Propagation on a Single Conductor in Free Space," in IEEE Transactions on Electromagnetic Compatibility, vol. 59, no. 1, pp. 119-127, Feb. 2017.
- Y. Ding, Y. Du and M. Chen, "Lightning Surge Propagation on a Ground Vertical Conductor," in IEEE Transactions on Electromagnetic Compatibility, vol. 60, no. 1, pp. 276-279, Feb. 2018.
- Y. Ding, Y. Du and M. Chen, "Extended Traveling Wave Theory for the Multi-stage Tower under a Direct Lightning Strike," Sent to IEEE Transactions on Electromagnetic Compatibility.

## II. Papers in Conferences

- Y. Ding and Y. Du, "Surge behavior on the single conductor with a discontinuity," 2016 33rd International Conference on Lightning Protection (ICLP), Estoril, 2016, pp. 1-5.
- Y. Ding, Y. Du, and M. Chen. "Surges on a vertical conductor excited by current and voltage sources." The 10th Asia-Pacific International Conference on Lightning, Krabi, Thailand, 16-19 May 2017.

# Acknowledgements

Firstly, I would like to express my sincere gratitude to my supervisor Prof. Du Yaping for his dedication and guidance. His suggestions, feedback, discussions, and support company me throughout all my study period at PolyU. I always enjoy academic exploration during this period, my precious period of life.

Then, I would acknowledge Prof. Chen Mingli for his kind encouragement and support during my research. I have discussed with him a lot of times on the research work presented in Chapter Four of this thesis. His broad and profound physical knowledge helps to shape my research results.

Also, I would like to appreciate my research team members: Qi Ruihan, Li Binghao, Zhang Yang, Cao Jinxin, Chen Hongcai, Lyu Jiahua, and Zhao Sihan. My time at PolyU has been lightened and enhanced by all the friends I have met. I would thank Qi Ruihan for the programing help on the PEEC code. I also like to thank Li Binghao for providing the FDTD simulation code. This gives me a lot of convenience in simulating the lightning transients. Zhang Yang helped me with the software simulation on practical simulations. Cao Jinxin, although comes to HK most recently, provides me a lot of help on the software.

Finally, I would like to thank my parents. As for now, I have been living in Hong Kong for seven years. They have provided the strongest backup and support to me during this long and precious time in my life.

# Table of Contents

CERTIFICATE OF ORIGINALITY .....	3
1. Introduction.....	10
1.1 Background.....	10
1.2 Lightning Strikes on Ground Structures .....	11
1.3 Objectives .....	13
1.4 Thesis Outline .....	14
2 Literature Review: Lightning Strikes on Ground Structures .....	16
2.1 The Electromagnetic Numerical Computation Methods.....	16
2.1.1 <i>The Partial-element-equivalent-circuit (PEEC) method</i> .....	16
2.1.2 <i>The other numerical methods</i> .....	20
2.2 Physical Mechanism of Lightning Strikes on Ground Structure .....	21
2.3 Modeling of Lightning Strikes on Ground Structures .....	22
2.4 The Traditional Traveling Wave Theory .....	23
3 The Extended Time Domain Traveling Wave Theory.....	28
3.1 The General Time-Domain-Traveling-Wave (TDTW) Theory .....	28
3.2 The Solutions of the Non-TEM Propagating Wave.....	36
3.3 The Time-and-space-varied Impedance for Arbitrary Current Waveform 43	
3.4 The Response Transfer under Arbitrary Source Voltage/Current Waveform .....	46
3.5 The Extended TDTW Theory for a Grounded Vertical Structure .....	47
3.6 The Extended TDTW Theory for a Conductor with a Discontinuity .....	54
3.7 The Extended TDTW Theory for a Grounded Multi-level Tower .....	63
3.8 Applications .....	70
3.8.1 <i>Dipole antenna with a lumped loading</i> .....	70
3.8.2 <i>Lightning strikes on a two-stage tower on the ground</i> .....	77

3.9	Conclusion .....	81
4	The Integrated Model for Lightning Strikes on Ground Structures .....	82
4.1	The Enhanced DC Model for Lightning Return Stroke with Dynamic Corona Discharge .....	82
4.2	The Integrated Model.....	85
4.3	Applications .....	94
4.4	Conclusions.....	99
5	Conclusions and Future work .....	100
5.1	Conclusions.....	100
5.2	Future Work.....	100
	<b>Appendix.....</b>	<b>115</b>
	<b>Appendix A The Relationship between Current and Scalar Potential .....</b>	<b>115</b>
	<b>Appendix B Lossless Propagation of Potentials .....</b>	<b>117</b>
	<b>Appendix C Wave Propagation in a Dipole Line Structure with Different Radius .....</b>	<b>118</b>
	<b>Appendix D Wave Propagation in a Multiple Dipole Line Structure .....</b>	<b>119</b>
	<b>Appendix E Transient Impedance of Wave Propagation in a Multi-stage tower .....</b>	<b>122</b>
	<b>Appendix F The Lumped Capacitance Considering the Nonlinear and Dynamic Corona Sheath.....</b>	<b>125</b>

# 1. Introduction

## 1.1 Background

Lightning is a powerful natural phenomenon. It is often classified into cloud discharges and cloud-to-ground (CG) discharges, both accompanied by strong flashes and loud noises [1,2]. The cloud discharges include intracloud, intercloud, and cloud-to-air discharges. It is mentioned in [3] that cloud discharges are generally considered to have little influence on the human being or other objects on the ground. It is the CG discharges that have a significant threat to the human being and facilities. It may cause casualties, forest fires, the malfunction of electrical systems. The peak value of the pulse current released by lightning is up to hundreds of kilo amperes and generates powerful electromagnetic pulses. The high peak pulse current and powerful electromagnetic pulses are extremely destructive to various objects, especially microelectronic devices. In China, the economic loss caused by the lightning hazard exceeds hundreds of millions of yuan and the number of casualties caused by lightning is more than thousands each year [4].



Figure 1.1 The ground objects hit by lightning flash

Lightning protection, therefore, is imperative for the facilities and systems on the ground. To design efficient and effective protection measures, evaluation of lightning transients in the structures and systems on the ground is considered essential.

It is well known that the presence of a vertically extended and grounded structure in the lightning discharge path can appreciably influence the lightning current waveforms and consequently the radiated electromagnetic fields. In addition, electrical characteristics of a lightning channel may influence the current and voltage distribution at the lightning striking object, such as a wind turbine system or a power system. These issues have significant meaning in both lightning science research and lightning protection engineering.

This thesis gives a specialized theory for lightning surge propagation and a technical solution for lightning transients on complicated ground structures.

## **1.2 Lightning Strikes on Ground Structures**

In the middle of the 18th century, Benjamin Franklin firstly used scientific methods to study lightning and discovered that lightning was a discharge phenomenon. Until now, researchers have been measuring and recording natural lightning with equipment installed in tall structures on the ground. The research not only includes the study of lightning evolution mechanism and characteristics, but also the measurement of lightning parameters and lightning-induced electromagnetic fields.

By comparing the measurement observation data and the electromagnetic simulation results, it is beneficial for researchers to obtain a deeper insight into the lightning phenomenon and understanding the interaction between lightning channel and ground structures. Thus, the electromagnetic transient study of lightning strikes on tall ground structures are of great significance in lightning science research.

On the other hand, the tall structure is the major object for lightning protection against economic loss and casualties. According to the lightning electromagnetic

wave path, the lightning effect for lightning protection engineering and lightning science research is divided into direct lightning and indirect lightning.

In an indirect lightning strike, the resultant current propagating on a tower could be a significant source in the evaluation of lightning-induced electromagnetic pulses (LEMP) [8-9]. Such LEMP may induce transient voltages and currents on overhead lines, underground lines, and wiring systems in buildings, and may cause damages or malfunction of electrical and electronic equipment connected as well. The correct current distribution along the lightning path, therefore, is indispensable in lightning-induced transient analysis. In a direct lightning strike, the lightning current surge propagates both upward along the lightning channel and downward along the tall structure. This instantaneous high current is very likely to cause damages to electrical and electronic equipment as well as the safety of the human being.

In a word, the lightning strikes on ground structures have considerable significance in both academic research and practical applications. However, the research of lightning strikes on ground structures began most recently and is far from fully developed.

The theoretical analysis of the lightning surge in the overhead horizontal lines is made with the traditional transmission line (TL) theory. This TL theory is widely used in the power system because of its especially convenience and clear physical meaning. However, for lightning strikes on ground structures, the traditional TL theory, which is based on the TEM assumption of wave, is no longer valid. A specialized theory shall be developed to study the traveling characteristics of the non-TEM wave in such structures.

Besides the theoretical establishment, numerical simulation is also of great significance in lightning research. Several models have been proposed recently including the antenna theory model, hybrid electromagnetic model distributed circuit model, and macroscopic model. These models are beneficial in the transient electromagnetic study of lightning strikes on ground structures. However, it is found that although the Partial-element-equivalent-circuit model has the advantage to consider more complex and practical EMC problems during a direct lightning strike [10], it is not applied yet for the simulation and study of lightning strikes on ground structures. On the other hand, the physical evolution of lightning is not fully considered in the modeling.

Thus, from the view of both specific theory establishment and realistic numerical simulation, the research for lightning strikes on ground structures shall be developed.

### 1.3 Objectives

This thesis aims at addressing the issues of lightning strikes on ground structures, and the specific non-TEM time-domain traveling wave theory. An integrated modeling method is developed to consider a more realistic lightning physical evolution and complicated ground structures for transient analysis.

The objectives of this thesis are shown below:

1. To develop a specific traveling wave theory, called time-domain-traveling-wave (TDTW) theory for describing the propagation of a lightning surge along vertical lines above the ground. The TDTW theory provides both the theoretical establishment and analytical expression for the non-TEM traveling wave problem. This theory aims at formulating the non-TEM traveling wave characteristics for a single conductor, multiple parallel-connected conductors, and discontinuities on the conductors, such as lumped loading, grounding, and multi-level structures, under a lightning strike. Note that the characteristics of such lines may vary with input waveform, a corresponding convolution technique is developed for evaluating the solution under arbitrary input source/voltage waveform.

2. To give a further development on the interaction between a realistic physical lightning channel and complicated ground structures in this thesis, i.e., an integrated model. The integrated model is based on the advanced distributed circuit (DC) model and the PEEC method. The integrated model includes both the comprehensive modeling of lightning physical evolution and a large-scale complicated ground structure at the same time. The calculated lightning radiated electromagnetic field and lightning current waveform are compared with the measurement observation result for verification.

The contribution of this thesis is summarized as follows:

- a) A novel time-domain traveling wave (TDTW) theory

By recognizing the deficiency of traditional traveling wave theory, the TDTW theory is developed for the 1st time to settle the problem of non-TEM traveling

waves along wire structures. The specially defined impedance is introduced for the 1st time to consider both the attenuation and distortion of the traveling wave. The discontinuity problem of non-TEM traveling wave is tackled with a time-variant reflection coefficient and a fictitious secondary current source. This theory is further developed for applications in a multi-conductor multi-level structure above the ground. The overall analytical expression is simple and accurate.

The phenomena of non-TEM traveling waves are widely observed in lightning surge propagating along vertical structures, such as a multi-stage tower, or a long wire antenna. This theory has been applied to address the electromagnetic transients and the non-TEM traveling wave behavior in a two-stage tower under a lightning stroke and the lumped loading long wire antenna under the voltage source excitation.

b) A novel integrated model for lightning strikes on complicated ground structures

This integrated model gives a further development on the interaction between the lightning channel and ground structures. The recent research results in lightning observation studies are included in the lightning channel model using the extended DC model. Meanwhile, the complicated ground structures are modeled with the PEEC method. This integrated model is intended to use for transient analysis in a system with a realistic lightning channel and complicated ground structures.

For the practical application, this integrated model is used to determine the lightning transients in a typical commercial house and a wind turbine system.

## **1.4 Thesis Outline**

The body of the thesis is structured as follows:

In Chapter 2, the literature review of lightning strikes on ground structures is given. This includes the analytical methods of lightning transient simulation, the physical mechanism of lightning strikes on ground structures, the modeling of lightning strikes on ground structures, and the traditional traveling wave theory.

In Chapter 3, the time-domain-traveling-wave (TDTW) theory is introduced. Similar to the traditional traveling wave theory, it is used to describe the propagation

of non-transverse-electromagnetic-mode (non-TEM) waves on a line structure. The scalar potential and vector potential are used to describe the characteristics of traveling waves. The specially introduced impedance is first evaluated under a ramp current source and then is extended to the arbitrary current/voltage source waveform. Then, the discontinuity issue of a non-TEM traveling wave is settled by introducing the time-variant reflection coefficient. The TDTW theory is also extended to a multi-conductor structure above the ground. The applications of the TDTW theory include the lightning transients in a multi-level tower above the ground and the transient analysis of the lumped-loading dipole antenna.

In Chapter 4, to model a complicated ground structure and the physical behavior of a lightning channel at the same time, an integrated model for the lightning channel and ground structures is proposed. It is based on the enhanced distributed circuit (DC) model and partial equivalent element circuit (PEEC) method. The initial charge distribution and the dynamic behavior of the corona sheath are included in the integrated model with the most recent research results on lightning corona discharge. As the dynamic corona discharge demonstrates the significant nonlinear behavior, the piecewise-linearization (PL) method combined with the march-on-in technique is used to solve the modified-nodal-analysis (MNA) matrix of PEEC. The vector fitting method is used to include the frequency-dependent effects and the quasi-static Green's function is applied to consider the effect of the lossy ground. This integrated model can be used to modeling the physical behavior of the lightning channel and the large-scale complicated ground objects together. It may give a tool for further study on the influence of various ground structures on the lightning current propagation behavior along the lightning channel, as well as the influence of lightning physical characteristics on the lightning current and voltage distribution along the ground structures. The application of this model is the lightning transient analysis of lightning strikes on a commercial house or a wind turbine system.

In Chapter 5, the conclusion and the future work of this thesis are presented.

# 2 Literature Review: Lightning Strikes on Ground Structures

In this chapter, the literature review of lightning strikes on ground structures are presented. It includes the general electromagnetic numerical method used in lightning protection engineering, the physical mechanism of lightning strikes on a ground structure, the existing model of lightning strikes on ground structures, and the traditional traveling wave theory.

## 2.1 The Electromagnetic Numerical Computation Methods

### 2.1.1 *The Partial-element-equivalent-circuit (PEEC) method*

The PEEC method was firstly proposed by E. Albert for extracting the lumped inductance and capacitance of the ultra-large-scale integrated circuit (VLSI) in the 1970s [11]. Based on this method, the acceleration calculation of inductance and capacitance was introduced for arbitrary three-dimensional structures [12]. The PEEC method can be applied from dc to extra-high frequency determined by the meshing. Using the PEEC method, the complicated electromagnetic problem can be transferred into the circuit domain. The equivalent circuit formulation can be easily constructed using modified nodal analysis (MNA) formulation and then be solved in the time or frequency domain, for example, SPICE. Another advantage of MNA formulation is that any type of circuit elements can be included directly into the solver of PEEC. The PEEC method is also efficient in solving non-orthogonal geometries. All these advantages lead to its wide applications in electromagnetic transient simulation in complex structures. Thus, with this PEEC model, it is possible to consider more complex and practical EMC problems [13], particularly the wire-structure problems.

In 1989, Milson proposed the non-orthogonal PEEC model in the simulation of the printed circuit board (PCB). This research shows the advantage and efficiency of PEEC in the simulation of non-orthogonal geometry [14]. In 1992, Ruehli introduces the time retardation effect into the PEEC model [15]. Then, the original

PEEC method is enhanced to obtain a full wave solution. Note that for the small electrical geometry size problem, it is found in [15] that the PEEC method can be approximated by a quasi-static model, which gives an approximately accurate result compared with the full-wave solution but significantly improves the algorithm efficiency. The following is the summary of the PEEC method, which is applied for the lightning transient analysis presented in this thesis.

### 2.1.1.1 PEEC model in the air

The formulation of the PEEC model is based on the mixed potential integral equation (MPIE). The electric field is expressed with scalar potential  $\phi$  and vector potential  $A$ , as follows:

$$E(r) = -j\omega A(r) - \nabla\phi(r) \quad (3.1.1)$$

Both vector potential  $A$  and scalar potential  $\phi$  can be expressed with charge  $\rho$  and current  $I$  using the free-space Green's function:

$$\begin{aligned} A(r) &= \frac{\mu_0}{4\pi} \int_{l'} G_0(r, r') I(r') dl' \\ \phi(r) &= \int G_0(r, r') \cdot \rho(r') dl' \end{aligned} \quad (3.1.2)$$

where  $G_0(r, r') = \frac{e^{-jk(r-r')}}{|r-r'|}$  is the free-space Green's function and  $k = j\omega\sqrt{\mu_0\epsilon_0}$  is

the free-space wavenumber.

Dividing the conductors into segments then substituting (3.1.2) into (3.1.1) yields the PEEC model for one segment,

$$\frac{l_i}{\sigma a} J_i + \sum_j j\omega \int_{l_i} \int_{l_j} G_0(r, r') dl'_j dl_i \cdot I_j = \phi_n - \phi_m$$

The inductance and capacitance of the PEEC model are defined as the following expression:

$$L_{ij} = \frac{\mu_0}{4\pi} \int_{l_i} \int_{l'_j} G_0(r, r') dl_i \cdot dl'_j$$

$$p_{nm} = \frac{1}{4\pi\epsilon_0} \frac{1}{\Delta l_n \Delta l_m} \int_{l_n} \int_{l'_m} G_0(r, r') dl_n dl'_m$$

Table 2.1 Expressions of PEEC elements

Partial Element Type	Partial Element Expression
Resistance	$R_i = \frac{l_i}{\sigma_i a_i}$
Inductance	$L_{ij} = \frac{\mu_0}{4\pi} \frac{1}{a_i a_j} \int_{v'} \int_{v'} \frac{1}{R} dV_i \cdot dV_j$
Coefficients of potential	$p_{nm} = \frac{1}{4\pi\epsilon_0} \frac{1}{S_n S_m} \int_{S_n} \int_{S_m} \frac{1}{R} dS_n dS_m$

With the partial inductance, capacitance, and resistance, the equivalent circuit of a line segment can be drawn as shown in Fig.2.1. The elements are found in Table 2.1.

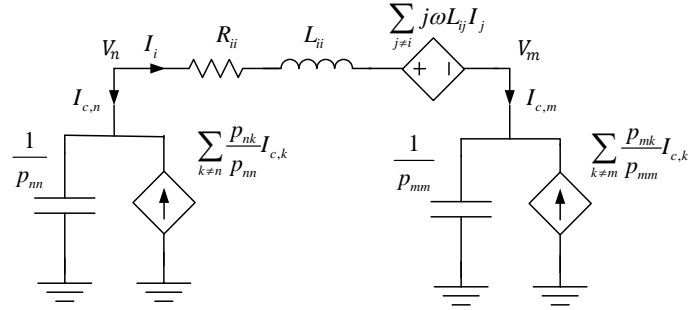


Figure 2.1 Equivalent circuit of a line segment

### 2.1.1.2 PEEC model above the lossy ground

The ground object is generally represented with a wire-grid structure during a lightning strike. Such a wire structure can be efficiently modeled by using the PEEC method proposed in [16].

Both vector potential  $A$  and scalar potential  $\phi$  for the segment above the ground can be expressed using Green's function as:

$$\begin{aligned}
A(r) &= \frac{\mu_0}{4\pi} \int_V \bar{\bar{G}}_A(r, r') I(r') dl' \\
\phi(r) &= \frac{1}{4\pi\epsilon_0} \int_S K_\phi(r, r') \rho(r') dv' + \int_{V'} C_\phi(r, r') I(r') dl'
\end{aligned} \tag{1}$$

where  $I(r')$  and  $\rho(r')$  are the conductor current and charge density.  $\bar{\bar{G}}_A(r, r')$  is the dyadic Green's function.  $K_\phi(r, r')$  are the scalar Green's function for electric potential and a correction term  $C_\phi$  arising from the z component of the current is introduced [17].

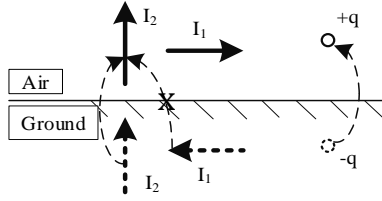


Fig. 2.2 Source current and charge and their images for two ground models: Low-frequency ground (LFG model)

It is noted in [18] that the configuration of the PEEC method with ground images is shown in Fig. 2.2. It is also known that the ground effect is ignorable in a high position. Therefore, the ground model presented in Fig. 2.2 is adopted for modeling the ground structure in the time-domain simulation. Therefore, circuit parameters consist of the contributions from the component in air and their images. With these lumped elements, one typical segment of the PEEC equivalent circuit is constructed. Fig. 2.1 shows the lumped circuit in a segment of the conductor.

Then the modified node analysis (MNA) matrix for the PEEC method is written as:

$$\begin{bmatrix}
A & -\left(R + L \frac{\partial}{\partial t}\right) \\
P^{-1} \frac{\partial}{\partial t} & A^T
\end{bmatrix}
\begin{bmatrix}
V^n \\
I_L^n
\end{bmatrix}
=
\begin{bmatrix}
V_S \\
I_S
\end{bmatrix}$$

The PEEC method is particularly useful in modeling 3D interconnected thin-wire structures. In the past few years, this method has been applied for lightning analysis in buildings due to its high computational efficiency and excellent compatibility with nonlinear devices. In [19], lightning current and voltage in distribution circuits

within buildings were addressed. In these studies, the ground was assumed to be perfectly conductive. The residual current in a circuit was addressed as well during a direct lightning strike to a house.

### *2.1.2 The other numerical methods*

Lightning transients in a line structure can be evaluated using other numerical methods, such as Finite-difference-time-domain (FDTD) [20-21] Finite element method (FEM) [22], Method of moments (MoM) [23], Partial-element-equivalent-circuit (PEEC) [11-14] method and transmission line (TL) [24-25] method. These numerical methods have been successfully applied to analyze electromagnetic phenomena associated with bio-electromagnetic models, waveguide models, and printed circuit boards with lumped electric elements.

MoM [23] is based on the integral formulation of Maxwell's equations. This basic feature makes it possible to exclude the air around the objects in the discretization. The MoM is a full-wave numerical technique for solving open boundary electromagnetic problems. This technique is widely used to solve electromagnetic radiation, scattering problems. However, the voltage is not directly obtained in this technique and needs post-processing.

The FDTD method is an intuitive and powerful analysis technique to solve electromagnetic problems in the time domain. The FDTD method delivers the result in field variables, E and H, at all locations in the discretized domain and at every time point. To obtain structure currents and voltages post-processing is needed for the conversion. However, the issue of charge variation during the lightning process is not well-addressed in FDTD.

The finite element method (FEM) is suitable for narrow-band frequency investigation. These methods can deal with complex geometry and material characteristics of conductive bodies. Note that they both need to discretize the whole problem domain into a large number of small cells. For the delicate wire system, the length and volume of the cells need to be small enough to ensure a reasonable result. As a result, both memory space and computation time increase significantly, compared with the PEEC and TML methods which need to build the model for conductors only.

Recently, in [18] the low-frequency model of lossy ground and the vector fitting technique were proposed to model frequency-dependent components. The time-domain simulation would be made very efficient even in a model with frequency-dependent parameters. For practical engineering applications, the partial element equivalent circuit (PEEC) method has advantages in modeling complicated wire structure and is widely used in electromagnetic transient simulation in-ground structures [10]. Using this PEEC model it is possible to consider more complex and practical EMC problems.

## **2.2 Physical Mechanism of Lightning Strikes on Ground Structure**

A typical cloud-to-ground lightning flash generally starts with a downward leader process. In this process, a negatively-charged leader channel is generated together with the positive charge situated on the ground in its vicinity. This process is followed by a return stroke propagating upward which creates a substantial lightning current in the channel and radiates impulse electromagnetic fields outwards. Such electromagnetic fields induce transient voltages and currents on overhead lines, underground lines, and wiring systems in buildings, and may cause damage or malfunction of electrical and electronic equipment connected.

The return stroke is the most important element of a lightning flash in the evaluation of lightning transients. For lightning strikes on a ground structure, the return stroke current propagates both upward along the lightning channel and downward along the ground structures. The charge deposited along a channel by the upward propagating current will be neutralized with the initial charge surrounded the channel core. This will make the channel behavior to be both non-uniform and non-linear. The downward propagating current is of major concern in engineering applications. When this part of the current is reflected from the ground and propagates into the channel again, the channel behavior is different because of the previous neutralization by the upward propagating current. This situation is much complicated if both downward leader and upward leader with opposite initial charge are taken into consideration. The complicated ground structure is also another concern in lightning modeling. Thus, an integrated model is necessary for both lightning mechanism study and lightning protection engineering.

The physical mechanism of the corona sheath has been studied increasingly [26]. A simplified corona sheath model has been proposed in [27]. It is represented as a given lumped current source in either the engineering model [28], distributed circuit model [29], or the electromagnetic model [30]. In this model, the distributed charge inside the corona sheath, which plays a key role in the radial expansion of the corona sheath, is downplayed. Note that the charge characteristics of corona discharges in a coaxial geometry are well studied in [31]. However, when applied to the distributed circuit model of a lightning channel, the situation is simplified, again, into a lumped pre-given constant current source, called corona current [32]. It is more reasonable to consider the time-varying corona current in the model.

## **2.3 Modeling of Lightning Strikes on Ground Structures**

The modeling of lightning strikes on a ground structure has drawn a lot of attention in recent years. Several models have been proposed based on the existing electromagnetic numerical methods as mentioned in Section 2.2, including the engineering model [28], the antenna theory (AT) model [30], the macroscopic physical model [33], the distributed circuit model [29] and the hybrid electromagnetic model [34].

The engineering model has been widely used in various lightning electromagnetic pulse (LEMP) calculations [28]. This model assumes that a current wave, injected at the lightning channel base, propagates upward along the channel with specific velocity and attenuation. The reflection coefficients at the ground and the structure tip are given as constant. Thus, the spatial and temporal distribution of the current along the channel and the striking object can be calculated directly. The channel-base current is introduced in the engineering model as the source term, which is assumed as an input parameter of the model known from measurement observation results.

In the AT model, the lightning channel is modeled as a lossy vertical antenna attached to the tower top. The lossy antenna and the wire structure representing the tower are assumed to be fed at their junction point by a voltage source. The voltage waveform of this source is selected so that the source current resembles a typical lightning current waveform not influenced by the presence of the tall strike object.

For the macroscopic physical model considering both the lightning channel and tall objects based on the EFIE technique. The lump voltage source is added as an input source term and obtained by an undisturbed current source and input impedance [43], the correct boundary conditions between the building and the lightning channel are well performed. However, the solution may be very time consuming

The distributed circuit (DC) model, also called the transmission line model, uses a transmission line with per-unit-length inductance, capacitance, resistance, and conductance to represent a lightning channel [35]. Currents and voltages along the lightning channel are obtained from the solution of the well-known telegrapher's equations. In the original DC model [36], the constant distributed resistance and inductance are adopted. Later in [37], the model revised with the nonlinear time-varying resistance is introduced to mimic the radially expanding core radius. Furthermore, the non-uniform transmission line model is proposed in [38] to reproduce the current pulse attenuation and distortion. In this model, the characteristic impedance of a transmission line varies with height. The corona effect around the core can be modeled by either adding a non-linear dynamic capacitance or a corona current source [32]. It is found that the distributed circuit model with the presence of corona is capable of reproducing the most important characteristics of subsequent return strokes in a negative lightning flash, including the realistic return stroke speeds and the signatures typically observed in measured electromagnetic fields [29].

## **2.4 The Traditional Traveling Wave Theory**

The transmission line model is widely used in power systems, electronic systems, and communication systems. Unlike the lumped circuit element, when the wavelength of the transmitted electromagnetic wave and the object circuit size is comparable, the circuit has to be changed from a lumped parameter circuit to a distributed parameter circuit. The inductance, capacitance, resistance, conductance are distributed along the line. A typical segment of the transmission line model is shown below:

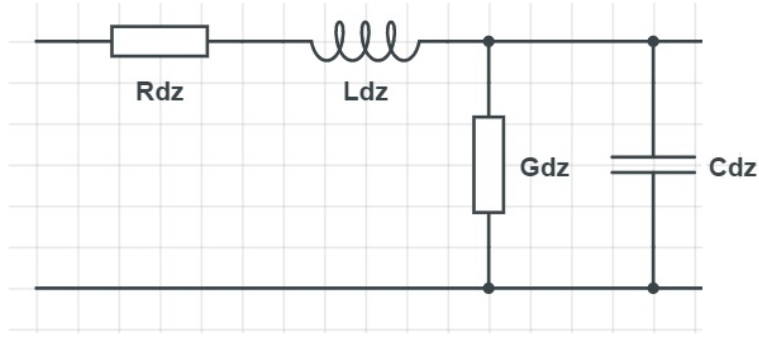


Fig. 2.3 The distributed circuit element of the transmission line model

The well-known telegrapher's equations are used in the transmission line model to describe the voltage  $V(z, t)$  and current  $I(z, t)$  with distance and time.

$$\begin{aligned} \frac{\partial}{\partial z} V(z, t) &= -L \frac{\partial}{\partial t} I(z, t) - RI(z, t) \\ \frac{\partial}{\partial z} I(z, t) &= -C \frac{\partial}{\partial t} V(z, t) - GI(z, t) \end{aligned} \quad (2.1)$$

Typically, if the transmission line is lossless, resistance and conductance can be removed:

$$\begin{aligned} \frac{\partial}{\partial z} V(z, t) &= -L \frac{\partial}{\partial t} I(z, t) \\ \frac{\partial}{\partial z} I(z, t) &= -C \frac{\partial}{\partial t} V(z, t) \end{aligned} \quad (2.2)$$

The lossless telegrapher's equations can be combined to get two wave equations, each with only one dependent variable, as follows:

$$\begin{aligned} \frac{\partial^2}{\partial z^2} V(z, t) &= LC \frac{\partial^2}{\partial t^2} I(z, t) \\ \frac{\partial^2}{\partial z^2} I(z, t) &= LC \frac{\partial^2}{\partial t^2} V(z, t) \end{aligned} \quad (2.3)$$

In the frequency domain, the solution of the wave equations is

$$\begin{aligned} V &= A_1 e^{-j\beta z} + A_2 e^{j\beta z} \\ I &= \frac{A_1}{Z_0} e^{-j\beta z} - \frac{A_2}{Z_0} e^{j\beta z} \end{aligned} \quad (2.4)$$

where  $\beta = \sqrt{LC}$  is the propagation constant and  $Z_0 = \sqrt{L/C}$  is the characteristic impedance. Both the voltage and current can be viewed as the superposition of incident waves  $U^i(z)e, I^i(z)$  and reflection waves  $U^r, I^r$ .

When considering the boundary condition such as the connected load  $Z_L$ , the reflection coefficient is introduced to express the ratio of the incident wave and the reflection wave that

$$\gamma(z) = \frac{U^-(z)}{U^+(z)} = \frac{Z_L - Z_0}{Z_L + Z_0} e^{-j2\beta z} \quad (2.5)$$

In the time domain, the solution of the wave equations (2.3) is the sum of a forward traveling wave and a backward traveling wave

$$V(z,t) = f_1(z - vt) + f_2(z + vt) \quad (2.6)$$

where,  $f_1$  and  $f_2$  can be arbitrary functions.  $f_1$  represents the wave traveling along positive z-direction and  $f_2$  represents the wave traveling along the negative z-direction.  $v = \sqrt{LC}$  is the propagation speed.

Similar to (2.5), with the characteristic impedance  $Z_0$  and the end load  $Z_L$ , the current and reflection coefficient is written as

$$I(z,t) = f_1(z - vt)/Z_0 + f_2(z + vt)/Z_0 \quad (2.7)$$

and

$$\gamma = \frac{Z_L - Z_0}{Z_L + Z_0} \quad (2.8)$$

To obtain the time domain traveling wave solution, there are three key constant parameters, characteristic impedance  $Z_0$ , propagation speed  $v$ , and reflection coefficient  $\gamma$ . The lattice diagram is a convenient and useful technique to express the general traveling wave solution with the three constant parameters mentioned before.

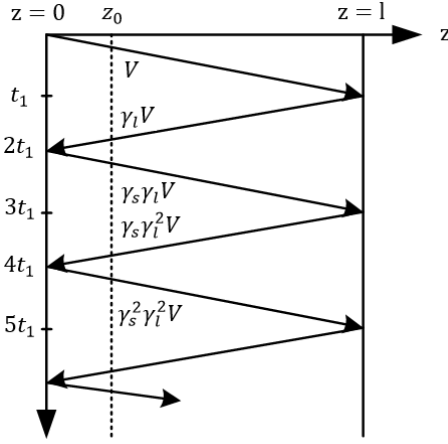


Fig. 2.4 Traveling wave and lattice diagram

The voltage  $V(z_0)$  at the observation point  $z_0$  can be obtained by the summation of each traveling wave component as shown in Fig. 2.4.  $\gamma_s$  and  $\gamma_l$  are the reflection coefficient respectively at the start and endpoint of the transmission line. The mathematical expression for  $V(z_0)$  is shown below.

$$\begin{aligned}
 V(z_0) &= V\left(t - \frac{z_0}{c}\right) + \sum_{n=1,2,\dots} \gamma_s^{n-1} \gamma_l^n V\left(t - \frac{z_0}{c} - \frac{2nl}{c}\right) + \sum_{n=1,2,\dots} \gamma_s^n \gamma_l^{n+1} V\left(t + \frac{z_0}{c} - \frac{2nl}{c}\right) \\
 I(z_0) &= \frac{V}{Z_0} \left(t - \frac{z_0}{c}\right) + \sum_{n=1,2,\dots} \gamma_s^{n-1} \gamma_l^n \frac{V}{Z_0} \left(t - \frac{z_0}{c} - \frac{2nl}{c}\right) + \sum_{n=1,2,\dots} \gamma_s^n \gamma_l^{n+1} \frac{V}{Z_0} \left(t + \frac{z_0}{c} - \frac{2nl}{c}\right) \quad (2.9)
 \end{aligned}$$

The traveling wave theory has been applied to analyze lightning transients in power lines, towers, and other structures. Recently the engineering model, which is based on the traveling wave solution of the transmission line model, has been widely used in the studies on the lightning strikes to tall structures. The propagation of current is assumed to be transverse electromagnetic (TEM) mode and the reflection coefficient at a discontinuity is normally given as a constant [39-40]. It is found in [41] that the ground reflection coefficient is dependent on the waveform and not influenced by the top of the struck object. In [42] the phenomenon of non-TEM wave propagation in a vertical conductor has been reported. The wave can be described using the electric scalar potential and current in the vertical structure. Note that the definition of quasi-static transverse voltage does not guarantee a unique value of the voltage on the tower [43]. It also is found that both the surge impedance [44] and the corresponding current attenuation [45-46] are time/position-variant. These studies, however, could not fully explain and formulate the varying surge impedance [43-

44]. The closed-form expression of the reflection coefficient and the dynamic behavior of a non-TEM wave in the tower with a discontinuity remain unknown.

# 3 The Extended Time Domain Traveling Wave Theory

In this chapter, to describe lightning surge propagation along vertical lines, the time-domain-traveling-wave (TDTW) theory is introduced. The wave equations for vector potential and scalar potential are used. Then the specially defined impedance is introduced under a ramp source waveform and then is extended to an arbitrary current/voltage source waveform. With the potential and impedance relationship, the TDTW theory for the grounded structure, discontinuities, and multi-conductor structure is proposed. Two typical applications using the TDTW theory are then presented.

## 3.1 The General Time-Domain-Traveling-Wave (TDTW) Theory

Surge propagation on vertical structures above the ground is a long-standing issue in lightning surge analysis. This is particularly important in predicting lightning overvoltage on electrical power systems as well as providing reference information for surge protection design. In the past decades, many experimental and theoretical studies have been carried out to investigate surge impedance [47-61] and the corresponding current attenuation phenomenon [62-65]. These studies provided useful information for researchers and engineers in understanding surge propagation behaviors along vertical structures and designing effective lightning protection.

The investigations into surge impedance have been carried out for a long time. In 1934, Jordan in [47] proposed the first theoretical equation based on the Neumann inductance equation. After that, several surge impedance equations were proposed using the field theory [48-59]. These equations all assume that the vertical conductor is a cylinder or an equivalent cylinder, and the surge propagation speed is assumed to be the same as the velocity of light. In these studies, the current attenuation in surge propagation was not taken into account. The author in [52] analyzed surge current in a dipole antenna fed with a unit step voltage. This configuration is similar to those discussed in [51]. Again current attenuation on the line was not taken into account. Numerical methods are also available to study lightning surges on the

vertical structures. These includes Method of Moment [53-54], partial element equivalent circuit (PEEC) [55-57], finite-difference finite-time method [63]. Except for the PEEC method, other methods are generally applicable to the surge current analysis only. So far there is no generalized theory for discussing traveling wave propagation in such structures.

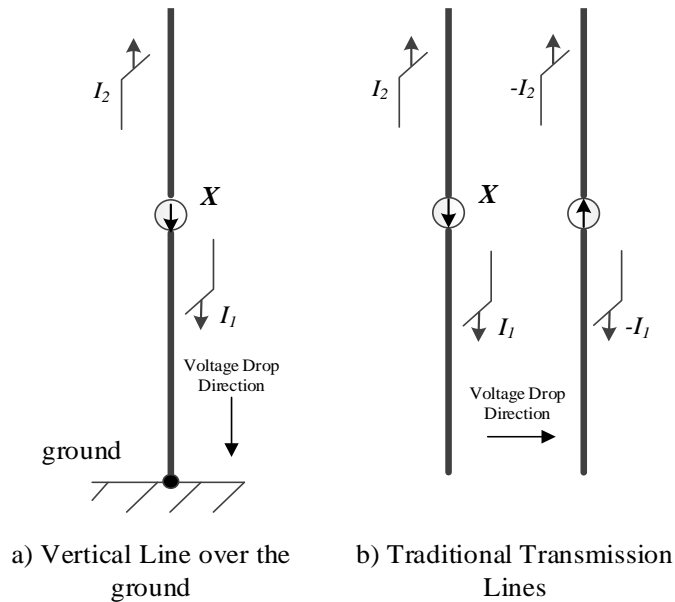


Fig.3.1 The comparison of vertical line structure and transmission lines

One critical issue in the discussion of traveling wave theory is the definition of voltage. Shown in Fig.3.1 is the comparison of the propagating current and voltage along vertical line structure and traditional transmission lines. In Fig.3.1 (b), the traditional transmission line theory is widely used for horizontal overhead wires or a pair of wires. The currents on the line are of opposite polarity, the voltage drop is approximated perpendicular to the line under TEM assumption. This voltage drop can be easily obtained with the integral of the electric field. The relationship between current and voltage can be written as  $V/I = Z_0$  with constant characteristic impedance  $Z_0 = \sqrt{L/C}$ .

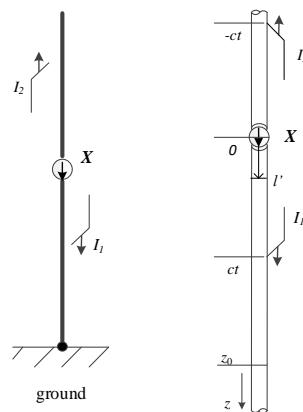
In Fig.3.1 (a), the propagating lightning current surge is without any return path. This results in a voltage drop mainly in the vertical direction. Note that the definition of quasi-static transverse voltage does not guarantee a unique value of voltage in this situation [65]. It is mentioned in many works of literature that [47-49] the voltage in this situation can be defined differently, such as:

- The line integral of the electric field from the ground to the top of a conductor.
- The potential difference between the top and bottom of a conductor.
- Measured value from the top of a conductor to a point far enough on the ground surface.

In this chapter, unlike the traditional transmission line theory, the surge potential instead of the surge voltage is discussed firstly to describe the non-TEM propagating surge. In the following sections 3.1.1-3.1.3, the characteristics of surges on a single conductor are described respectively upon the potential  $\phi$ , current I, and impedance Z.

### 3.1.1 Electric scalar potential $\phi$

In the discussion, the surge current source is placed in series between two conductor segments, as shown in Fig. 3.1(a). Fig. 3.1(a) shows a simplified configuration for surge propagation on a vertical line above the ground. Surges will be generated and propagate upwards and downwards. These surges have the same current values at Point X due to the current continuity. This configuration is similar to that of a vertical grounded structure struck by lightning. The return stroke can be viewed as a lumped current source placed between the grounded conductor and the lead wire when the current and potential on the ground object area of concern. The return stroke current propagates upwards along the lead wire and the discharge current propagates downwards to the ground.



a) Vertical conductor over the ground      b) Single conductor in free space

Fig.3.2 Configuration of a vertical line over the ground

Note that the ground does not affect the surge propagation if the reflected surge from the ground has not arrived. Without loss of generality, a single conductor with neither the ground nor a returning current path is then analyzed through this thesis. As shown in Fig. 3.2(b) this conductor is separated into two segments at Point X: upper and lower segments carrying surges propagating in opposite directions.

Surge propagation on a free-space single conductor excited by a ramp current source is then investigated numerically with the PEEC method. The cylindrical conductor has a radius of 5mm, and a length of 150m in both upper and lower segments, as shown in Fig. 3.2(b). It is connected to the perfect ground at the lower end and to a ramp current source of  $Kt$  ( $K = 5kA/\mu s$ ) at Point X on the conductor. In the PEEC method, wires are divided into short elements which are represented by coupled lumped-parameter circuit components. In this model, the conductor is equally divided into 2500 elements. Surge potential and current in the coupled network are analyzed using a circuit approach. Both surge current and potential are calculated in the frequency domain. The time-domain solution is obtained using an inverse Fourier Transform technique (*ifft*).

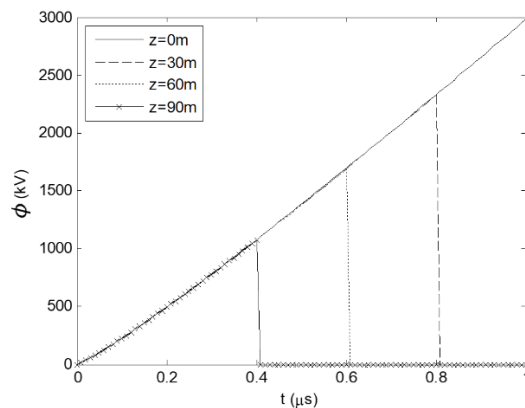


Fig. 3.3 Potential curves on the lower segment with time delay being removed.

Fig. 3.3 shows the curves of the surge potential at different positions along the conductor. The time delay of individual potential curves is removed again, and each curve is padded with zero when a reflected surge comes back from the ground. It is found that the potential curves at different positions on the conductor match very well. This indicates that there is no potential attenuation during its propagation. This phenomenon can be explained theoretically

According to Maxwell equations, electric scalar potential  $\phi$  at point  $z$  on a conductor (Fig. 3.2(b)) can be expressed by the magnetic vector potential  $A_z$  and electric field  $E_z$  in the  $z$ -direction, as follows;

$$\begin{aligned}\frac{\partial\phi(z,t)}{\partial z} &= -E_z(z,t) - \frac{\partial A_z(z,t)}{\partial t} \\ A_z(z,t) &= \int \frac{\mu_0 I(l', t - R/c)}{4\pi R} dl'\end{aligned}\quad (3.1)$$

where  $I(l', t - R/c)$  is a retarded surge current on the conductor, and is equal to zero when  $t < R/c$ . Both  $c$  and  $R$  are respectively the velocities of an electromagnetic wave in free space and the distance between the source-current point and observation point. On a perfect conductor electric field  $E_z$  in (3.1) is identically zero. As the resistance on a lossy conductor can be added into the surge impedance as a separate item [55], the lossy wire is not discussed in this thesis.

Throughout this thesis, potential  $\phi(z, t)$  given in [59] is selected to be the potential for addressing surge propagation on the conductor. This potential is determined by conductor geometry, observation position, and time, and is not affected by the path selected for the evaluation.

The exact expression of potential  $\phi(z, t)$  at position  $z$  and time  $t$  on a conductor of radius  $r$  is given by combining equations in (3.1) that

$$\phi(z,t) = \frac{\mu_0}{4\pi} \cdot \int_z^{ct} \frac{\partial}{\partial t} \int_{\frac{l-ct}{2}}^{\frac{l+ct}{2}} \frac{I(l', t - \frac{|l-l'|}{c})}{\sqrt{(l-l')^2 + r^2}} dl' dl \quad (3.2)$$

where  $I(0, t)$  is the source current at Point X. The derivation of (3.2) is given in Appendix A.

Note that (3.2) is a complicated expression and inefficiency in computation. Here we introduce the wave equations of scalar potential  $\phi$  and vector potential  $A$  as used in [60] that

$$\begin{aligned}\frac{\partial^2 \phi(z,t)}{\partial z^2} &= \frac{1}{c^2} \frac{\partial^2 \phi(z,t)}{\partial t^2} \\ \frac{\partial^2 A(z,t)}{\partial z^2} &= \frac{1}{c^2} \frac{\partial^2 A(z,t)}{\partial t^2}\end{aligned}\quad (3.3)$$

Note that a solution of (3.3) for the downward surge is given by

$$\begin{aligned} A(z, t) &= F(z - ct) \\ \phi(z, t) &= G(z - ct) \end{aligned}$$

where  $F(\cdot)$  and  $G(\cdot)$  are wave functions for the vector potential and scalar potential, respectively.

Thus, for a lossless conductor, the one-directional scalar potential and vector potential are both lossless during propagation. A further relationship between scalar potential  $\phi$  and vector potential  $A$  for a single traveling wave is derived in Appendix B, that is,  $\phi(z, t) = cA(z, t)$ . Thus, the potential  $\phi(z, t)$  in (3.2) can also be evaluated as

$$\phi(z, t) = \frac{\mu_0 c}{4\pi} A(z, t) = \frac{\mu_0 c}{4\pi} \cdot \int_{\frac{z-ct}{2}}^{\frac{z+ct}{2}} \frac{I(l', t - \frac{|z-l'|}{c})}{\sqrt{(z-l')^2 + r^2}} dl' \quad (3.4)$$

This is the general evaluation of potential  $\phi(z, t)$  with given current distribution  $I(z, t)$  in the TDTW theory for a one-directional single traveling wave

It is noted that the current distribution is unknown because, unlike the traditional transmission line theory based on the TEM assumption, this current distribution would suffer both attenuation and distortion during its propagation [57]. In the next section, this characteristic of current attenuation will be discussed.

### 3.1.2 The distorted and attenuated current $I$

Fig. 3.4 shows the time-domain curves of the surge current at different positions along the conductor. In the figure, the time delay of individual current curves is removed. As the reflected surge is not an issue of concern in this section, all the curves are padded with zero when a reflected surge from the ground or a discontinuity arrives. This is for easy identification of curves at different locations. It is found in the figure that the surge current attenuates or the slope of its waveform decreases with increasing distance to the observation point. The change, however, becomes less at a farther position.

This phenomenon was observed in the experimental results of the surge propagation on perfect vertical conductors, especially near the source region [64]. A

“scatter theory” was proposed by authors in [63] to explain the current attenuation. The surge associated with an electromagnetic wave in a non-zero thickness vertical conductor does not transmit in TEM mode. The attenuation can be attributed to the “reflected surge” generated during propagation.

The attenuation coefficient of surge current  $p(z, t)$  is introduced in this thesis for surge evaluation. It is defined by a ratio of the current  $I$  with propagation attenuation to the current  $I'$  without propagation attenuation, as follows:

$$\begin{aligned} p(z, t) &= \frac{I(z, t)}{I'(z, t)} \\ &= \frac{I(z, t)}{I_0(t - z/c)} \end{aligned} \quad (3.5)$$

for  $t \geq z/c$ . The attenuation coefficient of the surge current is affected by the conductor radius as well. Fig. 3.5 shows time-domain curves of attenuation coefficient at different positions for two-conductor radii. The time delay of each curve is removed. It is found that current attenuation is significant in the early time, and becomes small when time goes on. The current attenuation is significant as well as near the source point. It is also found that the attenuation coefficient approaches one when the radius becomes small.

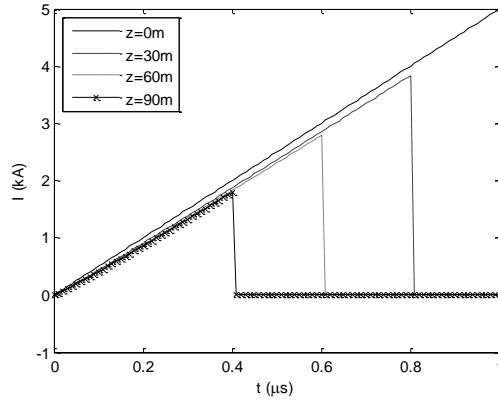


Fig. 3.4 Current curves on the lower segment with time delay being removed

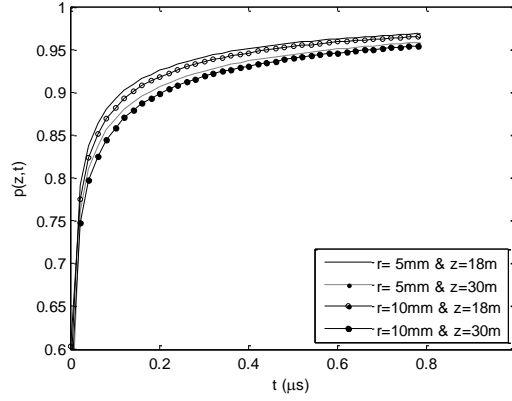


Fig. 3.5 Attenuation coefficient  $p(z, t)$  of surge current at  $z=18\text{m}$  and  $30\text{m}$  with conductor radius  $r=5\text{mm}$  and  $10\text{mm}$

### 3.1.3 The time-and-space-varied impedance $Z$

Characteristic impedance is a key parameter to describe wave propagation over a line and is generally expressed by the ratio of voltage to current. Though it is known that further analysis of surge behavior on vertical conductors needs time-variant surge impedance expressions [56-58], the question of “how to define surge impedance” obstructs the understanding of this problem. Authors in [57-58] quoted some definitions of surge impedance in the time domain as below;

- Transient surge impedance defined by voltage  $v(t)$  and current  $i(t)$  at the top of a conductor:

$$z(t) = \frac{v(t)}{i(t)} \quad (3.6)$$

- Surge impedance defined by voltage  $v(t)$  and current of a single value:

$$z(t) = \frac{v(t)}{\max[i(t)]} \quad (3.7)$$

where the current is of either a step wave or a ramp wave.

In this chapter, the definition of surge impedance given in (3.6) is adopted and extended. As mentioned before, the scalar potential instead of voltage is used. To consider both the distortion and attenuation of surge current along the conductor, we introduce a time-and-space-varied impedance  $Z(z, t)$  that is,

$$Z(z,t) = \frac{\phi(z,t)}{I(z,t)} \quad (3.8)$$

The evaluation of  $Z(z,t)$  is settled in this chapter under the ramp current waveform. Both analytical and numerical methods for obtaining  $Z(z,t)$  are derived respectively in section 3.2.1 and section 3.2.2.

Fig. 3.6 shows time-domain curves of surge impedance at different positions on a conductor with a radius of 5mm. For comparison, the time delay of each curve in the figure is removed. It is noted that that surge impedance increases with time, but the changing rate becomes small as time goes on. The surge impedance increases as well when the distance to the source point is increased. However, the change of surge impedance will be small if the observation point is away from the source.

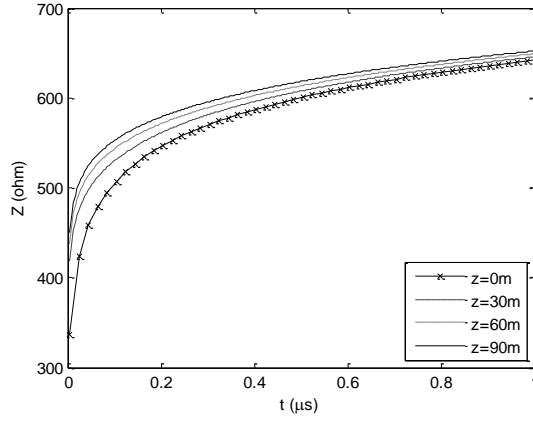


Fig.3.6 Surge impedance on a single conductor with the radius of 5mm

## 3.2 The Solutions of the Non-TEM Propagating Wave

### 3.2.1 Analytical solution for $Z$ , $\phi$ , and $I$ .

By using the definition of transient surge impedance given in (3.8) with the potential given in (3.4), surge impedance at point  $z$  is obtained according to (C4) in appendix C

$$Z(z,t) = \frac{\mu_0 c}{2\pi} \left( \frac{z}{ct-z} \ln \frac{ct+z}{\sqrt{z^2+r^2}+z} + \ln \frac{\sqrt{c^2 t^2 - z^2}}{r} - 1 \right) \quad (3.9)$$

for  $t \geq z/c$ . At Point X ( $z = 0$ ), surge impedance of the vertical conductor reduces to

$$Z(0,t) = 60 \left( \ln \frac{ct}{r} - 1 \right) \quad (3.10)$$

Then, according to Appendix B that the lossless propagation of the potential wave, the following equation is then written:

$$\phi(z,t) = I(z,t)Z(z,t) = I(t-z/c)Z(0,t-z/c) \quad (3.11)$$

Then, by substituting (3.11) into (3.3), the attenuation coefficient can also be written as:

$$\begin{aligned} p(z,t) &= \frac{I(z,t)}{I_s(t-z/c)} \\ &= \frac{Z(0,t-z/c)}{Z(z,t)} \end{aligned} \quad (3.12)$$

This means that once the source current  $I_s(z,t)$  and impedance  $Z(z,t)$  is known, the current distribution as well as the potential can be obtained through (3.11-3.12).

Some analytic formulas of surge impedance have been derived in the literature by using different approaches. These formulas are normally used to estimate the surge at the top of a grounded conductor just before a reflected surge from the ground reaches the top of the conductor. Table 3.1 shows some of the surge impedance formulas together with the proposed formula of (6). It is noted that these expressions are very similar. Only the coefficients or the constants of the formulas are different. The difference might be caused by; (a) the upward lead wire is not taken into account, or (b) a step function is adopted for the current source. Note that the revised Jordan's expression [62] is the same as the proposed formula when  $t = 2H/c$ . However, the revised Jordan's expression was derived with the following assumptions:

- The constant current along the conductor is assumed;
- The effect of the conductor image is considered;
- The effect of an upward lead wire is not considered.

Table 3.1 Analytic formulas of surge impedance for a vertical conductor with height  $H$  and radius  $r$  above the ground

Revised Jordan formula [60]	$Z = 60 \ln(4H/r) - 60$
Wagner formula [47]	$Z = 60 \ln(2\sqrt{2}H/r)$
Sargent formula [50]	$Z = 60 \ln(\sqrt{2}H/r) - 60$
CIGRE formula [67]	$Z = 60 \ln [\cos[0.5 \tan^{-1}(H/r)]]$
Proposed formula (3.9)	$Z = 60 \ln(2H/r) - 60$

### 3.2.2 Numerical Solution for $Z$ , $\phi$ , and $I$ .

An iterative method is presented in this section for the evaluation of surge propagation on a free-space single conductor. This procedure does not request a detailed knowledge of circuit modeling. With the information of conductor geometry and current source, surge current, potential, and impedance can be obtained directly.

Assume source current  $I_0(t)$  at Point X is already given, and the attenuation coefficient  $p(z, t)$  is known. Let discrete values  $z_i = i\Delta z$ , and  $t_j = j\Delta t$  (position index  $i$  and time index  $j = 0, \dots, N$ ) and  $\Delta z = c\Delta t$ . With the results in Appendix A, discrete potential  $A_{i,j} = A_z(z_i, t_j)$  is expressed by

$$A_{i,j} = \frac{\mu_0}{4\pi} \int_{\frac{z_i - ct_j}{2}}^{\frac{z_i + ct_j}{2}} \frac{I(l', t - |z_i - l'|/c)}{\sqrt{(z_i - l')^2 + r_1^2}} dl' \quad (3.13)$$

where  $ct_j > z_i$ .  $r_1$  is the radius of the conductor. To evaluate (3.13), the interval of  $l'$  is divided into three sub-segments, that is,  $[0.5(z_i - ct_j), 0]$ ,  $[0, z_i]$  and  $[z_i, 0.5(z_i + ct_j)]$ . By replacing  $dl' = -dl'$  in the first interval of  $[0.5(z_i - ct_j), 0]$ , vector potential  $A_{i,j}$  turns to

$$\begin{aligned}
A_{i,j} = \frac{\mu_0}{4\pi} & \left[ \int_0^{\frac{ct_j - z_i}{2}} \frac{I(l', t - (z_i + l')/c)}{\sqrt{(z_i + l')^2 + r_1^2}} dl' + \right. \\
& \int_0^{z_i} \frac{I(l', t - (z_i - l')/c)}{\sqrt{(z_i - l')^2 + r_1^2}} dl' + \\
& \left. \int_{z_i}^{\frac{z_i + ct_j}{2}} \frac{I(l', t - (l' - z_i)/c)}{\sqrt{(z_i - l')^2 + r_1^2}} dl' \right] \tag{3.14}
\end{aligned}$$

It is noted from (3.3) that  $I(l', t)$  can be expressed with source current  $I_0$  and attenuation coefficient  $p(l', t)$ . Three surge currents in (3.14) are then expressed by

$$\begin{aligned}
I(l', t_j - \frac{z_i + l'}{c}) &= I_0(t_j - \frac{z_i - 2l'}{c}) \times p(l', t_j - \frac{z_i + l'}{c}) \\
&\approx \sum_{k=0}^{(j-i)/2} I_{0,j-i+2k} \times p_{k,j-i-k} \times U_k(l') \\
I(l', t_j - \frac{z_i - l'}{c}) &= I_0(t_j - \frac{z_i}{c}) \times p(l', t_j - \frac{z_i - l'}{c}) \\
&\approx \sum_{k=0}^i I_{0,j-i} \times p_{k,j-i+k} \times U_k(l') \\
I(l', t_j - \frac{l' - z_i}{c}) &= I_0(t_j - \frac{2l' - z_i}{c}) \times p(l', t_j - \frac{l' - z_i}{c}) \\
&\approx \sum_{k=0}^{(j+i)/2} I_{0,j+i-2k} \times p_{k,j+i-k} \times U_k(l') \tag{3.15}
\end{aligned}$$

where  $I_{0,j}$  is the discrete source current at  $t = t_j$ , and  $p_{i,j}$  is the discrete attenuation coefficient at  $z = z_i$  and  $t = t_j$ . In (3.15) pulse function  $U_k(l')$  is defined by

$$U_k(l') = \begin{cases} 1 & k\Delta z \leq l' < (k+1)\Delta z \\ 0 & \text{otherwise} \end{cases} \tag{3.16}$$

Substituting (3.15) in (3.14) yields

$$\begin{aligned}
A_{i,j} = \frac{\mu_0}{4\pi} & \left[ \sum_{k=0}^{(j-i)/2} I_{0,j-i+2k} \times p_{k,j-i-k} \times f_{1,i}(k) + \right. \\
& \sum_{k=0}^i I_{0,j-i} \times p_{k,j-i+k} \times f_{2,i}(k) + \\
& \left. \sum_{k=i}^{(j+i)/2} I_{0,j+i-2k} \times p_{k,j+i-k} \times f_{2,i}(k) \right] \tag{3.17}
\end{aligned}$$

where functions  $f_{1,i}(k)$  and  $f_{2,i}(k)$  are defined by

$$\begin{aligned}
f_{1,i}(k) &= \frac{\mu_0}{4\pi} \int_{k\Delta z}^{(k+1)\Delta z} \frac{dl'}{\sqrt{(i\Delta z + \Delta z/2 + l')^2 + r^2}} \\
&= \frac{\mu_0}{4\pi} \ln \frac{k+1.5+i+\sqrt{(k+1.5+i)^2 + (r/\Delta z)^2}}{k+0.5+i+\sqrt{(k+0.5+i)^2 + (r/\Delta z)^2}} \\
f_{2,i}(k) &= \frac{\mu_0}{4\pi} \int_{k\Delta z}^{(k+1)\Delta z} \frac{dl'}{\sqrt{(i\Delta z + \Delta z/2 - l')^2 + r^2}}
\end{aligned} \tag{3.18}$$

For  $k \neq i$

$$f_{2,i}(k) = \frac{\mu_0}{4\pi} \ln \frac{k+0.5-i+\sqrt{(k+0.5-i)^2 + (r/\Delta z)^2}}{k-0.5-i+\sqrt{(k-0.5-i)^2 + (r/\Delta z)^2}}$$

For  $k = i$

$$f_{2,i}(k) = \frac{\mu_0}{2\pi} \ln \frac{0.5+\sqrt{(0.5)^2 + (r/\Delta z)^2}}{r/\Delta z}$$

Note in Appendix B that vector potential propagates downwards without any attenuation, that is,  $A_{i,j} = A_{i-k,j-k}$  ( $k = 1, \dots$ ). If any difference of vector potential at different positions along the conductor is observed, the attenuation coefficient  $p_{i,j}$  will be adjusted. The vector potential will be updated again.

In the proposed algorithm, the following error of vector potential ( $ERR^{(m)}$ ) in the  $m$ -th iteration is checked

$$ERR^{(m)} = \sum_{i=0}^N \sum_{j=0}^N \frac{A_{i,j}^{(m)} - A_{i+1,j+1}^{(m)}}{A_{i,j}^{(m)}} \tag{3.19}$$

If  $ERR^{(m)}$  is greater than a pre-set value, the attenuation coefficient  $p_{i+1,j+1}^{(m+1)}$  will be updated with

$$p_{i+1,j+1}^{(m+1)} = \Delta p_{i,j}^{(m+1)} + p_{i,j}^{(m+1)} \tag{3.20}$$

In (3.20) difference of attenuation coefficient  $\Delta p_{i,j}^{(m+1)}$  is determined by

$$\Delta p_{i,j}^{(m+1)} = \Delta p_{i,j}^{(m)} \times e^{\beta \times \frac{A_{i,j}^{(m)} - A_{i+1,j+1}^{(m)}}{A_{i,j}^{(m)}}} \quad (3.21)$$

where  $\beta$  is a damping coefficient. A minimum value of the damping coefficient could be set for the fast convergence of the iterative method. Before the calculation with (3.17), a boundary condition has to be set, that is,  $p_{0,j}^{(m+1)} = 1$  for any  $j$ . This means that the current at Point X does not have any attenuation. After  $p_{i,j}^{(m+1)}$  is obtained, potential  $\phi_{i,j}^{(m+1)}$  can be calculated using (B6). The flow chart of this iterative procedure is given in Fig. 3.7.

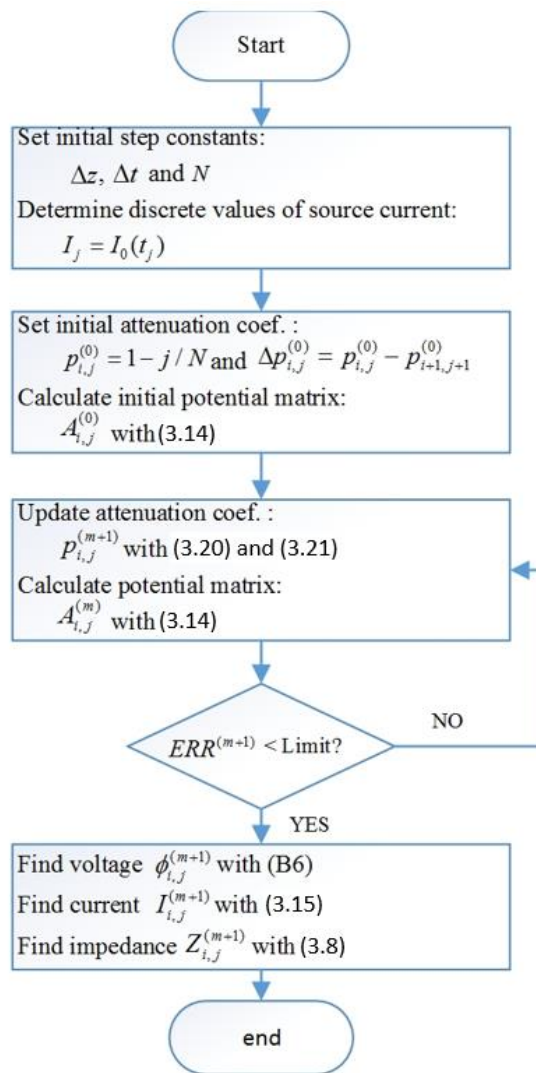


Fig. 3.7 Iterative method for surge evaluation

Propagation characteristics of a surge on a free-space single conductor can be analyzed by applying the proposed iterative method. This method has been coded on

the MATLAB platform. With the source current and conductor radius, this MATLAB program returns the attenuation coefficient of the surge current, as well as surge potential, current, and impedance at any time and any position along the conductor.

### 3.2.3 Comparison with PEEC results

Numerical comparison with the PEEC results has been made. The configuration of a conductor system for comparison is illustrated in Fig. 3.2(b). Both conductor and source parameters are given in Fig. 3.2(b) in Section 3.1.2, as well as PEEC simulation parameters. In the simulation with the proposed iterative method, both distance and time steps  $\Delta z$  and  $\Delta t$  were selected to 1.5m and 5ns, respectively. It is noted that simulation time in a PC with i7-4790 CPU at 3.6GHz and 16GB RAM is 27.5 sec. with the iterative method, and 3hr 15min. with the PEEC method.

Fig. 3.8 shows the surge current at  $z=30m$  on the conductor calculated with (1) the iterative method and (2) the PEEC method. It is noted that there is no difference between these two curves. The average error is less than 1%. The source current at Point X is also presented in the figure for reference. Fig. 3.9 shows surge impedance at  $z = 0m$  and  $z = 30m$  calculated with these two methods. When the current attenuation is taken into consideration, the calculated impedance matches the PEEC result. The average difference between the calculated surge impedance and the simulated one is 0.2% for the time greater than  $0.2\mu s$ .

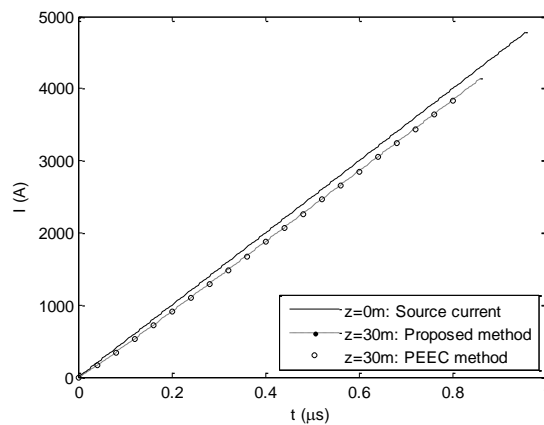


Fig. 3.8 Surge current on the vertical conductor under a ramp current source

A relatively large difference of these curves is observed in the early time in which the current is relatively small. This difference arises from using the frequency-

domain PEEC method. Because both *fft* and *ifft* techniques are used to obtain the time-domain result, a small non-zero current is observed in the PEEC result even before the surge arrives. This leads to a relatively large error.

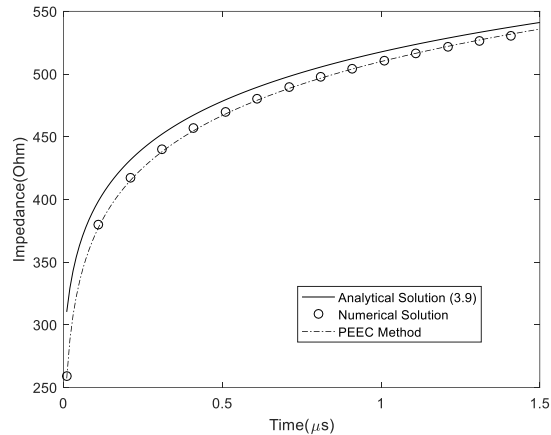


Fig. 3.9 Surge impedance on the vertical conductor under a ramp current source

For comparison, surge impedance calculated with the simplified formula (3.9) is presented in the figure as well. It is noted that there is a large difference between the results using the simplified formula and the iterative method. The surge impedance is generally overestimated if the theoretical formula is used, as the current attenuation is not taken into consideration.

### 3.3 The Time-and-space-varied Impedance for Arbitrary Current Waveform

It is noted in Section 3.2 that simplified surge impedance given in (3.8) is not affected by the slope of a ramp current source. It is then interesting to know whether the surge impedance is affected by the source current waveform when the current attenuation is taken into account. Simulation of surge impedance with different current waveforms has been carried out using the proposed iterative method. Three groups of representative waveforms were selected for evaluation, that is, (a) ramp waveform, (b) impulse waveform with a slow or fast-rising rate, and (c) impulse waveform with a fast or slow decaying rate.

As shown in fig. 3.2(b), all the waveforms used for a surge current injected at Point X. The front time of an impulse current is either  $0.06\mu\text{s}$  or  $0.12\mu\text{s}$ , and the time to half-peak is either  $0.95\mu\text{s}$  or  $100\mu\text{s}$  approximately. The impulse current has a fixed

magnitude of 10kA. The ramp current has a slope of either 10kA/ $\mu$ s or 20kA/ $\mu$ s. Fig. 3.10b shows the curves of surge impedance under five different current waveforms. It is noted that the slope of a ramp current does not affect the surge impedance. This is the same as that observed from the simplified formula of (3.9). The surge impedance under an impulse current source is, however, significantly different from that under a ramp waveform. The surge impedance generally varies with the front time and the time to half-peak. It increases quickly if the front time is short, and remains the same if there is no difference in the tail. Surge impedance generally continues to increase no matter what waveform the tail has. The surge impedance will increase quickly if the time to half-peak is short. Therefore, the surge impedance under a ramp current generally has a lower impedance than that under an impulse current.

Although surge impedance is not affected by the slope of a ramp function, it is indeed changed by the shape of the source current waveform, as seen in Fig. 3.10. This is because the surge impedance of a standalone line is time-variant.

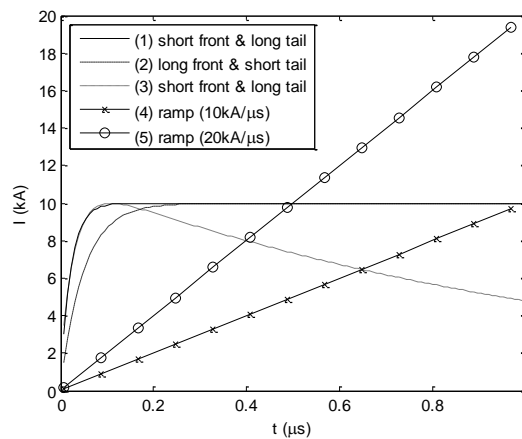


Fig. 3.10a Waveforms of a surge current propagating on the conductor

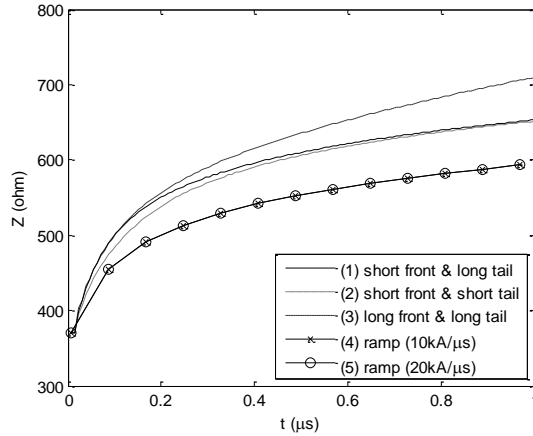


Fig. 3.10b Surge impedance with different waveforms of a surge current

The evaluation of the current and potential response under arbitrary current source waveform is derived in this section. As shown in Fig. 3.11, an arbitrary waveform can be expressed approximately by a series of ramp waveforms with different time delays, as follows,

$$I(t) = \sum_{j=0}^N k_j \cdot r(t - j\Delta t) \quad (3.22)$$

where  $r(t - j\Delta t)$  is a unit ramp function with the slope of one applied at  $t = j\Delta t$ .  $\Delta t$  is the time step used in the evaluation of surges. In particular, the slope  $k_j$  can be expressed as,

$$k_j = \begin{cases} \frac{I(\Delta t)}{\Delta t} & j = 0 \\ \frac{I[(j+1)\Delta t] - I[j\Delta t] + I[(j-1)\Delta t]}{\Delta t} & j \neq 0 \end{cases} \quad (3.23)$$

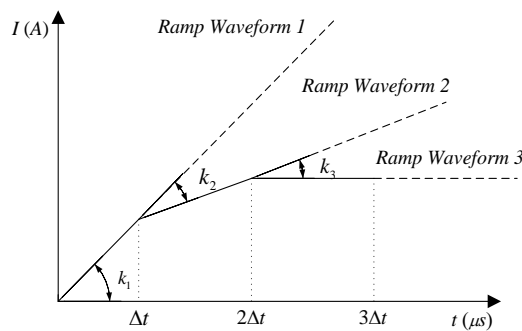


Fig. 3.11 Decomposition of an arbitrary waveform into ramp waveforms

The surge impedance and attenuation coefficient do not vary with the slope of a ramp source current [9]. Both surge current and electric potential on the line arising from a unit ramp current applied at  $j\Delta t$  can be directly obtained through (10) and (12). The surge current and electric potential under the arbitrary-waveform current source can be given by,

$$\begin{aligned} I_{arbi}(z, t) &= \sum_{j=1}^N k_j I(z, t - j\Delta t) \\ \phi_{arbi}(z, t) &= \sum_{j=1}^N k_j \phi(z, t - j\Delta t) \end{aligned} \quad (3.24)$$

This expression indicates that both potential and current excited by an arbitrary-waveform current source can be calculated with the surge responses of a ramp current source, or characteristic parameters  $p_a(z, t)$ , and  $Z_a(z, t)$  of a vertical line.

### 3.4 The Response Transfer under Arbitrary Source Voltage/Current Waveform

In section 3.2, the vertical line is fed by a current source with a ramp waveform. To find out the current and potential response under an arbitrary-waveform current, the technique in section 3.3 is adopted. This can be expressed with a more general technique, called the convolution technique, in this chapter. Assume that the current/voltage response under a ramp feed current is  $e_i(t)$ , which is obtained with the numerical/analytical solution in section 3.2. According to the convolution properties in a linear time-invariant system [69], the impulse response  $h_i(t)$  of the dipole is derived to be

$$h_i(t) = \frac{d^2 e_i(t)}{dt^2} \quad (3.25)$$

Then, response  $y(t)$  of the dipole under an arbitrary-waveform feed current  $I_s(t)$  is written as:

$$y(t) = I_s(t) * h_i(t) \quad (3.26)$$

Note that the step response of the current given by the delta-gap voltage is presented in [68]

$$I_{step}(z, t) = \frac{u(t - z/c)}{\sqrt{\mu_0/\epsilon_0}} \tan^{-1} \left( \frac{\pi}{2 \ln \sqrt{c^2 t^2 - z^2}/r} \right) \quad (3.27)$$

Then, the impulse response  $h_v(z, t)$  of feed-point current in the dipole excited by a voltage source can be expressed by the step response  $I_{step}(z, t)$  [69], as follows:

$$\begin{aligned} h_0(t) &= dI_{step}(0, t)/dt \\ &= \sqrt{\frac{\epsilon_0}{\mu_0}} \left[ \delta(t) \tan^{-1} \left( \frac{\pi/2}{\ln(ct/r)} \right) - \frac{u(t)}{\pi t \ln(ct/r) + 4} \right] \end{aligned} \quad (3.28)$$

The dipole response  $y(t)$  under the source voltage  $V_s(t)$  then is expressed by

$$y(t) = [V_s(t) * h_0(t)] * h_i(t) \quad (3.29)$$

The evaluation of the dipole response is illustrated in Fig. 3.12.

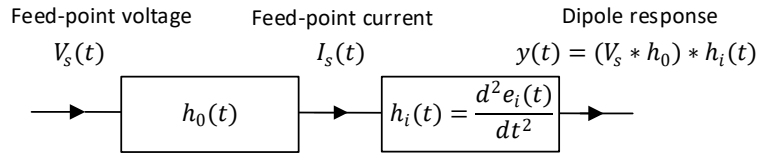


Fig. 3.12 Flowchart of dipole response evaluation given by the source voltage

### 3.5 The Extended TDTW Theory for a Grounded Vertical Structure

Vertical structures on the ground, such as towers and buildings, are subject to lightning strikes. Severe lightning electromagnetic environments may cause malfunction or even damage to vulnerable equipment in the vicinity. Therefore, it is of significant importance to evaluate lightning current and potential along vertical structures to protect the equipment on the towers or in the buildings.

This section presents an extended discussion on the surge propagation on a ground vertical conductor resulting from the ground reflection, with the characteristic parameters of a vertical line [70]. The conductor is connected to the earth via a grounding electrode and is subject to a lightning stroke at its top end. With the surge impedance and attenuation coefficient of current, the propagation mechanism on the grounded conductor can be revealed. More importantly, explicit expressions of

surges resulting from the ground reflection are derived under the source current with a ramp or an arbitrary waveform. Finally, numerical validation with both finite-difference and time-domain (FDTD) method [71] and the PEEC method [72] is presented.

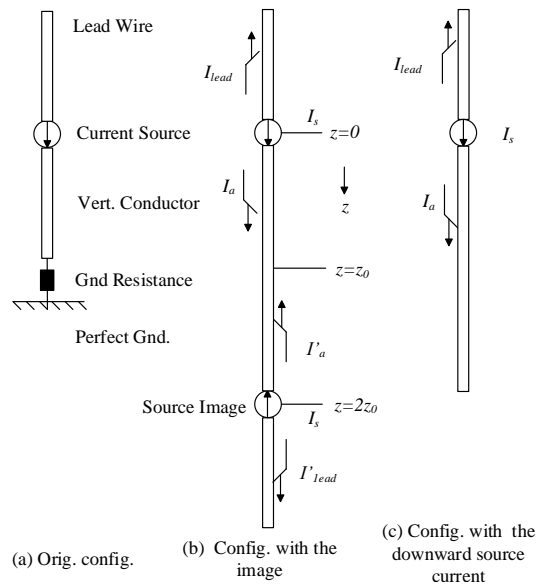


Fig. 3.13 Configurations of a vertical grounded conductor subject to lightning

### 3.5.1 Reflection under a Ramp-Waveform Current Source

Fig. 3.13(a) is a typical configuration of the grounded vertical conductor subject to a lightning stroke. The lightning stroke is represented with current source  $I_s$  connected on the top end of the conductor ( $z = 0$ ). The current source can generate the lightning return stroke current propagating upwards in the lightning channel and the lightning discharge current propagating downwards to the ground on the vertical conductor. Notably, the vertical conductor is connected to a grounding electrode, which is represented with ground resistance  $R$ . A reflected surge is generated when the downward lightning current reaches the ground surface ( $z = z_0$ ). It was reported in [72] that the material parameters of the soil, such as conductivity and permittivity have little influence on surge propagation on a vertical line. Therefore, the analysis is performed on the line connected to a perfect ground via grounding resistance  $R$ , as shown in Fig. 3.13(a).

### 3.5.2 Scenario I: ground resistance $R=0$

By using the image method, the perfect ground is substituted with the images placed under the ground surface. As seen in Fig. 3.13(b), the conductor is extended to the source image at  $z = 2z_0$ . The source image is connected to the lead wire image on the other end. Since this configuration is symmetrical to the ground surface, an upper part of the line configuration is selected for discussion, as shown in Fig. 3.13 (c). The surge propagation over such a line can be described with the theory of the vertical transmission line proposed in [70].

It is assumed that the conductor is perfectly conductive. Under a ramp current source  $I_s$  applied at  $z = 0$  and  $t = 0$ , surge current  $I_a(z, t)$  on the conductor with radius,  $r$  can be expressed with the attenuation coefficient  $p_a(z, t)$  [70], i.e.,

$$I_a(z, t) = I_a\left(0, t - \frac{z}{c}\right) \cdot p_a(z, t) \quad z \geq ct, \quad (3.30)$$

where  $I_a(0, t - z/c)$  is the retarded current without attenuation, and equal to  $I_s(t - z/c)$ .  $c$  is the speed of an electromagnetic field wave in free space. With surge impedance  $Z_a(z, t)$  [70], electric potential  $\phi_a(z, t)$  is given as,

$$\phi_a(z, t) = I_s\left(t - \frac{z}{c}\right) \cdot p_a(z, t) \cdot Z_a(z, t) \quad (3.31)$$

Both  $p_a(z, t)$  and  $Z_a(z, t)$  are the characteristic parameters of a vertical transmission line. They can be determined numerically using an efficient iterative procedure given in Section 3.2. These parameters vary with wire radius but are not affected by the slope of a ramp waveform.

It should be noted that the resultant surge on the conductor is the sum of surges  $I_a$  and  $I'_a$  which are symmetrical to the ground surface. These components have the same expressions, but arise from the current source at  $z = 0$  and its image at  $z = 2z_0$ , respectively. As a result, the total surge current above the ground ( $0 \leq z \leq z_0$ ) is expressed as

$$\begin{aligned} I(z, t) &= I_a(z, t) + I'_a(z, t) \\ &= I_s\left(t - \frac{z}{c}\right) p_a(z, t) + I_s\left(t - \frac{2z_0 - z}{c}\right) p_a(2z_0 - z, t) \end{aligned} \quad (3.32)$$

### 3.5.3 Scenario II: ground resistance $R \neq 0$

Fig. 13(a) shows the simplified configuration of a grounded conductor terminated with a ground resistance. Resistance  $R$  is inserted in series between the conductor and its image. In this scenario, additional surge current  $I_{\Delta}$  and its image  $I'_{\Delta}$  will be generated when a lightning current reaches the ground. The propagation starts from the ground surface in opposite directions. The total surge current in (3.32) is revised as

$$I(z, t) = I_a(z, t) + I_a(2z_0 - z, t) + I_{\Delta}(z, t) \quad (3.33)$$

As seen in Fig. 3.14(a), both  $I_{\Delta}$  and  $I'_{\Delta}$  are symmetrical to the ground surface. This is equivalent to the configuration where a virtual current source  $I_{\Delta}(z_0, t)$  is placed at  $z = z_0$ , as illustrated in Fig. 3.14(b). Based on the theory of the vertical transmission line [9], the upward surge current can be expressed as:

$$I_{\Delta}(z, t) = I_{\Delta}(z_0, t - \frac{z_0 - z}{c}) \cdot p_a(z_0 - z, t - \frac{z_0}{c}) \quad (3.34)$$

Attenuation coefficient in (3.34), resulting from the virtual source  $I_{\Delta}(z_0, t)$  applied at  $z = z_0$  and  $t = z_0/c$ , have the same expression as that used in (1). Similar to (2), the electric potential on the bottom end of the line is given as

$$\phi_{\Delta}(z_0, t) = -I_{\Delta}(z_0, t) \cdot Z_a(0, t - \frac{z_0}{c}) \quad (3.35)$$

In (3.35) the negative sign arises from the upward propagation of  $I_{\Delta}$ . Similarly, surge impedance in (3.35) yielding from the virtual source has the same expression of that in (3.31).

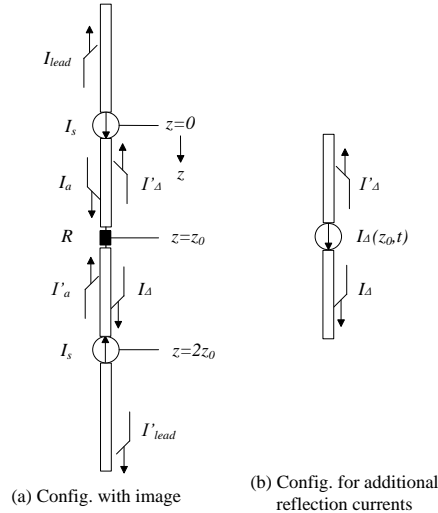


Fig. 3.14 Configuration of a vertical line with resistance subject to lightning

The current in (3.33) yields a resistive voltage on the ground resistance as well,

$$V_R = (I_a(z_0, t) + I'_a(z_0, t) + I_\Delta(z_0, t)) \times R \quad (3.36)$$

The symmetric property leads to the fact that  $I_a(z_0, t) = I'_a(z_0, t)$ . As the electric potential of the earth is equal to zero, i.e.,  $V_R + \phi_\Delta(z_0, t) = 0$ , additional current component  $I_\Delta(z_0, t)$  can be obtained as,

$$\begin{aligned} I_\Delta(z_0, t) &= \frac{-2R}{Z_s(t-t_0) + R} I_a(z_0, t) \\ &= \frac{-2R}{Z_s(t-t_0) + R} I_s(t-t_0) \cdot p_a(z_0, t) \end{aligned} \quad (3.37)$$

where  $Z_s(t) = Z_a(0, t)$  and  $t_0 = z_0/c$ .

Conventionally, the reflection coefficient  $\beta$  of the surge current can be defined as,

$$\beta(z_0, t) = \frac{Z_s(t-t_0) - R}{Z_s(t-t_0) + R}, \quad (3.38)$$

where  $\beta$  is similar to the traditional reflection coefficient of a TEM line. However, (3.38) is not able to be directly applied to the vertical line since two reflected components shown in (3.33) attenuate at different rates during their upward propagation.

With (3.34) and (3.37), total surge current in (3.32) can be expressed explicitly for  $t \geq t_0$ ,

$$I(z,t) = I_s(t_1)p_a(z,t) + I_s(t_3)p_a(2z_0 - z,t) - I_s(t_3)p_a(z_0,t_2) \frac{2R}{Z_s(t_3) + R} p_a(z_0 - z,t - t_0) \quad (3.39)$$

where  $t_1 = t - z/c$ ,  $t_2 = t - (z_0 - z)/c$  and  $t_3 = t_2 - z_0/c$ .

Noted that electric potential does not attenuate during its propagation [9] on a single conductor, i.e.,  $\phi_a(z,t) = \phi_a(0,t - z/c)$ , the following identities can be obtained

$$\begin{aligned} I_a(z,t)Z_a(z,t) &= I_s(t - z/c)Z_s(t - z/c) \\ p_a(z,t)Z_a(z,t) &= Z_s(t - z/c) \end{aligned} \quad (3.40)$$

The total electric potential on the conductor can be expressed as,

$$\begin{aligned} \phi(z,t) &= I_a(z,t)Z_a(z,t) - I_a(2z_0 - z,t)Z_a(2z_0 - z,t) - I_\Delta(z,t)Z_a(z_0 - z,t - t_0) \\ &= I_s(t_1)Z_s(t_1) - I_s(t_3)Z_s(t_3) \cdot \left( 1 - \frac{2R \cdot p_a(z_0,t_2)}{Z_s(t_3) + R} \right) \end{aligned} \quad (3.41)$$

Electric potential and surge current on the grounded conductor have been yielded with (3.40) assuming that characteristic parameters  $p_a(z,t)$  and  $Z_a(z,t)$  of a vertical line have been given. In this section, simulation results of the surges on the line shown in Fig. 14(a) will be presented. In the simulation, the ground is located at  $z_0=120$  m. The conductor radius is equal to 20 mm. The source current has the 10 kA magnitude and the 0.25/100  $\mu$ s waveform.

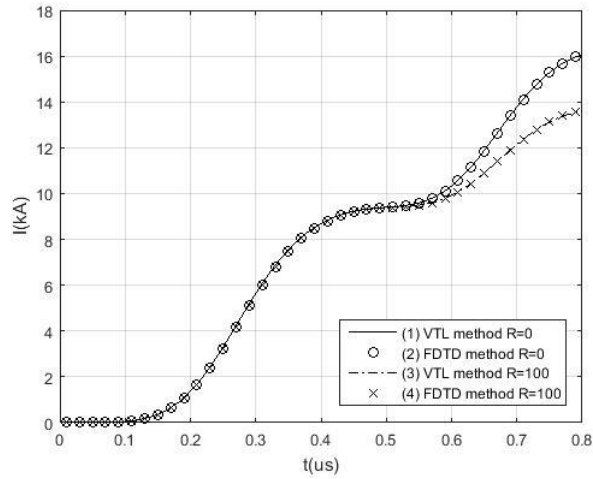


Fig. 3.15a Surge currents calculated with the FDTD method and with (3.40)

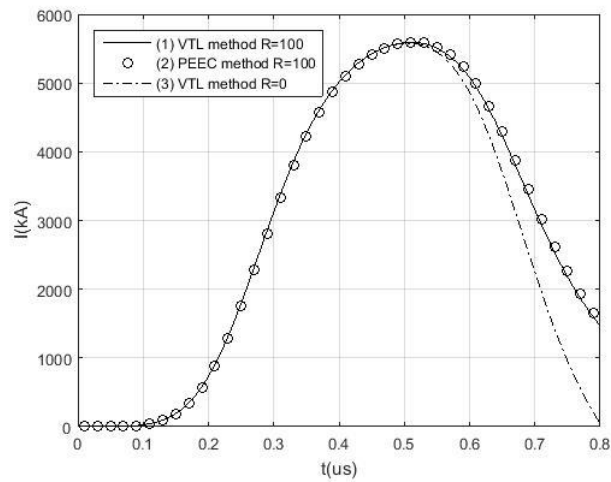


Fig. 3.15b Electric potentials calculated with the PEEC method and with (3.40)

To validate the proposed formulas, the comparison with the FDTD [73] or the PEEC method [74] has been performed. The FDTD method is generally applicable to surge current analysis exclusively. Fig.3.15a and Fig.3.15b show the surge current and electric potential at the middle point of the line ( $z=60$  m) calculated by the FDTD method, the PEEC method, and the proposed method (VTL) under an impulse current source. Two different scenarios of grounding resistance have been simulated, i.e., a)  $R=0$  ohm and b)  $R=100$  ohm. It can be observed that the surge current and electric potential match the results from the FDTD and PEEC methods very well. The average error of the surge current and electric potential is generally less than 1%.

## 3.6 The Extended TDTW Theory for a Conductor with a Discontinuity

### 3.6.1 Center-fed dipole line structure

Shown in Fig. 1 is the configuration of a center-fed perfectly-conducting thin-wire dipole aligned in the  $z$ -direction. Current source  $I_s(t)$  is applied at  $t = 0$  and  $z = 0$  in series with wire  $a$  of radius  $r_a$  and wire  $b$  radius  $r_b$ . This source generates two current waves propagating outwards along these wires.

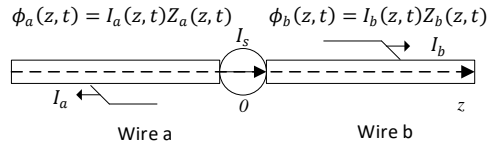


Fig. 3.16 Wave propagation in a center-fed line dipole

It is noted in [70] that current waves attenuate during their propagation in a dipole with  $r_a = r_b$ . While the waves of electric scalar and magnetic vector potentials propagate without any attenuation. These parameters are uniquely determined by the transient characteristic impedance  $Z_x(z, t)$  ( $x = a$  or  $b$ ) of the dipole under a ramp current source. The characteristic equations for a dipole in Fig. 1 are then given by

$$\begin{aligned}\phi_x(z, t) &= \pm Z_x(z, t) \cdot I_x(z, t) \\ I_x(z, t) &= Z_x(0, t - z/c) / Z_x(z, t) \cdot I_s(t)\end{aligned}\quad (3.42)$$

where both  $\phi_x(z, t)$  and  $I_x(z, t)$  are the scalar potential and current waves propagating in wire  $x$ . The minus sign in (1) is taken when potential  $\phi$  propagates in the  $-z$ -direction.  $c$  is the speed of light in free space. With (3.42) attenuation coefficient  $p$  of current in a dipole is then expressed by

$$\begin{aligned}p_x(z, t) &= I_x(z, t) / I_s(t - z/c) \\ &= Z_x(0, t - z/c) / Z_x(z, t)\end{aligned}\quad (3.43)$$

Transient impedance  $Z_x(z, t)$  varies temporally and spatially along the wire. It is uniquely determined by the wire radius and can be numerically evaluated with an iterative procedure [70]. The simplified formula of  $Z_x(z, t)$  is also available, and is presented in (A4) in Appendix A. According to Appendix B, (1) holds even if  $r_a \neq$

$r_b$ . Transient impedance in wire  $x$  can be evaluated by assuming the radius  $r_x$  everywhere in the dipole.

### 3.6.2 Dipole line with a discontinuity

Fig. 3.17 shows the dipole with line discontinuity caused by a change of wire radius at  $z = z_0$ . The dipole is fed by the current source  $I_s(t)$  applied at  $t = 0$  and  $z = 0$ . The line with the discontinuity could be connected to the ground, but the reflected surge from the ground has not arrived yet in the analysis.

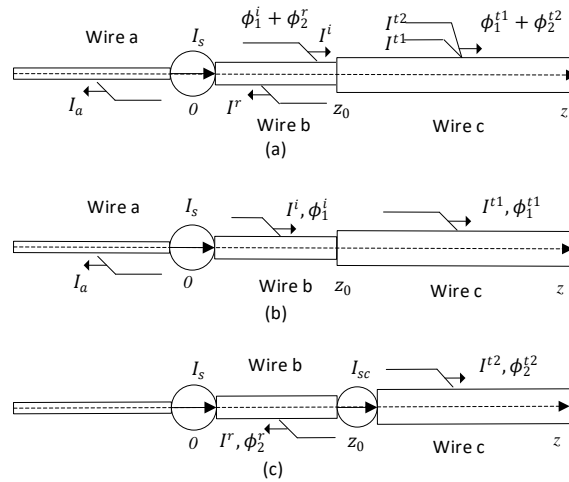


Fig. 3.17 Configuration of the dipole with a line discontinuity (a) Current waves resulted from the line discontinuity. (b) Configuration for evaluating waves  $\phi_1, I^i$  and  $I^{t1}$  (c) Configuration for evaluating waves  $\phi_2, I^r$  and  $I^{t2}$ .

The current source in Fig. 3.17(a) generates an incident current surge  $I^i$  propagating towards the discontinuity ( $z = z_0$ ). When the incident surge arrives at the discontinuity, both reflected surge and transmitted surge will be generated and propagate away from the discontinuity along wires  $a$  and  $b$ . For the convenience of analysis, the transmitted surge is split into two components  $I^{t1}$  and  $I^{t2}$ . These components at  $z = z_0$  are respectively equal to the incident and reflected surges  $I^i$  and  $I^r$ .

Note that the scalar potential in a dipole can be evaluated with the following formula [75],

$$\phi(z, t) = \frac{\mu_0}{4\pi} \int_z^{\infty} \frac{\partial}{\partial t} \int_{(l'-ct)/2}^{(l'+ct)/2} \frac{I(l', t - |l' - l|/c)}{\sqrt{(l' - l)^2 + r^2}} dl' dl \quad (3.44)$$

where  $I(l', t)$  is the total current in the dipole, which is composed of four current components mentioned above. The original model in Fig. 3.17(a) is then replaced with two pairs of currents propagating on these wires independently, i.e.,  $I^i$  and  $I^{t1}$ ,  $I^r$  and  $I^{t2}$  as shown in Fig. 3.17(b) and Fig. 3.17(c). In this case,  $I^i(z_0, t) = I^{t1}(z_0, t)$  and  $I^r(z_0, t) = I^{t2}(z_0, t)$ .

In Fig. 3.17(c), an additional dipole current source  $I_{sc}$  is introduced so that the current continues at the discontinuity. Now the configuration in Fig 3.17(c) is the same as that of a dipole shown in Fig. 1. Scalar potentials in this configuration are expressed by  $= I_r(z_0, t)$

$$\begin{aligned}\phi^r(z, t) &= I^r(z, t)Z_b(-\zeta, \tau) \\ \phi^{t2}(z, t) &= I^{t2}(z, t)Z_c(\zeta, \tau)\end{aligned}\quad (3.45)$$

where  $\zeta = z - z_0$ ,  $\tau = |t - t_0|$ ,  $z_0 = ct_0$  and  $t_0 = z_0/c$ . Both  $Z_b(-\zeta, \tau)$  and  $Z_c(\zeta, \tau)$  are the dipole impedances with arm radius of  $r_b$  and  $r_c$ , respectively, excited at  $\zeta = 0$  and  $\tau = 0$ .

In Fig. 3.17(b), the pair of current surges  $I^i$  and  $I^{t1}$  propagates in the same direction on wire  $b$  ( $z \leq z_0$ ) and wire  $c$  ( $z \geq z_0$ ), respectively. As stated in Appendix C, the influence of surge  $I^{t2}$  on wire  $c$  on scalar potential  $\phi^i(z, t)$  on wire  $b$  is negligible.  $\phi^i(z, t)$  can be expressed by,

$$\phi^i(z, t) = I^i(z, t)Z_b(z, t) \quad (3.46a)$$

According to Appendix C. The scalar potential  $\phi^{t1}(z, t)$  on wire  $c$  is expressed by,

$$\phi^{t1}(z, t) = I^{t1}(z, t)[Z_c(\zeta, \tau) + Z_{TL}] \quad (3.46b)$$

where  $Z_{TL} = \frac{\mu_0 c}{2\pi} \ln(r_c/r_b)$ .

The total potentials on wire  $b$  and wire  $c$  are contributed by components in Fig. 3.17(b) and (c), and are expressed by

$$\begin{aligned}
\phi_b(z,t) &= \phi^i(z,t) + \phi^r(z,t) \\
&= I^i(z,t)Z_b(z,t) + I^r(z,t)Z_b(\zeta,\tau) \\
\phi_c(z,t) &= \phi^{t1}(z,t) + \phi^{t2}(z,t) \\
&= I^{t1}(z,t)[Z_b(z,t) - Z_{TL}] + I^{t2}(z,t)Z_c(\zeta,\tau)
\end{aligned} \tag{3.47}$$

Note that dipole source current  $I_{sc}(\tau) = I^r(z_0, \tau) = I^{t2}(z_0, \tau)$  at the discontinuity. It can be obtained by equaling (3.46a) and (3.46b) with boundary condition  $I^i(z_0, t) = I^{t1}(z_0, t)$  as mentioned before. With incident current  $I^i$  it is expressed as,

$$\begin{aligned}
I_{sc}(\tau) &= I^i(z_0, t)\alpha(t) \\
\alpha(t) &= Z_{TL}/(Z_b(0, \tau) + Z_c(0, \tau))
\end{aligned} \tag{3.48}$$

It is a time-variant reflection coefficient expressed with a ratio of dipole impedances at the position  $z = z_0$ . Note that the reflection coefficient is only determined by wire radii.

### 3.6.3 Reflection coefficient at the discontinuity with a lumped load

Note that the reflection coefficient of current is generally determined using the potential balanced equation at the discontinuity. As a general case, a lumped load is inserted in series between two wires at the discontinuity ( $z = z_0$ ). This load can be a resistor ( $R$ ), a capacitor ( $C$ ), an inductor ( $L$ ), or a combination of these elements. A voltage drop  $\Delta\phi(t)$  then is generated across the load when a surge propagates over the discontinuity and can be expressed as

$$\Delta\phi = I(t)R + L\frac{dI(t)}{dt} + \frac{1}{C}\int I(t)dt \tag{3.49}$$

where  $I(t) = I^i(z_0, t) + I^r(z_0, t)$ . It is the total current at the discontinuity. With the ramp waveform for the currents, (3.49) can be simplified, as follows:

$$\begin{aligned}
\Delta\phi &= I(t)Z_{eq} \\
Z_{eq} &= R + L/(t - t_0) + (t - t_0)/2C
\end{aligned} \tag{3.50}$$

where  $Z_{eq}$  is an equivalent impedance of the load used in the time-domain simulation.

Note that potentials at the discontinuity are balanced, i.e.,

$$\phi_b(z_0, t) - \phi_c(z_0, t) = \Delta\phi \quad (3.51)$$

Substituting (3.48), (3.49) and (3.50) into (3.51) yields the reflection coefficient  $\alpha(t)$  of current at the discontinuity, as follows:

$$\alpha(t) = \frac{Z_{TL} - Z_{eq}}{Z_b(0, \tau) + Z_c(0, \tau) + Z_{eq}} \quad (3.52)$$

for  $t \geq t_0$ . Therefore, the reflection coefficient is essentially calculated with dipole impedance at the feeding point and equivalent load impedance at the discontinuity. It is determined by the radii of the wires and is a characteristic parameter of a center-fed dipole.

### 3.6.4 Extended traveling wave theory

As shown early, the surge propagation in a dipole with the line discontinuity can be described with two sets of surges propagating in two-line configurations shown in Fig. 3.17(b) and 3.17(c). given by lossless propagation of scalar potentials on wire  $b$  and  $c$  in the configuration of Fig. 3.17 (b) in appendix D, both  $I^i(z, \tau)$  and  $I^{t1}(z, \tau)$  can be expressed using (3.45) and (3.46) as

$$\begin{aligned} I^i(z, t) &= I_s(t) \cdot \frac{Z_b(0, t - z/c)}{Z_b(z, t)} \\ I^{t1}(z, t) &= I^i(z_0, t) \cdot \frac{Z_b(0, \tau) - Z_{TL}}{Z_b(\xi, \tau) - Z_{TL}} \end{aligned} \quad (3.53)$$

The other two surges emitted by the dipole current source  $I_{sc}(t)$  will propagate again without attenuation. Thus, by using (3.52) the following yields:

$$\begin{aligned} I^r(z, t) &= \alpha(t) I^i(z_0, t) \cdot \frac{Z_b(0, \tau)}{Z_b(-\xi, \tau)} \\ I^{t2}(z, t) &= \alpha(t) I^i(z_0, t) \cdot \frac{Z_c(0, \tau)}{Z_c(\xi, \tau)} \end{aligned} \quad (3.54)$$

Here,  $Z_x(0, \tau)$  is the dipole impedance on wire  $x$  at the feeding point.

For the sake of simplicity, a time-domain full-wave attenuation coefficient  $K$  of the traveling wave is introduced, as follows:

$$K_x(u, v) = \frac{Z_x(0, v) - a_0}{Z_x(u, v) - a_0} \quad (3.55)$$

where  $a_0 = Z_{TL}$  for the  $I^{t1}$  component, otherwise  $a_0 = 0$ . This parameter looks like an attenuation coefficient but varies for surge components and wire geometry at the discontinuity. Then, four current surges can be expressed, as follows:

$$\begin{aligned} I^i(z, t) &= I_s(t)K_b(z, t - z/c) \\ I^r(z, t) &= \alpha(t)I^i(z_0, t) \cdot K_b(\xi, \tau) \\ I^{t1}(z, t) &= I^i(z_0, t) \cdot K_c(-\xi, \tau) \\ I^{t2}(z, t) &= \alpha(t)I^i(z_0, t) \cdot K_c(\xi, \tau) \end{aligned} \quad (3.56)$$

Surge propagation over line discontinuity can then be described graphically. Fig. 3.18 shows the traveling wave theory for wave propagation on the dipole with line discontinuity, which is physically similar to that for the TEM wave propagation. When the incident current  $I^i(z, t)$  travels to the position of discontinuity, two transmitted current surges, and one reflected current surge emerge. The propagation of these generated surges around the discontinuity is governed by both the reflection coefficient  $\alpha(t)$  and generalized attenuation coefficient  $K_x(z, t, d)$ , which are fundamentally determined by dipole impedances and the position of the discontinuity on the dipole.

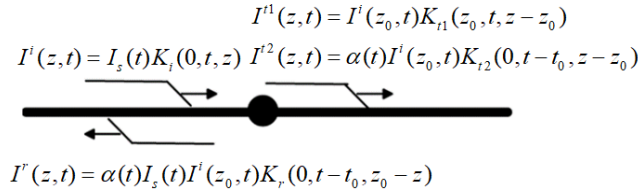


Fig. 3.18 Travelling Wave Theory for the dipole with a discontinuity

The proposed procedure has been implemented on the platform of MATLAB and applied to evaluate surges in a dipole structure with line discontinuity. Numerical validation was then made by comparing the results with the results obtained from the FDTD or PEEC method [76].

The wire structure selected for surge evaluation consists of three wires:  $a$ ,  $b$  and  $c$ , as illustrated in Fig. 3.19(a). The dimensions of these wires are given in Table 1. The current source has a ramp function and is placed in series with wire  $a$  and wire  $b$ . The discontinuity is located at  $z = z_0$  between wire  $b$  and wire  $c$ . At the

discontinuity, a lumped load is connected. This load can be either (a) a resistor with  $R= 500 \Omega$ , (b) an inductor with  $L=10 \mu\text{H}$ , or (c) a capacitor with  $C=100 \mu\text{F}$ .

Table.3.1 wire dimensions of a dipole structure

	Wire <i>a</i>	Wire <i>b</i>	Wire <i>c</i>
Length (m)	120	60	120
Radius (mm)	20	20	5

As discussed in previous sections, surge propagation in a dipole structure can be fully described with dipole impedances evaluated with (6). Fig. 3.20 and 3.21 show the reflection coefficient of current at the discontinuity with different lumped loads using this proposed method and the PEEC method [76]. The curves of the reflection coefficient up to  $0.4 \mu\text{s}$  are plotted in the figures. It is found that the reflection coefficient matches well with the results obtained from the PEEC method in all four cases. It is noted in Fig. 3.20 that the reflection coefficient generally does not varies with time significantly. The reflection coefficient is approximately equal to  $-0.1$  for  $R=0$  and increased negatively to  $-0.4$  for  $R=500\text{ohm}$ . Fig. 3.21 shows the reflection coefficient of current when an inductor or a capacitor is connected at the discontinuity. Similar results are observed.

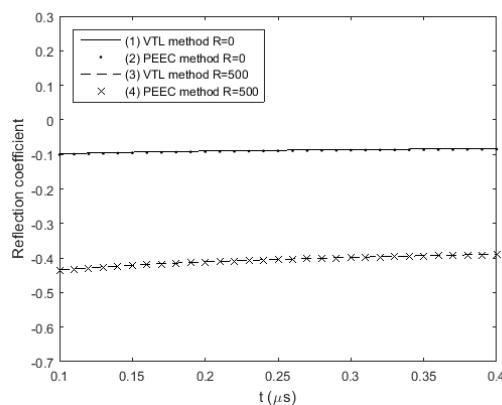


Fig. 3.20 Reflection coefficients with a resistance connected at the discontinuity ( $R=0$  ohm and  $500$  ohms)

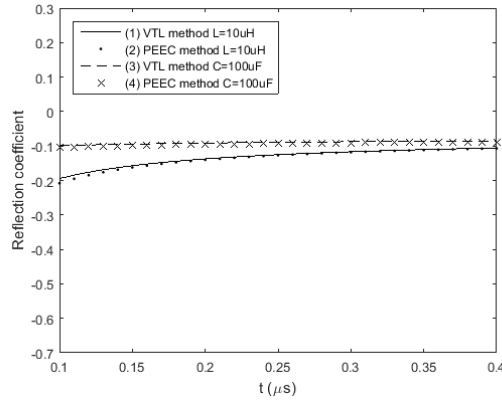


Fig. 3.21 Reflection coefficients with an inductance and a capacitance connected at the discontinuity ( $L=10 \mu\text{H}$  and  $C= 100 \mu\text{F}$ )

Fig. 3.22 shows surge currents in both wires  $a$  and  $b$  calculated with the proposed method and the FDTD method. The load connected at the discontinuity has a 500-ohm resistance. In this case, surge currents at two positions P1 ( $z=45\text{m}$ ) and P2 ( $z=75\text{m}$ ) of upper and lower wires were respectively recorded, that is, 15m away from the discontinuity. For comparison, the source current with a ramp waveform is also plotted in the figure. It is found that the results obtained from the two methods match well, and the average difference is generally less than 1%. The surge current in the wire is contributed by both the incident surge and reflected surge from the discontinuity. It is clear to see in Fig. 5 that the reflected surge arrives at P1 at  $t=0.1\mu\text{s}$ . Note that the surge currents in wires  $a$  and  $b$  are less than the source current. This is due to both the current attenuation during its propagation and the surge reflection at the discontinuity.

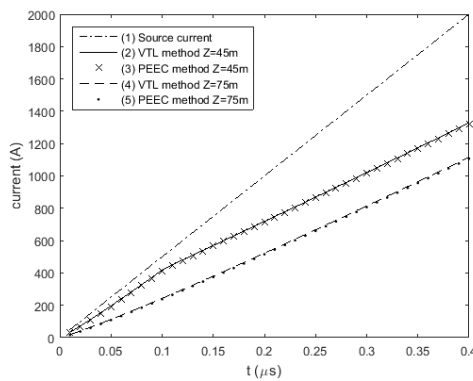


Fig.3.22 surge currents at  $z=45\text{m}$  in wire  $a$  and at  $z=75\text{m}$  in wire  $b$  with resistance at the discontinuity ( $R=500 \text{ ohm}$ )

Simulation of surges in a grounded dipole structure, as shown in Fig. 3.19(b) is also performed. This mimics a grounded vertical structure with a grounding resistance of 100 ohms struck by lightning under excitation of an arbitrary waveform current. In this case, the load connected at the discontinuity has zero resistance. The source current has a rising time of 0.2  $\mu$ s, and a magnitude of 10kA. Both surge currents in wires *a* and *b* are calculated with the proposed method. By simply adding a time delay in (25) and (26) for each component of the current source, resultant surge currents in wires *a* and *b* are obtained by summing all these surge components together using (27). The results are presented in Fig. 3.22. The surge currents calculated with the FDTD method are presented in Fig. 3.22 as well for comparison. It is found that these results from the two methods match well, with an average difference of less than 1%. It is noted that simulation time in a PC with i7-4790 CPU at 3.6GHz and 16GB RAM is 27.5 sec. with the iterative method, and 30min with the FDTD method.

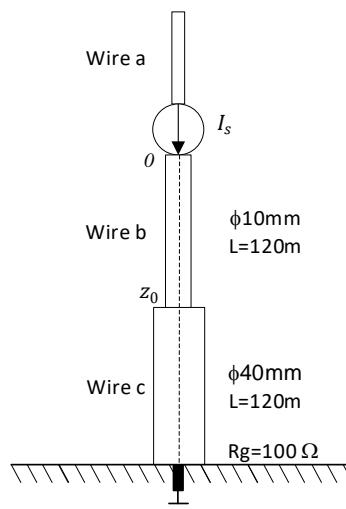
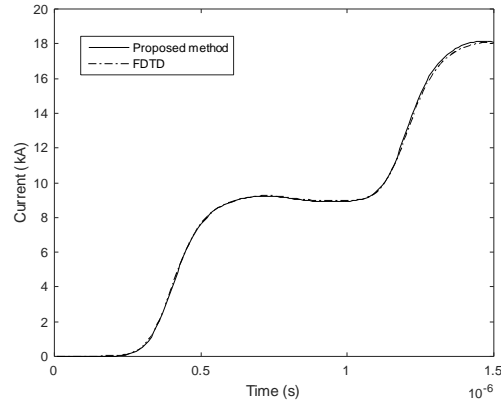
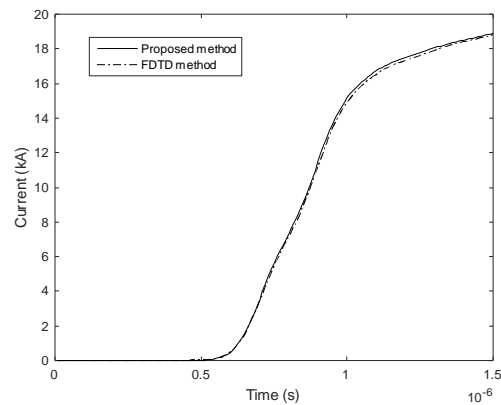


Fig. 3.23 configuration of a vertical structure struck by lightning

It is found that surge potentials and currents around the discontinuity are completely determined by characteristic parameters of a line, that is, surge impedance, attenuation coefficient, and reflection coefficient under a ramp current source. With the reflection coefficient, surges on the conductors can be evaluated directly, even if the source current has an arbitrary waveform. The formulas presented in the paper have been validated numerically with the FDTD method. Good agreements have been observed.



(a) Surge current in wire *a* at  $z=90\text{m}$



(b) Surge current in wire *b* at  $z=150\text{m}$

Fig.3.24 surge current with an impulse-wave source current with 100Ohm grounding resistance

### 3.7 The Extended TDTW Theory for a Grounded Multi-level Tower

The grounding resistance and characteristic parameters of a single line, i.e., the attenuation coefficient Transmission towers are of great significance in lightning research, as they are the essential part in the analysis of lightning surges on overhead power lines [77]-[79]. Inappropriate tower modeling may fail to predict the flashover rate [80], and lead to incorrect assessment of hazards to sensitive loads. On the other hand, the resultant current propagating on a tower could be a significant source in the evaluation of lightning-induced electromagnetic pulses (LEMP) [81-82]. The correct current distribution along a tower, therefore, is indispensable in lightning transient analysis.

Research work has been carried out extensively to reveal the tower current distribution using lumped representations. Several models has been proposed, including the single-line model [80], [83-85], multi-conductor model [86-88], multi-story model [89-90]. The simplest representation is based on the transmission line (TL) theory using constant surge impedance and travel time [90]. Note that, the TL theory introduces forward and backward waves along a line as well as the reflection at the boundary, which is of great convenience in its application. Recently the engineering model, which is based on the TL theory, has been widely used in the studies on the lightning strikes to tall structures. The propagation of current is assumed to be TEM-mode and the reflection coefficient at a discontinuity is normally given as a constant [91-92]. It is found in [93] that the ground reflection coefficient is dependent on the waveform and not influenced by the top of the struck object.

In this section, a TDTW theory is developed for the transient analysis of a multi-stage and multi-conductor tower. A generic configuration of the tower and its model are described. Based on this configuration, the wave propagation equations are presented multiple lines in parallel and for the lines with a discontinuity. Closed-form formulas are provided for both the transient impedance and reflection coefficient. The comparison results using the FDTD method are given.

Fig. 25(a) is a multi-stage tower subject to a lightning stroke at its top end. It is known that the lightning return stroke generates two current pulses propagating upwards in the channel, and downwards in the tower. These pulses may be viewed as the incident currents in the channel and tower resulting from a voltage source at the attachment point. With this model, the wave reflection at the channel base can then be fully taken into account in a lightning stroke. This configuration is similar to a dipole fed by a delta-gap voltage source, as shown in Fig. 1.

Note that the tower structure is rotationally-symmetric, as seen in Fig.3.25 (a). All branch currents and scalar potentials are identical at the same height in a stage. The tower structure can then be represented by a set of identical dipole lines running in parallel. Each line has a feed current ( $I_{s1,0}$ ) at  $z = 0$  and a discontinuity between two stages. Fig.3.25 (b) shows the configuration of one representative dipole line, which is deformed at  $z = 0$  and  $z = z_0$ . Note that  $I_{s1,0} = I_{s,0}/n$  where  $n$  is the number of branches in the stage.

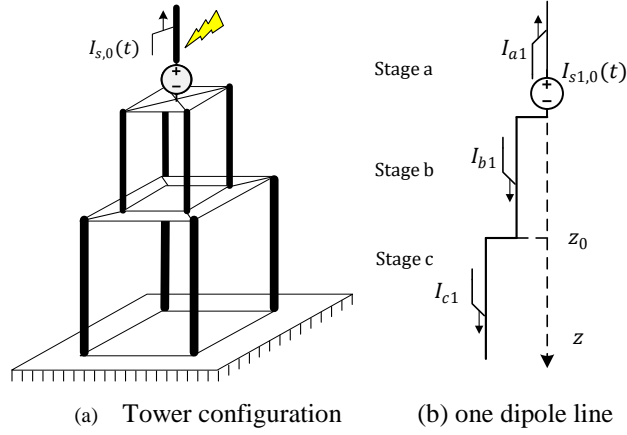


Fig. 3.25 Tower structure and its dipole line model

### 3.7.1 Wave Propagation on a Tower Model with Constant Wire Spacing

Consider a standalone center-fed dipole with two perfectly conducting thin wires of radius  $r_x$ , which is excited by a delta-gap voltage source. With a ramp incident current from the source, current  $I$  propagates with attenuation along the dipole, while scalar potential  $\phi$  propagates without attenuation [70]. These parameters are uniquely determined by transient impedance  $Z$  of the dipole. In wire  $x$  of the dipole, they are described with the following characteristic equations,

$$\begin{aligned}
 \phi_x(z, t) &= \phi_x(0, t - z/c) \\
 &= I_x(z, t)Z_x(z, t) \\
 I_x(z, t) &= I_{s,0}(t - z/c)\alpha_x(z, t)
 \end{aligned} \tag{3.57}$$

where  $c$  is the speed of light, and  $\alpha_x$  is the attenuation coefficient of current give by  $Z_x(0, t - z/c)/Z_x(z, t)$ .  $I_{s,0}(t)$  is the ramp incident current at the feed point ( $z = 0$ ).  $Z_x(z, t)$  can be either evaluated numerically [70] or analytically [76] with (D6) in Appendix D

Now consider a rotationally-symmetric model of  $n$  parallel dipole lines, which is fed separately by  $n$  voltage sources with the ramp current  $I_{s,0}$  ( $I_{s1,0} = I_{s,0}/n$ ) from the source. These dipole lines have a spacing of  $D_{x,ij}$  between lines  $i$  and  $j$ , and a radius of  $r_x$  in stage  $x$  ( $x = a$  or  $b$ ). Fig. 3.26(a) illustrates the configuration of two dipole lines 1 and  $i$  of this model. In the model, the total stage current  $I_{xM}$  is equal to  $nI_{x1}$ , where  $I_{x1}$  is the current of one dipole line in stage  $x$ .

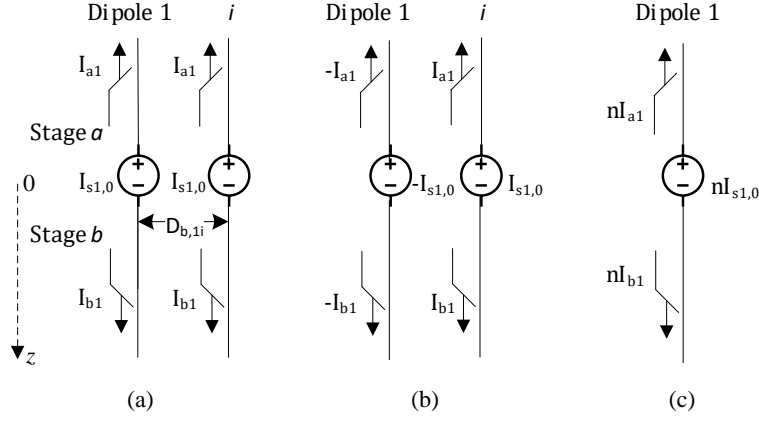


Fig.3.26 Multi-dipole model with constant wire spacing (a) original model, (b) one pair of dipole lines carrying balanced currents (c) single dipole line

It is known in Appendix B that electric potential  $\phi_{xM}$  propagates without attenuation in the model. According to Appendix B,  $\phi_{xM}$  and  $I_{xM}$  in this  $n$ -dipole line model can be expressed using tower transient impedance  $Z_{xM}$ , as follows:

$$\begin{aligned}
 \phi_{xM}(z, t) &= \phi_{xM}(0, t - z/c) \\
 &= I_{xM}(z, t) Z_{xM}(z, t) \\
 I_{xM}(z, t) &= I_{s,0}(t - z/c) \alpha_{xM}(z, t)
 \end{aligned} \tag{3.58}$$

where  $\alpha_{xM}$  is the attenuation coefficient of current in the  $n$ -dipole line model. Both  $\alpha_{xM}$  and  $Z_{xM}$  are given by

$$\begin{aligned}
 \alpha_{xM}(z, t) &= Z_{xM}(0, t - z/c) / Z_{xM}(z, t) \\
 Z_{xM}(z, t) &= Z_x(z, t) - \frac{\mu_0 c}{2\pi n} \sum_{i=2}^n \ln\left(\frac{D_{x,li}}{r_x}\right)
 \end{aligned} \tag{3.59}$$

$Z_x(z, t)$  is the transient impedance of a standalone dipole made of wire  $b$ . Note that both (3.57) and (3.59) are similar. An additional quasi-static transmission line impedance is added for this multi-dipole line structure.

### 3.7.2 Wave Propagation over the Multi-dipole Line Model with a Discontinuity

#### A. Waves at the discontinuity of a dipole line model

Consider the  $n$ -dipole line model with a sudden change of spacing in the parallel wires, as illustrated in Fig. 3.27(a). This dipole model has the spacing of  $D_{b,ij}$  in stage  $b$ , and  $D_{c,ij}$  in stage  $c$ . The change of wire spacing is made at  $z = z_0$ .

Similar to the wave propagation in the standalone dipole with a discontinuity in section 3.6, incident current  $I_{bM}^i$  propagates in stage  $b$  towards the discontinuity. It then generates reflected current  $I_{bM}^r$  in stage  $b$ , and transmitted current  $I_{cM}^t = I_{cM}^{t1} + I_{cM}^{t2}$  in stage  $c$ . These currents are combined into two groups: (1)  $I_{bM}^r$  and  $I_{cM}^{t1}$  and (2)  $I_{bM}^i$  and  $I_{cM}^{t2}$ . Fig. 3.27(b) and 3.27(c) show the configurations for these two sets of the currents. By ignoring the effect of short wires connecting stages  $b$  and  $c$  at  $z = z_0$ , the following boundary conditions are observed,

$$\begin{aligned} I_{bM}^i(z, t) \Big|_{z=z_0} &= I_{cM}^{t1}(z, t) \Big|_{z=z_0} \\ I_{bM}^r(\zeta, \tau) \Big|_{\zeta=0} &= I_{cM}^{t2}(\zeta, \tau) \Big|_{\zeta=0} \end{aligned} \quad (3.60)$$

where  $\zeta = z - z_0$ ,  $\tau = t - t_0$  and  $t_0 = z_0/c$ .

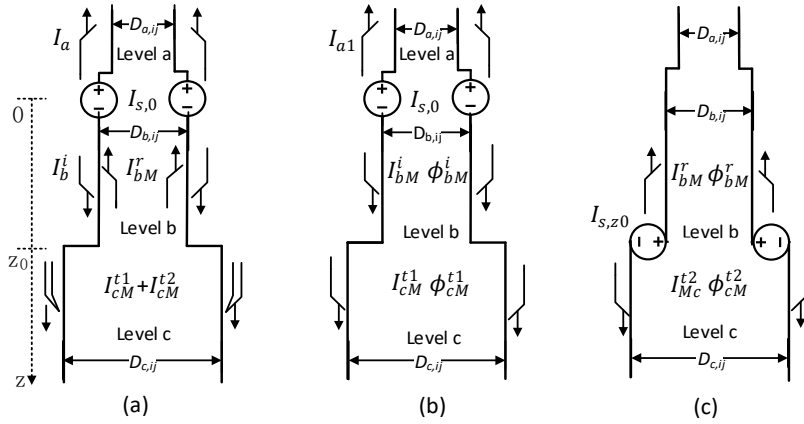


Fig. 3.27 Multi-dipole line model with a change of wire spacing (a) original model, (b) config. of  $I_{bM}^r$  and  $I_{cM}^{t1}$ , and (c) config. of  $I_{bM}^i$  and  $I_{cM}^{t2}$ .

In the configuration shown in Fig. 3.27(b), as indicated in Appendix E, both scalar potential  $\phi_{bM}^i(z, t)$  and  $\phi_{cM}^{t1}(z, t)$  are expressed respectively using corresponding branch currents  $I_{bM}^i$  and  $I_{cM}^{t1}$  in their stages, as follows:

$$\begin{aligned} \phi_{bM}^i(z, t) &= I_{bM}^i(z, t) Z_{bM}(z, t) \\ \phi_{cM}^{t1}(z, t) &= I_{cM}^{t1}(z, t) Z_{cM}(z, t) \end{aligned} \quad (3.61)$$

where  $Z_{xM}(z, t)$  is the transient impedance of a multi-dipole line model with the same geometry as the wires in stage  $x$ . This indicates that both potential and current in a tower stage can be evaluated using a multi-dipole line model with constant spacing.

In Fig. 3.27(c), a set of voltage sources is inserted between stages  $b$  and  $c$  so that the currents in the dipole lines are continuous at the discontinuity. In this case the incident current  $I_{s,z_0}(\tau)$  from the virtual sources is equal to  $I_{bM}^r(z_0, \tau)$  or  $I_{bM}^{t2}(z_0, \tau)$ , and is activated after the wave arrives at  $z_0$ . This configuration is similar to the one shown in Section 3.6. According to Appendix E, both  $\phi_{bM}^r$  and  $\phi_{cM}^{t2}$  are expressed with transient impedance  $Z_{xM}$  as

$$\begin{aligned}\phi_{bM}^r(\zeta, \tau) &= -I_{s,z_0}(\tau)Z_{bM}(-\zeta, \tau) \\ \phi_{cM}^{t2}(\zeta, \tau) &= I_{s,z_0}(\tau)Z_{cM}(\zeta, \tau)\end{aligned}\quad (3.62)$$

### B. Reflection coefficient at the discontinuity

It is noteworthy that the potential at the position  $z = z_0$  in this configuration is continuous, i.e.,  $\phi_{bM}^i + \phi_{bM}^r = \phi_{cM}^{t1} + \phi_{cM}^{t2}$  at  $z = z_0$ . With (3.61) and (3.62), the following equation for the reflection coefficient  $\gamma_{z_0}(\tau)$  is obtained,

$$\gamma_{z_0}(\tau) = \frac{I_{sc}(\tau)}{I_{bM}^i(z_0, t - z_0/c)} = \frac{Z_{bM}(z_0, t) - Z_{cM}(z_0, t)}{Z_{bM}(0, \tau) + Z_{cM}(0, \tau)} \quad (3.63a)$$

Expression (3.63a) is similar to the reflection coefficient defined in traditional traveling wave theory, in which the impedance is constant. Note that with (C5) in appendix C, (3.63a) can be further written as

$$\gamma_{z_0}(\tau) = \frac{\mu_0 c}{2\pi} \frac{\ln\left(\frac{r_c}{r_b}\right) - \frac{1}{n} \sum_{i=2}^n \ln\left(\frac{r_c}{r_b} \cdot \frac{D_{b,li}}{D_{c,li}}\right)}{Z_{bM}(0, \tau) + Z_{cM}(0, \tau)} \quad (3.63b)$$

Note that the reflection coefficient is only decided by radius, spacing distance, and input impedance at the point of discontinuity, this is in coincidence with the experimental study in [93].

### C. Traveling wave theory for the multi-dipole line model with a discontinuity

As seen in Appendix D, the propagation of scalar potentials in a set of perfectly conducting wires is lossless. It can then be stated that the propagation of  $\phi_{bM}^r$  and  $\phi_{cM}^{t2}$  in Fig. 3.27(c) is lossless, as well as  $\phi_{bM}^i$  and  $\phi_{cM}^{t1}$  in Fig. 3.27(b). Therefore,

both  $I_{bM}^i$  and  $I_{cM}^{t1}$  are obtained with (3.61), and are expressed with the source current as

$$\begin{aligned} I_{bM}^i(z, t) &= I_{s,0}(t - z/c) \cdot \alpha_{bM}(z, t) \\ I_{cM}^{t1}(z, t) &= I_{bM}^i(z_0, t) / \alpha_{cM}(z_0, t) \cdot \alpha_{cM}(z, t) \end{aligned} \quad (3.64)$$

With (3.62) the following is obtained,

$$\begin{aligned} I_{bM}^r(\zeta, \tau) &= I_{s,z0}(\tau) \cdot \alpha_{bM}(\zeta, \tau) \\ I_{cM}^{t2}(\zeta, \tau) &= I_{s,z0}(\tau) \cdot \alpha_{cM}(\zeta, \tau) \\ I_{s,z0}(\tau) &= \gamma_{z0}(\tau) I_{bM}^i(z_0, \tau) \end{aligned} \quad (3.65)$$

Now introduce coefficients  $\alpha_{x,zs}^*(z, t')$  and  $\gamma_{zs}^*(z, t')$  expressed with time  $t'$ , given by a source at  $z = zs$ .  $t'$  is the time counting after the wave arrives at point  $z$ , for example,  $\alpha_{x,zs}^*(z, t') = \alpha_x(z, t)|_{t=t'+\Delta t}$ , where  $\Delta t$  is the travel time of a wave from the source point ( $zs$ ) to the field point ( $z$ ). Both (3.64) and (3.65) then are revised to be

$$\begin{aligned} I_b^i(z, t) &= I_{s,0}^*(t') \cdot \alpha_{b,0}^*(z, t') \\ I_c^{t1}(z, t) &= I_{s,0}^*(t') \cdot \alpha_{c,0}^*(z, t') \cdot C_{b/c,0}^*(z_0, t') \\ I_b^r(\zeta, \tau) &= I_{s,0}^*(t') \cdot \alpha_{b,z0}^*(\zeta, t') \\ I_c^{t2}(\zeta, \tau) &= I_{s,0}^*(t') \cdot \alpha_{c,z0}^*(\zeta, t') \end{aligned} \quad (3.66)$$

where correction factor  $C_{b/c,0}^*(z_0, t')$  is defined as  $\alpha_{b,0}^*(z_0, t') / \alpha_{c,0}^*(z_0, t')$ , arising at the discontinuity ( $z_0$ ) for the source at  $z = 0$ . All the currents in wires  $b$  and  $c$  in (3.66) are expressed with local time  $t'$  accounting after the wave arrives at field point  $z$ .

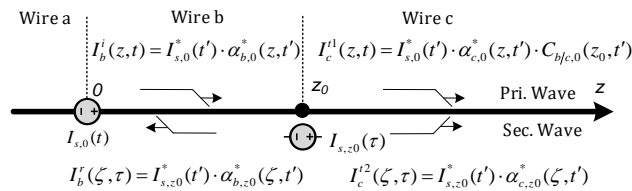


Fig. 3.28 Traveling wave theory for the dipole line model with a discontinuity

Wave propagation over a line discontinuity in the multi-dipole model can then be described graphically. Fig. 3.28 depicts the traveling wave theory for wave

propagation on the dipole line model. The incident current  $I^i$  travels with attenuation towards the discontinuity. After the discontinuity, it continues to propagate as  $I^{t1}$  with a new attenuation coefficient multiples by a correction factor. This wave is called the primary wave. A pair of secondary wavers  $I^r$  and  $I^{t2}$  are generated at the discontinuity. This case is similar to a delta-gap dipole fed with the incident current  $I_{s,z0}$ .

## 3.8 Applications

### 3.8.1 Dipole antenna with a lumped loading

The expression of current in cylindrical antennas has been addressed for a long time [94-97]. Hallén [98] derived an integral equation in the Fourier domain for the outward traveling wave on a perfectly conducting dipole antenna. The simplified solutions in both time and frequency domains were given by Bogerd in [100]. It is found that the approximate frequency-domain solution is generally consistent with the numerical result of Hallen's integral equation. However, a larger difference was found in the time-domain solution of Hallen's integral equation. The reason may be the constant value approximation for both the time- and space-varying admittance.

Traveling wave antennas constructed using a loading technique [101] are desirable in some practical situations [102]. It was stated in [103] that because of the broad frequency band of the short-pulsed fields, direct treatment of the antennas in the time-domain may lead to more efficient and physically transparent representations. It is noted that analysis [104-105] and optimization [106-107] of the radiated pulsed energy in a given direction have been performed in the time-domain. However, time-domain traveling wave analysis for the dipole antenna with lumped loads or a discontinuity has not been addressed significantly.

Recently, the lumped circuit model has been developed to determine the impedance of line antennas under different situations [108-109]. An accurate determination of the input impedance is essential for designing an appropriate matching network to obtain the maximum radiation efficiency, especially at or near the first resonance [108]. Numerical methods such as the finite-difference time-domain method (FDTD) [90-93] and time-domain-integral-equations [94-95] have been developed to evaluate the input impedance and the radiated electromagnetic

field of a dipole antenna. Generally speaking, these methods could deal with problems with complex geometry and material properties. To address the wave propagation over a line discontinuity, several types of impedances at the discontinuity have been introduced. These impedances were numerically investigated using the PEEC method [97-98] and were applied to reveal the relationship among the waves arising at the discontinuity. However, generalized mathematical models for such impedances in time-domain are not available. Insights on the wave propagation on a line dipole are not available either.

In this section, the TDTW theory is used for the wave propagation in a line dipole, fed by a delta-gap voltage source. The dipole has a line discontinuity caused by a sudden change of wire radius or a lumped load.

Fig. 3.29 shows the configuration of a center-fed perfectly-conducting thin-wire dipole aligned in the  $z$ -direction. A delta-gap voltage source with current  $I_s(t)$  is applied at  $t = 0$  and  $z = 0$  in series with wire  $a$  of radius  $r_a$  and wire  $b$  of radius  $r_b$ . This source generates two current waves propagating outwards along these wires.

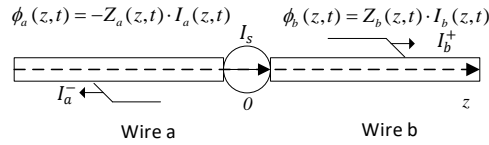


Fig. 3.29 Wave propagation in a center-fed line dipole

Theoretically, this dipole can be described by the 1-D wave equation of vector potential  $A$  in the time domain, as follows [103]:

$$\frac{\partial^2 A(z,t)}{\partial z^2} = \frac{1}{c^2} \frac{\partial^2 A(z,t)}{\partial t^2} \quad (3.67)$$

where  $c$  is the speed of light in free space. Note that the identity of holds  $A(z,t) = \mp c^{-1} \partial A(z,t)/\partial z$  [104]. The signs  $\mp$  are taken respectively for the traveling waves propagating in positive and negative directions from the source. As the axial electric field is zero on a perfect conductor, the electric scalar potential  $\phi$  can be expressed by

$$\phi(z,t) = \pm cA(z,t) \quad (3.68)$$

under zero initial boundary conditions. It is noted in (1-2) that both scalar and vector potentials propagate without attenuation, i.e.,  $A_x(z, t) = A_x(0, t - z/c)$  and  $\phi_x(z, t) = \phi_x(0, t - z/c)$ .

Vector potential  $A$  in a dipole can be also evaluated with the free-space Green's function [17]

$$A(z, t) = \frac{\mu_0}{4\pi} \int_{(z-ct)/2}^{(z+ct)/2} \frac{I(l', t - |l' - z|/c)}{\sqrt{(l' - z)^2 + r^2}} dl' \quad (2.69)$$

where  $I(l', t)$  is the current on the dipole. Under a ramp source current, characteristic equations for the dipole in Fig. 1 was derived with (3) [70], and are given by

$$\begin{aligned} \phi_x(z, t) &= \pm Z_x(z, t) \cdot I_x(z, t) \\ I_x(z, t) &= I_s(t \mp z/c) \cdot Z_x(0, t \mp z/c) / Z_x(z, t) \end{aligned} \quad (3.70)$$

where both  $\phi_x(z, t)$  and  $I_x(z, t)$  ( $x = a$  or  $b$ ) are the scalar potential and current waves propagating in the  $z$  directions in wire  $x$  from the source point.  $Z_x(z, t)$  is the transient characteristic impedance of the dipole, given by the source at  $z = 0$ . With (3.70) attenuation coefficient  $\alpha(t)$  of current in a dipole fed by the source at  $z = 0$  is then expressed by

$$\begin{aligned} \alpha_x(z, t) &= I_x(z, t) / I_s(t \mp z/c) \\ &= Z_x(0, t \mp z/c) / Z_x(z, t) \end{aligned} \quad (3.71)$$

Transient impedance  $Z_x(z, t)$  varies temporally and spatially along the wire. It is uniquely determined by the wire radius and can be numerically evaluated with an iterative procedure [70]. The simplified formula of  $Z_x(z, t)$  is also available, and is presented in (C4) in Appendix C. According to Appendix B, both (3.70) and (3.71) holds even if  $r_a \neq r_b$ . Transient impedance in wire  $x$  can be evaluated by assuming the radius  $r_x$  everywhere in the dipole

The proposed procedure has been implemented on the platform of MATLAB and was applied to evaluate wave propagation in the dipole structure with a discontinuity. Numerical validation was made by comparing the results with the results obtained from the commercial software XFDTD using an FDTD method.

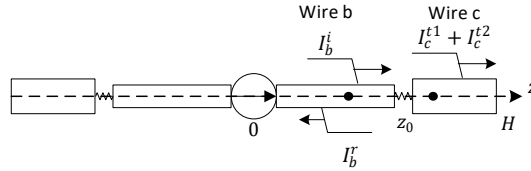


Fig. 3.30 Line dipole with lumped loads

Fig. 3.30 shows a line dipole fed by a delta-gap voltage source with the ramp source current. Each line of the dipole consists of two equal-length wires connected with a lumped load. This load can be either (a) a resistor  $R$ , (b) an inductor  $L$ , or (c) a capacitor  $C$ . In the simulation presented in this section, the dipole has the wires radii of  $r_a = r_b = 5$  mm and  $r_c = 2$  mm.

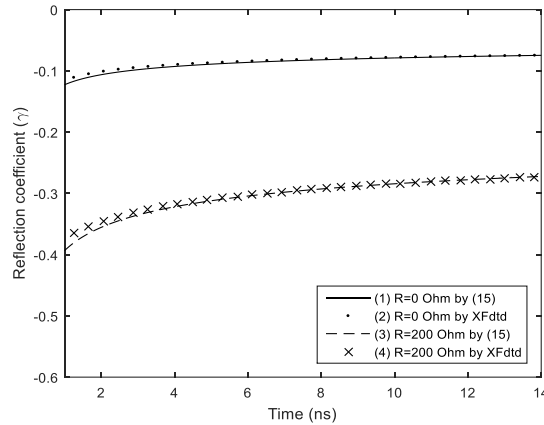


Fig. 3.31 Reflection coefficient with a resistance connected at the discontinuity ( $R=0$  ohm and 200 ohms)

The reflection coefficient of the dipole at the discontinuity is investigated first. As seen in (11) and (15), it is calculated using transient impedances of the dipole and connected load impedance. Note that the transient impedance is calculated with (A5) in Appendix A. Fig. 3.31 and 3.32 show the calculated reflection coefficient of current up to the 14 ns at the discontinuity for different lumped loads. The reflection coefficient for  $R = 0 \Omega$  or  $200 \Omega$  is presented in Fig. 3.31, while that for  $L = 0.5 \mu H$  or  $C = 0.5 nF$  is presented in Fig. 6. Reflection coefficients with different connected loads were also calculated with XFtd, and are presented in these figures. It is found that the results obtained by both methods match well in all four cases.

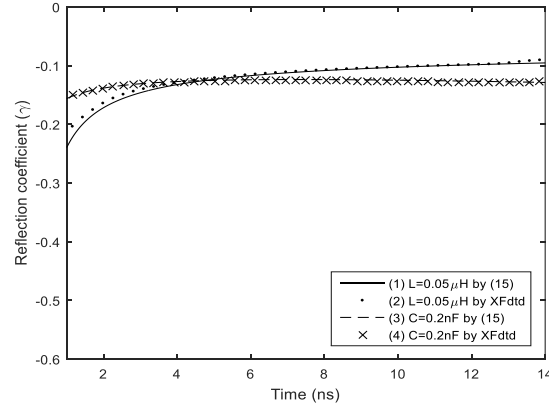


Fig. 3.32 Reflection coefficient with an inductance of  $0.5 \mu H$  or capacitance of  $0.5 nF$  placed connected at the discontinuity

Fig. 3.33 shows the waveforms of currents  $I_b^i$ ,  $I_b^r$  and  $I_c^t$  at the discontinuity of the dipole, calculated with the FDTD method. It is observed that these currents generally have the ramp waveform. Note that the reflection coefficient is the ratio of two currents. It is reasonable to use the ramp waveform assumption in the calculation of the reflection coefficient. This has been illustrated already in Fig. 3.31 and Fig. 3.32.

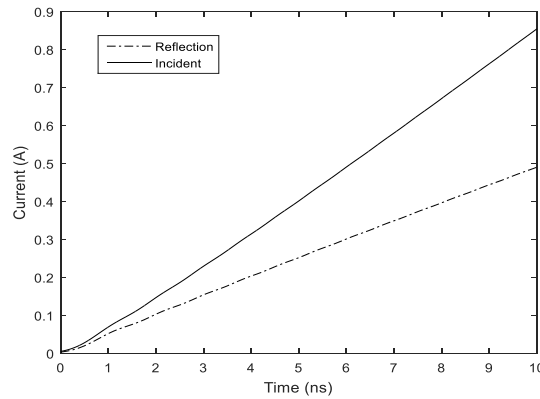


Fig. 3.33 Waveforms of  $I_b^i$ ,  $I_b^r$  and  $I_c^t$  at the discontinuity

Simulation of the transient waves in wire  $b$  of the dipole with resistive loading was also performed. In this case, the dipole was fed by a cosine function modulated Gaussian-pulse delta-gap voltage source, as below:

$$V_s(t) = V_0 \exp(-t^2/2) \cos(2\pi t) \quad (3.72)$$

where the unit of time  $t$  is set to be ns, and  $V_0$  is set to be 1.

Fig. 3.34 illustrates the wave propagation in the dipole using the traveling wave theory. The dipole configuration is illustrated in Fig. 3.30, with a resistance of 100 ohms. For simplicity,  $z_0$  is set to be half of  $H$ , where  $H = 1.2$  m. In Fig. 3.34(a) the incident current wave  $I_1$  generated by the center-fed dipole source propagates in wire  $b$ . The reflected wave  $I_2$  is generated by the lumped element at the discontinuity  $X_1$  and propagates in wire  $b$ , as shown in Fig. 3.34(b). In Fig. 3.34(c), the wave  $I_3$  reflected at the discontinuity  $X_2$  propagates forward in wire  $b$ . In Fig. 3.34(d), both the wave reflected at  $z = H$  and the wave propagating from a point  $X_2$  hit the discontinuity  $X_1$ . They generate the 2<sup>nd</sup> round of reflected and transmitted waves  $I_4$  and  $I_5$  in wires  $b$  and  $c$ . The resultant current in wire  $b$  up to the 2<sup>nd</sup> round of reflection at  $z = z_0$  is evaluated.

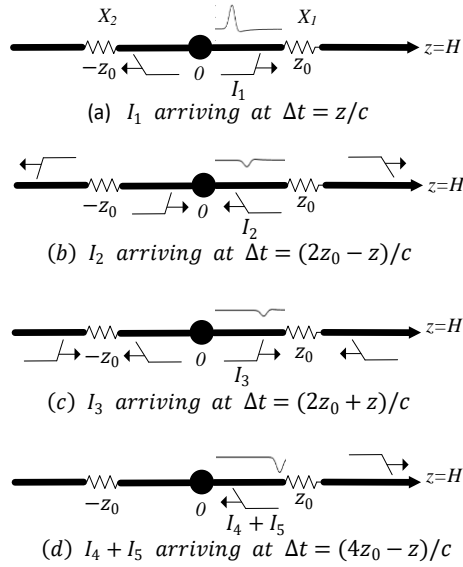


Fig. 3.34 Illustration of the traveling wave theory

These components in wire  $b$  are evaluated first under a ramp source current with (17). The resultant current is obtained by adding all these components, as follows:

$$I(z,t) = \sum_{i=1}^5 I_i(z,t) \quad (3.73)$$

where

$$\begin{aligned}
I_1(z, t) &= I_s^*(t') \alpha_{b,0}^*(z, t') \\
I_2(z, t) &= \gamma_{z_0}^*(t') I_s^*(t') \alpha_{b,0}^*(z_0, t') \alpha_{c,z_0}^*(z_0 - z, t') \\
I_3(z, t) &= \gamma_{-z_0}^*(t') I_s^*(t') \alpha_{b,0}^*(z_0, t') \alpha_{c,-z_0}^*(z_0 + z, t') \\
I_4(z, t) &= \gamma_{z_0}^*(t') I_3(z_0, t + (z_0 - z)/c) \alpha_{b,z_0}^*(z_0 - z, t') \\
I_5(z, t) &= -I_H^*(t') \alpha_{b,2z_0}^*(z_0, t') [\alpha_{b,2z_0}^*(z_0 + z, t') / \alpha_{b,2z_0}^*(z_0, t') \\
&\quad + \gamma_{-z_0}^*(t') \alpha_{b,0}^*(z, t') (z_0 - z, t')]
\end{aligned}$$

and

$$I_H^*(t') = I_s^*(t') \alpha_{b,0}^*(z_0, t') \left[ \frac{\alpha_{c,0}^*(2z_0, t')}{\alpha_{c,0}^*(z_0, t')} + \alpha_{c,z_0}^*(t')(z_0, t') \right]$$

$$\gamma_{z_0}^*(t') = \frac{Z_{TL,cb} - Z_{eq}}{Z_b(0, t') + Z_c(0, t') + Z_{eq}}$$

$$\gamma_{-z_0}^*(t') = \frac{Z_{TL,bc} - Z_{eq}}{Z_b(0, t') + Z_c(0, t') + Z_{eq}}$$

$I_H^*(t')$  is the current reflected at the end of the dipole. The reflection coefficient there is -1.  $\gamma_{z_0}^*(t')$  and  $\gamma_{-z_0}^*(t')$  are the reflection coefficients at points  $z = z_0$  and  $-z_0$  respectively for the waves propagating from the source at  $z = 0$ .

With (3.66), the current of the dipole fed by a modulated Gaussian-pulse voltage source is obtained. Fig. 35 shows the waveforms of the current at  $z = 0.5z_0$  in wire  $b$ , calculated with the proposed method and the XFDTD method. It is found that the results obtained from the two methods match well, with an average difference of 2% at peaks. The waveforms of five traveling waves are illustrated in Fig. 3.35.

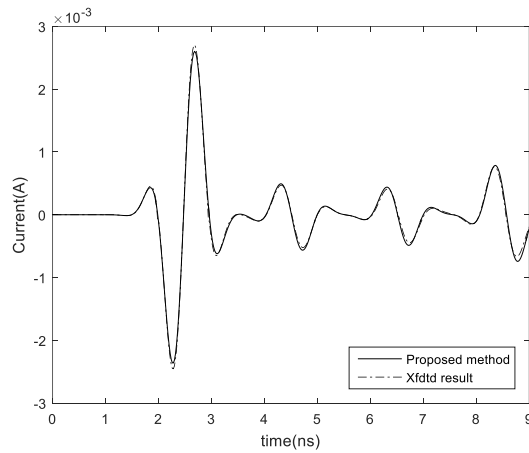


Fig. 3.35 Transient current in a dipole antenna at position  $z = 0.5z_0$  by a Modulated-Gaussian-pulse delta-gap voltage source

### 3.8.2 Lightning strikes on a two-stage tower on the ground

Lightning transient currents in a two-stage tower on the ground, as shown in Fig. 3.36, are simulated with the proposed approach. The tower is 240 m tall with 120 m height in each stage. The conductors have radii of 0.01 m and 0.03 m and wire spacing of 1.2 m and 2.4 m, respectively in the upper and lower stages. The lower stage is connected to a grounding electrode with a resistance of 10 Ohm. The perfect ground is considered for tower modeling [110] and is substituted with the tower image shown in Fig. 3.36.

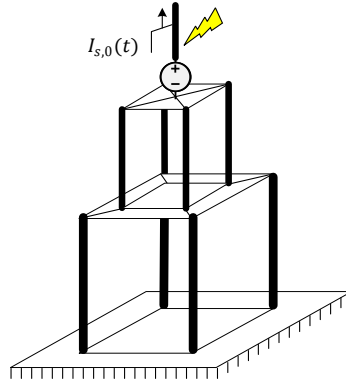


Fig. 3.36 A typical Two-stage Tower structure

The incident current  $I_{s,0}(t)$  resulting from a lightning return stroke has a magnitude of 10 kA and a waveform of 0.25/100  $\mu$ s. It is expressed using Heidler's function [111]. In the simulation, the traveling wave theory is first employed to calculate the transient current  $I_r(t)$  with a ramp incident current. Lightning current  $I_p(t)$  at point  $p$  given by incident current  $I_{s,0}(t)$  then is calculated using a convolution technique presented in section V, as follows:

$$I_p(t) = \frac{d^2 I_{s,0}(t)}{dt^2} * I_r(t) \quad (3.74)$$

As shown in Fig. 3.36, incident current  $I^i$  as a primary wave propagates with attenuation towards the other end of the model. The wave is reflected with  $\gamma_0^*$  at  $z = 0$  or  $2H$ . The subsequent propagation in the model can be viewed as a new primary wave arising from a brand-new source at  $z = 0$  or  $2H$ . Fig. 3.36(a) shows a lattice diagram for the primary waves propagating along the model, which originate at one end of the model. The total attenuation for a wave propagating from one end towards another after three discontinuities is expressed by

$$K(z, t') = \gamma_0^*(t') \alpha_{b,0}^*(z, t') C_{b/c,0}^*(z_0, t') C_{b/c,0}^*(3z_0, t') \quad (3.75)$$

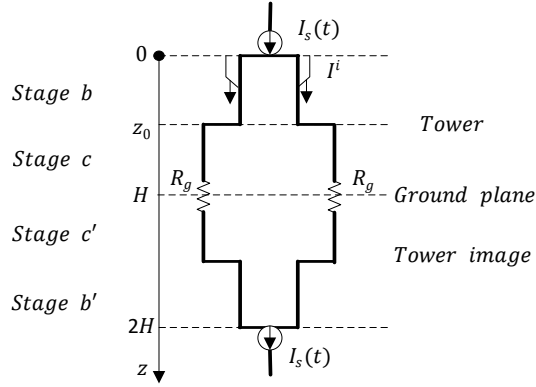
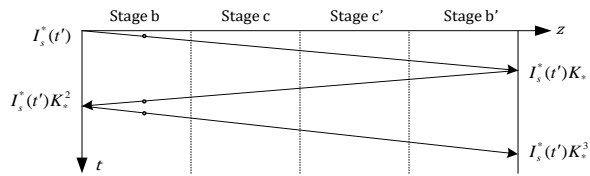


Fig.3.37 Tower model struck by lightning:  $z_0 = 120$  m and  $H = 2z_0$

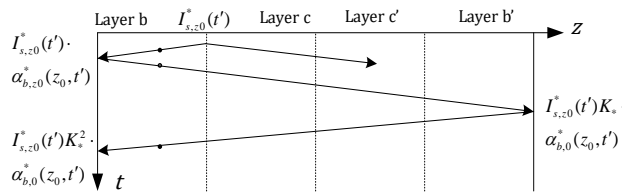
Consider a primary wave arriving at  $z$  in stage  $b$  in the  $n$ th one-way trip in the model. The primary wave  $I_{pri}^{(n)}$  can be expressed with (3.64) and (3.75) as

$$I_{pri}^{(n)}(z, t') = \begin{cases} I_{s,0}^*(t') \alpha_{b,0}^*(z, t') \cdot K^{n-1}(2H, t') & n = 2i \\ I_{s,0}^*(t') K(2H - z, t') \cdot K^{n-1}(2H, t') & n = 2i + 1 \end{cases} \quad (3.76)$$

where  $i = 0, 1, \dots$ .  $K(2H, t')$  is the total attenuation of current in a one-way trip including the reflection at one end. Both  $\alpha_{b,0}^*$  and  $K(2H - z, t')$  are respectively the attenuations from the ends to field point in a one-way trip.



(a) The primary current  $I_{pri,i}$



(b) The 1<sup>st</sup> secondary current  $I_{sec,1a}$

Fig.3.38 Illustration of traveling waves in a 2-stage tower,  $K_* = K(2H, \tau')$

The primary wave will generate a virtual source at each of the discontinuities ( $z = 0, z_0, H, z_0 + H, 2H$ ), which is determined by the reflection coefficient there. Fig. 3.39 shows the reflection coefficients of a current wave at  $z=0, z_0, H$ , and  $z_0 + H$ .

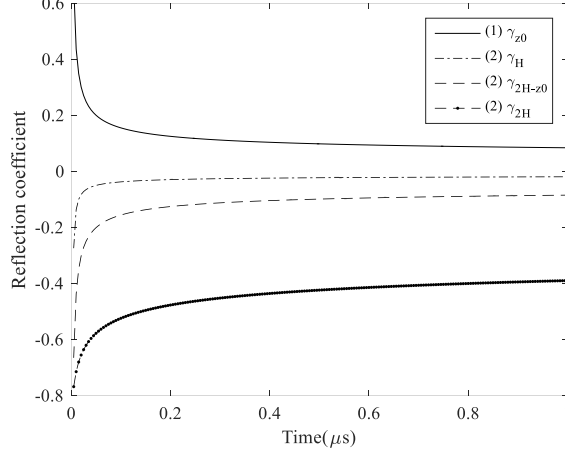


Fig.3.39 Reflection coefficient  $\gamma_{z_0}^*$  between stage b and stage c,  $\gamma_H^*$  at the ground with grounding resistance of 10 Ohm,  $\gamma_{2H-z_0}^*$  between stage c' and stage b' and  $\gamma_{2H}^*$  at the tower top.

At each discontinuity, the virtual source generates a pair of secondary waves propagating in the opposite directions. Similar to the primary wave, these secondary waves will produce a next-level virtual source at each discontinuity they encounter. As the reflection coefficients are generally less than 0.1, as seen in Fig. 3.39, the next-level secondary waves could be neglected. The secondary wave arriving at  $z$  in stage  $b$  after the  $(n-1)th$  full reflection, arising from the 1<sup>st</sup> virtual current source  $z = z_0$ , is expressed by

$$I_{\text{sec},1a}^{(n)}(z, t') = I_{s,0}^*(t') \alpha_{b,0}^*(z_0, t') \cdot \begin{cases} \alpha_{b,0}^*(z_0 - z, t') / \alpha_{b,0}^*(z_0, t') & n = 0 \\ \alpha_{b,0}^*(z, t') K^n(2H, t') & n = 2i + 1 \\ K(2H - z, t') K^n(2H, t') & n = 2i + 2 \end{cases} \quad (3.77)$$

$$I_{\text{sec},1b}^{(n)}(z, t') = I_{s,0}^*(t') \alpha_{b,z_0}^*(3z_0, t') C_{c/b,z_0}(2z_0, t') \begin{cases} K(2H - z, t') K^n(2H, t') & n = 2i + 1 \\ \alpha_{b,0}^*(z, t') K^n(2H, t') & n = 2i + 2 \end{cases} \quad (3.78)$$

where  $i = 0, 1, \dots$ . Fig. 3.38(b) shows a lattice diagram for the propagation of a pair of the secondary waves arising from a virtual source at  $z = z_0$ .

Fig. 3.38(a) illustrates both the primary and secondary waves arriving at  $z = 50\text{ m}$  up to the 3rd one-way trip on the structure. It is found that the 1<sup>st</sup>-level secondary waves are relatively small due to the small reflection coefficient. Their subsequent secondary waves can therefore be ignored. Fig. 3.38(b) shows the curve of the resultant current at the observation point calculated using the traveling wave theory. For comparison, the resultant current calculated with the FDTD method [112-113] is presented in the figure as well. It is found that both curves match very well with the difference of 2%. The non-TEM solution based on the traditional TL is also calculated for comparison. The reflection coefficient at the tower tip is assumed to be  $-0.7$  and at the other discontinuities are zero. A significant difference between the traditional TL theory and the proposed traveling theory is observed.

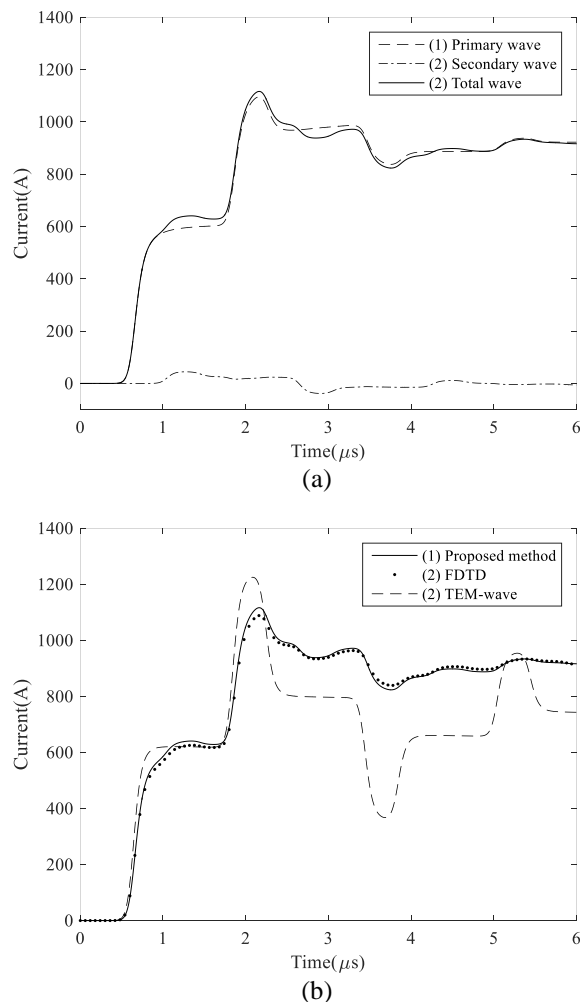


Fig.3.40 Comparison of tower current calculated with the FDTD method and the extended traveling wave theory.

### **3.9 Conclusion**

This chapter presented a theoretical time-domain analysis of lightning transients in a vertical tower. The extended time-domain-traveling-wave (TDTW) theory is introduced. Based on the traditional traveling wave theory, it is extended to formulate the propagation of non-transverse-electromagnetic-mode (non-TEM) waves. The overall mathematical expression is simple and accurate. This theory can be used in a typical dipole antenna with a lumped loading technique and a grounded multi-level stage tower. Once the current distribution is obtained with the closed-form expression, both the radiated electromagnetic field of the antenna and lightning striking object can be computed quickly. From the view of lightning protection, the proposed TDTW theory can be used to build a more general and reasonable engineering model. From the view of antenna design, it can be used to fast calculate the input impedance and radiation pattern of long wire antenna with lumped loading technique.

# 4 The Integrated Model for Lightning Strikes on Ground Structures

In Chapter 4, a novel integrated model for lightning channel and ground structures is proposed. To consider a more comprehensive physical evolution of lightning channel, the advanced DC model of lightning return stroke is proposed and is introduced in this Chapter. The dynamic corona discharge is modeled in section 4.1. Then, to include a more complicated ground structure, the integrated model is proposed based on the advanced DC model and PEEC method. In section 4.3, two typical applications are introduced.

## 4.1 The Enhanced DC Model for Lightning Return Stroke with Dynamic Corona Discharge

The attachment between the downward and upward leaders leads to a transient neutralization process of charges in the corona sheath. The lightning return stroke after the attachment generates two current waves. One propagates upward along the lightning channel and the other one propagates downward along the ground structure. The upward propagating current serves to delivery charges to the corona sheath, which is surrounded by the channel core due to the electrical breakdown. The downward propagating wave is the major threat to the ground structure as well as the surrounded electronic devices.

It is often interesting to determine the current in the ground structure and lightning channel, with the known current at the attachment point. For simplicity, the return stroke is substituted with a charging process arising from a voltage source at that point. In such a way, the charge transferred to the channel will lead to the same current waveform at the attachment point. Note that the difference between these two models is the charge offset which is the initial charge before the attachment. This is the static charge, which affects the static electric field only, not the dynamic charging or discharging current.

Shown in Fig. 4.1 is the configuration of a lightning stroke terminating on a tall structure. Given by the return stroke current at the attachment point, the lightning current in the channel and the ground structure is evaluated. A hybrid model for the

whole system is proposed for the evaluation. In this model, the lightning channel is represented as a thin-wire core surrounded by the corona sheath. A non-linear and non-uniform DC model, similar to that in [114] is adopted. The telegrapher's equations for this DC model are described, as follows:

$$\begin{aligned} -\frac{\partial V(z,t)}{\partial z} &= L_{ch}(z,t) \frac{\partial I(z,t)}{\partial t} + R_{ch}(t) I(z,t) \\ -\frac{\partial I(z,t)}{\partial z} &= C_{ch}(z,t) \frac{\partial V(z,t)}{\partial t} \end{aligned} \quad (4.1)$$

where  $R_{ch}$ ,  $L_{ch}$  and  $C_{ch}$  are the per-unit length resistance, inductance, and capacitance of the lightning channel. They generally vary with time and channel current as well. By neglecting skin effect, the channel resistance is calculated with  $R_{ch}(t) = 1/\sigma\pi r_c^2(t)$ , where  $\sigma$  is the channel conductivity. The core radius  $r_c$  can be expanded radially, and is determined by core current  $i$ , as follows:

$$r_c(t) = \sqrt{(0.25\sigma\xi\rho_0\pi^2)^{-1/3} \int_0^t i(t)^{2/3} dt + r_0^2} \quad (4.2)$$

According to the strong-shock approximation [115]. In (4.2),  $r_0$  is the initial radius corresponding to the leader channel,  $\rho_0$  is the atmospheric density, and  $\xi$  is the factor controlling the expansion rate of the channel proposed in [115].

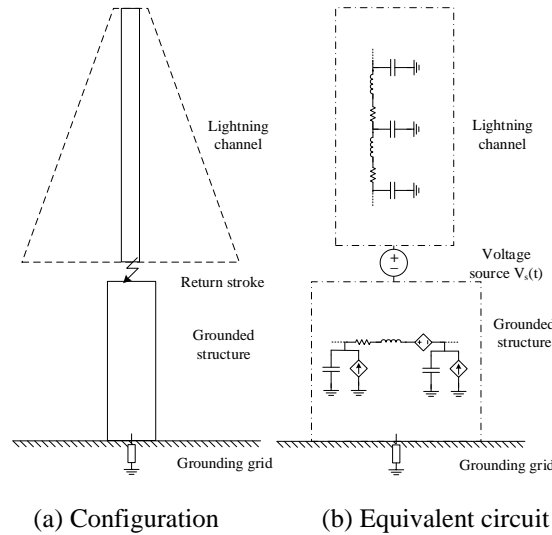


Fig.4.1 Configuration of a lightning channel terminated on a ground structure.

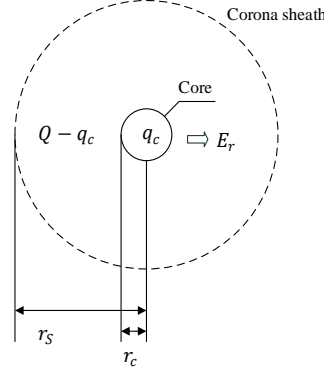


Fig4.2 The modeling of dynamic corona sheath

Both the inductance and capacitance are evaluated with the characteristic impedance  $Z_c$  of the channel [116], and are expressed approximately by

$$\begin{aligned}
 L_{ch}(z,t) &= c^{-1}Z_c(z,t) \\
 C_{ch}(z,t) &= c^{-1}Z_c^{-1}(z,t) \\
 Z_c &= 60\ln(2z/r_c(t))
 \end{aligned} \tag{4.3}$$

The characteristic impedance  $Z_c$  varies with channel height. It is noted in (4.2) that the core radius is a function of the core current in the strong-shock approximation model. Then the core radius varies with time  $t$  and channel height  $z$ . The radius is no longer assumed constant in the distributed model of a lightning channel.

So far, the corona sheath effect is not included in the model. To consider the presence of the corona sheath, the dynamic capacitance due to the existence of a deposited sheath charge shall be added in the model [32]. Thus the channel capacitance is modified as follows:

$$C_{ch}(z,t) = c^{-1}Z_c^{-1}(z,t) + C_{dyn}(z,t) \tag{4.4}$$

where the dynamic capacitance  $C_{dyn}$  is defined as a ratio of sheath charge  $q_s$  over its potential.

In the corona model proposed in [31], a simple coaxial structure is adopted to make it more straightforward the calculation of radial corona currents. Instead of the thin wire model, this coaxial arrangement assumes a central and outer conductor even if the corona does not exist. The radial extension of the corona sheath increases

with increasing potential applied at the central conductor. For the reason that the corona behavior is well analyzed by Cooray, the coaxial arrangement, which is just for mathematical simplicity at first, is no longer used in this thesis. The derivation of  $C_{dyn}$  in this thesis is addressed based on the assumption of the thin-wire model, which does not need the outer conductor. The assumption is the same as Coorays that that electric field is uniformly distributed inside the corona sheath [31], and is equal to the breakdown value. This is in coincidence with the experimental observation. The formula of  $C_{dyn}$  is derived in Appendix F. It is expressed with total charge  $Q$ , the summation of core and sheath charges  $q_c$  and  $q_s$ , as follows:

$$C_{dyn}(x,t) = \begin{cases} 0 & \text{for } Q \leq q_c \\ \frac{Q}{q_c p_c + (Q - q_c) p_s} - C_i(x,t) & \text{for } Q > q_c \end{cases} \quad (4.5)$$

where both  $p_c$  and  $p_s$  are the coefficients of potential associated with core and sheath charges, respectively. As these coefficients are determined core and sheath radii, they vary with time and position on the channel. In (4.5) core charge  $q_c$  is equal to  $2\pi\epsilon_0 r_c E_c$  where  $E_c$  is the breakdown electric field. Thus  $q_c$  is the critical charge that maintains the corona sheath surrounding the core. With (4.5) the dynamic evolution of the corona sheath is modeled. This can reflect how the corona sheath radius expansion synchronously with the deposited charge along the whole channel. Because of the spacing variation of  $C_{dyn}(z, t)$  along the channel, a lightning channel with a varying radius of corona sheath is formulated.

The proposed evaluation method for  $C_{dyn}(z, t)$  is shown in Appendix F.

## 4.2 The Integrated Model

It is known in the previous sections that the lightning channel is represented with a non-linear and time-variant distributed circuit, and the ground structure is represented with a partial electrical equivalent circuit. Note that the potential in these circuits is the potential with reference to the infinity. These two circuits can be integrated, and connected in series via a voltage source.

### 4.2.1 Introduction of the integrated model

The PEEC model is generally solved by using the modified node analysis (MNA). The matrix equation is given as follows:

$$\begin{bmatrix} -\mathbf{A} & -\mathbf{R}-\mathbf{L}\partial/\partial t \\ \mathbf{P}^{-1}\partial/\partial t & \mathbf{A}^T \end{bmatrix} \begin{bmatrix} \mathbf{V} \\ \mathbf{I} \end{bmatrix} = \begin{bmatrix} \mathbf{V}_s \\ \mathbf{I}_s \end{bmatrix} \quad (4.6)$$

where  $A$  is the incident matrix of the assembled network, and  $R$ ,  $L$ , and  $P$  are the resistance, inductance, and potential coefficient matrices, respectively.

It is noted that the DC model is described by the telegraph equations as shown in (4.1). With the discretization in space, the following equations are obtained,

$$\begin{aligned} V_k^n - V_{k+1}^n &= L_{ch}(z,t) \frac{\partial I_k^n}{\partial t} + R_{ch}(t) I_k^n \\ I_k^n - I_{k+1}^n &= C_{ch}(z,t) \frac{\partial V_k^n}{\partial t} \end{aligned} \quad (4.7)$$

where  $z = n\Delta z$ . Here, the subscript  $ch$  represents the lightning channel. From (4.6) a matrix equation is obtained, as follows:

$$\begin{bmatrix} -\mathbf{A}_{ch} & -\mathbf{R}_{st} - \mathbf{L}_{ch}(z,t)\partial/\partial t \\ \mathbf{C}_{ch}(z,t)\partial/\partial t & \mathbf{A}_{ch}^T \end{bmatrix} \begin{bmatrix} \mathbf{V}_{ch}^n \\ \mathbf{I}_{ch}^n \end{bmatrix} = \begin{bmatrix} \mathbf{V}_s \\ \mathbf{I}_s \end{bmatrix} \quad (4.8)$$

where  $\mathbf{V}_{ch}^n$  and  $\mathbf{I}_{ch}^n$  are the vectors of node potentials and branch currents for all segments in the channel. Note that this matrix equation is similar to the equation in the PEEC model.

By integrating (4.6) and (4.8), a general MNA matrix equation is obtained, as follows:

$$\begin{bmatrix} \mathbf{A} & -\mathbf{R}-\mathbf{L}/\Delta t \\ \mathbf{C}/\Delta t & \mathbf{A}^T \end{bmatrix} \begin{bmatrix} \mathbf{V}^n \\ \mathbf{I}^n \end{bmatrix} = \begin{bmatrix} \mathbf{V}_s \\ \mathbf{I}_s \end{bmatrix} \quad (4.9)$$

where resistance, inductance, and capacitance matricide are given by

$$\mathbf{R} = \begin{bmatrix} \mathbf{R}_{ch} & \mathbf{0} \\ \mathbf{0} & \mathbf{R}_{st} \end{bmatrix}$$

$$\mathbf{L} = \begin{bmatrix} \mathbf{L}_{ch} & \mathbf{0} \\ \mathbf{0} & \mathbf{L}_{st} \end{bmatrix}$$

$$\mathbf{C} = \begin{bmatrix} \mathbf{C}_{ch} & \mathbf{0} \\ \mathbf{0} & \mathbf{P}_{st}^{-1} \end{bmatrix}$$

It is known that in the PEEC model the inductive and capacitance coupling from external sources has to be taken into consideration. It is noted again that the coupling effect is weak if those sources are away from the circuit of concern. Thus, the coupling effect from the lower part of DC is included in the proposed model. Both  $\mathbf{L}$  and  $\mathbf{C}$  matrices will then be updated with additional mutual inductance and capacitance.

In the problem presented in the previous section, the ground object is subject to a lightning stroke. Because of the interaction between the lightning channel and ground object, a simple hard current source is not appropriate to study the lightning current within the structure as well as the lightning channel. A voltage source then is introduced at the attachment point, as shown in Fig. 4.1(b). The source voltage is determined in such a way that the lightning current at the attachment point generally has the same waveform as the given lightning return stroke current.

The voltage source is comprised of two components, i.e.,  $V_{s1}(t)$  and  $V_{s2}(t)$ .  $V_{s1}(t)$  is applied to enforce the return stroke current  $I_0$  to be injected into the structure. It is determined by the input impedance  $Z_{st}$  of the structure, as follows:

$$V_{s1}(t) = F^{-1}[Z_{st}(\omega) \cdot I_0(\omega)] \quad (4.10)$$

where  $\omega$  is the angular frequency, and  $F^{-1}$  is the inverse Fourier transform. The procedure for evaluating  $Z(\omega)$  is detailed in [117].  $V_{s2}(t)$  is applied to enforce an assigned waveform for the incident current  $I_0$  at channel base. Because the channel is modeled as a nonlinear distributed circuit, the procedure in [117] is not applicable. Therefore, it is evaluated by applying  $I_0$  directly at the channel base without the structure being connected. Note that this input waveform is termed as an “undisturbed” waveform by researchers in [118]. This “undisturbed” waveform does not involve the reflection waves from the ground. By adding the voltage source  $V_s$ , the given “undisturbed” current waveform can be obtained.

#### 4.2.2 Time-domain solution of the system

The MNA matrix equation for a complete system is built in the previous section. For finding a time-domain circuit solution, the differential equation in (12) is discretized in time by using the backward Euler method. Because the channel radii vary with the current there, the MNA matrix contains nonlinear elements, particularly the channel capacitance. The solution of (4.10) can be obtained by using the enhanced march on-in-time technique. Consider channel resistance, inductance, capacitance are the parameters varying slowly with time. These parameters are assumed constant at each time interval. At the time from  $t$  to  $t + \Delta t$ , the equations for branch current through inductance and node potential upon capacitance are written as:

$$\begin{aligned} L_{ch}(t) \frac{\partial I(t)}{\partial t} &\approx L_{ch}(t) \frac{I(t + \Delta t) - I(t)}{\Delta t} \\ C_{ch}(t) \frac{\partial V(t)}{\partial t} &\approx C_{ch}(t) \frac{V(t + \Delta t) - V(t)}{\Delta t} \end{aligned} \quad (4.11)$$

Then, by writing (4.11) into (4.9) in a matrix format, the discrete equation of the iterative solution yields,

$$\begin{bmatrix} \mathbf{A} & -\mathbf{R}(t - \Delta t) - \frac{\mathbf{L}(t - \Delta t)}{\Delta t} \\ \frac{\mathbf{C}(t - \Delta t)}{\Delta t} & \mathbf{A}^T \end{bmatrix} \begin{bmatrix} \mathbf{V}^n \\ \mathbf{I}^n \end{bmatrix} = \begin{bmatrix} \mathbf{V}_s - \frac{\mathbf{L}(t - \Delta t)}{\Delta t} \mathbf{I}^{n-1} \\ \frac{\mathbf{C}(t - \Delta t)}{\Delta t} \mathbf{V}^{n-1} \end{bmatrix}$$

It is noted in (4.4) that the channel capacitance is determined by the instantons value of channel charge  $Q$ . According to the current continuity equation for a wire, total charge  $Q$  at time  $t$  and height  $z$  is evaluated with

$$Q(z, t) = - \int_h^H \frac{\partial I(z, t)}{\partial z} dz \quad (4.12)$$

After evaluating the charge, the nonlinear sheath potential coefficient, and then the total equivalent potential coefficient can be obtained with (4.4) and (4.5). The calculation flowchart is illustrated in Fig. 4.3

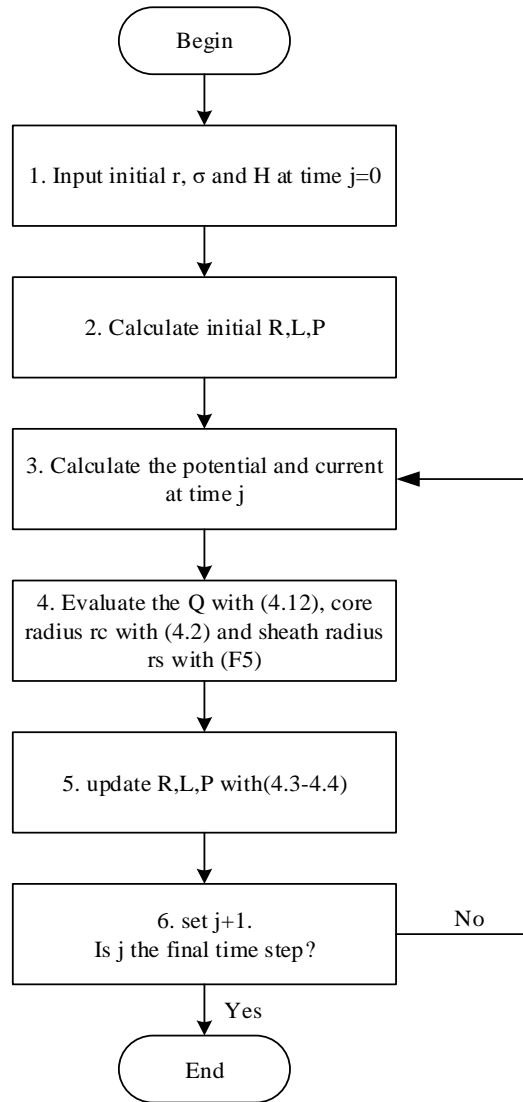


Fig. 4.3 Flowchart for solving the MNA matrix equation

#### 4.2.3 Model Validation

In this section, the proposed model is validated by the electric field and current distribution observed by the measurement.

The Typical electric field observation result is obtained from [119]. As shown in Fig.4.4, the vertical electric field at distance 1, 2, 10, 15, 50, and 200km are measured by authors in [119]. The solid line is the date of the first return stroke and the dashed line is the date of the subsequent return stroke.

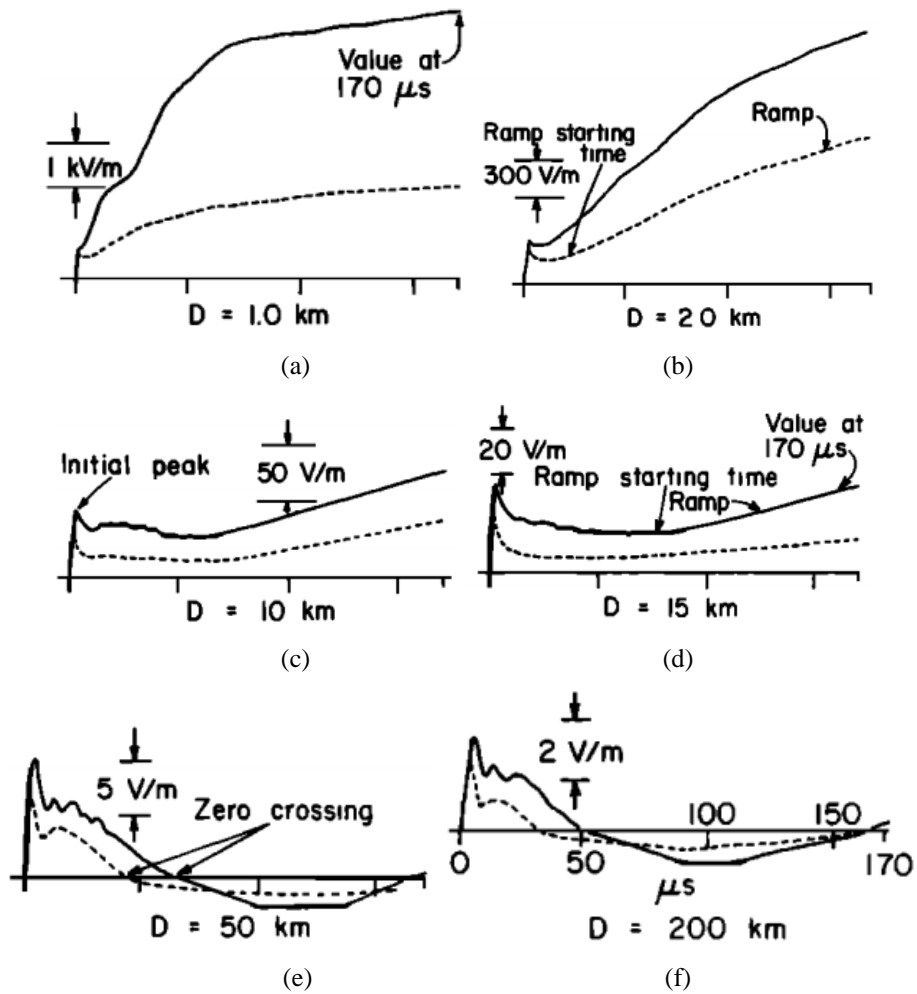
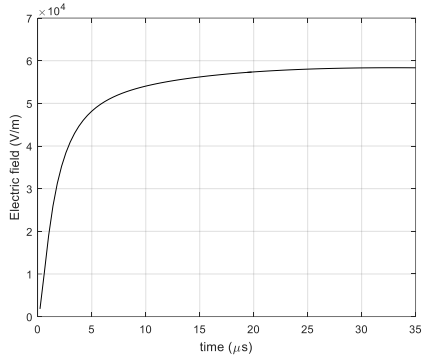


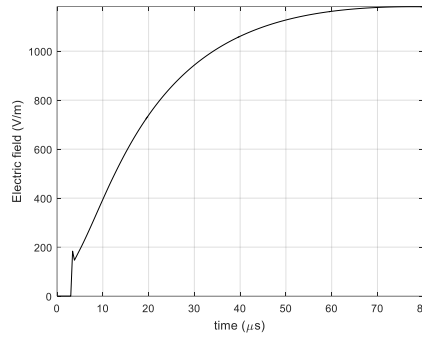
Fig.4.4 Typical vertical electric field intensity

It is noted in [120] that the typical characteristics of observed electric fields can be summarised and shown below:

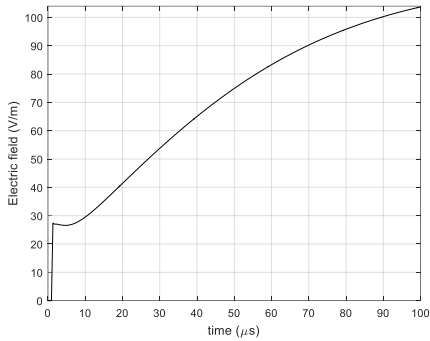
- (a) The sharp initial peak at 5 km and 100 km.
- (b) Flattening of the electric field measured at 50m.
- (c) Slow ramp after the initial peak at 5 km.
- (d) Zero crossing in the tail of field waveforms at 100km.



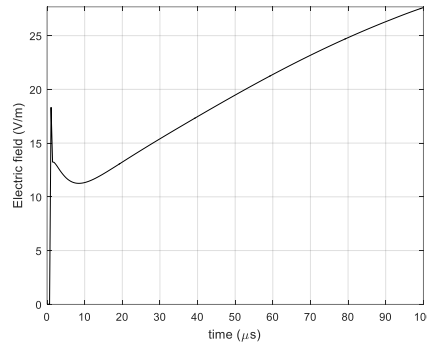
(a) D=50m



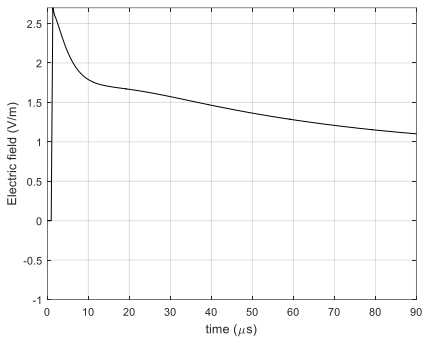
(b) D=1km



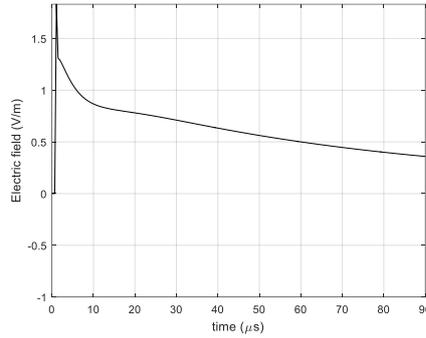
(c) D=5km



(d) D=10km



(e) D=50km



(f) D=100km

Fig.4.5 Calculated electric field with the proposed model

The calculated electric field at distance  $D=50\text{m}$ ,  $1\text{km}$ ,  $5\text{km}$ ,  $10\text{km}$ ,  $50\text{km}$ , and  $100\text{km}$  are shown in fig.4.5(a-f). In fig.4.5(a) the electric field goes flatten at the distance of  $50\text{m}$ , this is in coincidence with the measurement observation. In Fig.4.5(b), the close distance electric field has an initial peak. After that, the current rises with an approximate ramp and then goes flatten. In Fig.4.5(c-d) are the intermediate distance electric field, shows an initial peak at  $d=5\text{km}$ . Then the slow ramp after the initial peak. In Fig.4.5(e-f) are the far-field electric field, the initial peak value is observed at a distance of  $100\text{km}$ . However, zero-crossing is not found

in the calculated electric field. It is mentioned in [121] that not all the measured electric field shows a zero-crossing characteristic.

The measurement data obtained in [30] is the lightning channel on the 553m height CN tower. The source current waveform was specified to match the initial rising portion of the measured current waveform, with the tail portion being set to match that of the measured current waveform disregarding the multiple reflections.  $I_{01} = 6.5 \times 10^3$ ,  $k_0 = 0.845$ ,  $\tau_1 = 0.07 \times 10^{-6}$ ;  $\tau_2 = 2 \times 10^{-6}$ ;  $I_{02} = 5.1 \times 10^3$ ;  $\tau_3 = 70 \times 10^{-6}$ ;  $\tau_4 = 4 \times 10^{-6}$ . The similar specified current waveform can be found in [117] with the antenna model and is written as the following expression:

$$I(t) = \frac{I_{01}}{k_0} \frac{t^2/\tau_1^2}{1+t^2/\tau_1^2} e^{t/\tau_2} + I_{02}(e^{-t/\tau_3} - e^{-t/\tau_4}) \quad (4.13)$$

The current source waveform is shown in Fig.4.6.

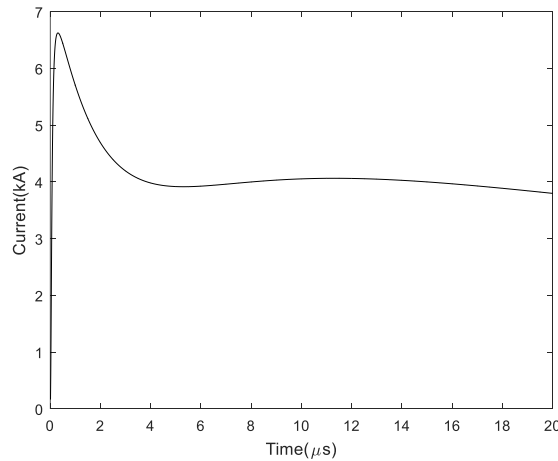


Fig.4.6 The source current waveform using Heidler's function that was used to obtain the voltage source in this simulation.

In this simulation, the initial core radius is set to be 1mm, and the core conductivity  $\sigma = 3 \times 10^4$ .  $\sigma$  is in the range of lightning channel conductivities estimated by authors in [91]. The breakdown electric field is selected as 2MV/m corresponding to the model in [92-93]. A  $\phi 10$ cm vertical conductor with a skypod is set on the top of a tower with a height of 330m, the same as the model proposed in [30]. The low frequency and low current grounding resistance are set to be 30 Ohm in this simulation.

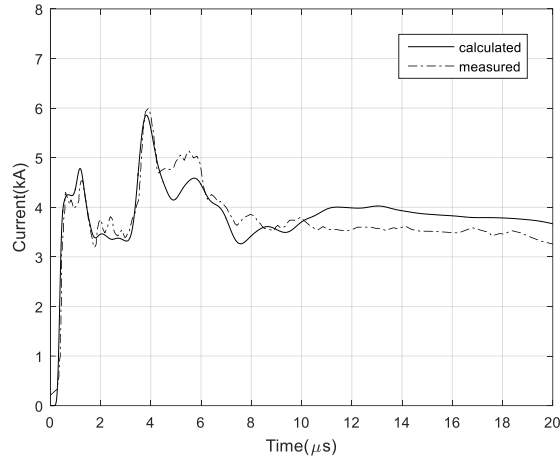


Fig.4.7 Measured and calculated current at 80m beside the top of the tower.

The simulation result can be seen in Fig.4.7. The measured data is obtained from the experience in [30]. The calculation result matches the measured data well. The reflection from the skypod and the reflection of the ground can be seen from Fig. 4.7.

The current distribution along the lightning channel is shown in Fig.6. The obvious distortion and attenuation of current are observed which are in coincidence with the scattering theory in [38]. With the inclusion of the corona sheath, the propagation speed of current along the channel changes from  $2/3$  to  $1/3$  light speed with height increasing, which is coincidence with the measurement value [120].

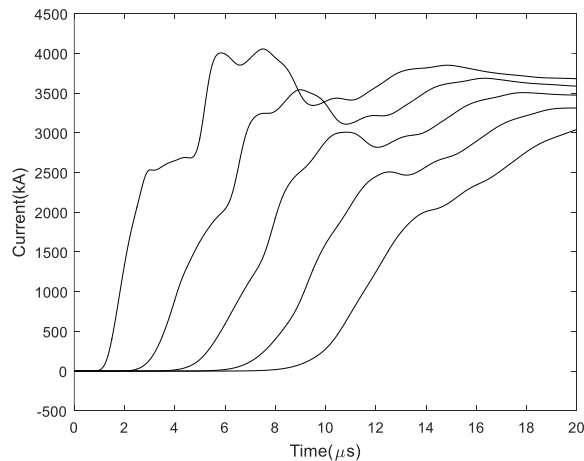


Fig.4.8 The current distribution along lightning channel 600m, 900m, 1200m, 1500m, and 1800m height.

## 4.3 Applications

### 4.3.1. Lightning Strikes on a Commercial Building

The PEEC-based lightning channel on a typical commercial building is shown below. The building is 100m high. In the existing models for the lightning strike, a lightning channel is represented by the simple resistance, which is equal to the channel surge impedance, the value of which is often provided from the range between  $400 \Omega$  and  $2000 \Omega$  [120]. It is often recommended to adopt the lower value of the lightning channel impedance for lightning currents having high values and vice versa. This resistance is connected in parallel to the above mentioned ideal current source. In the following simulation, the calculation result is based on the proposed lightning channel model. The simulated results are compared with those obtained from the simplified models.

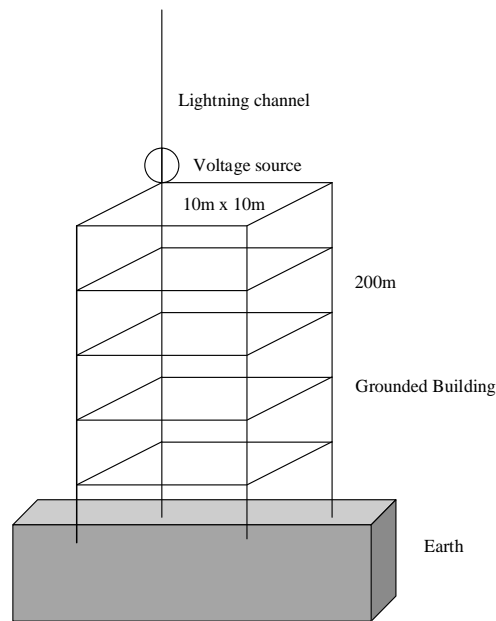


Fig.4.9 The typical building integrated with the lightning channel model

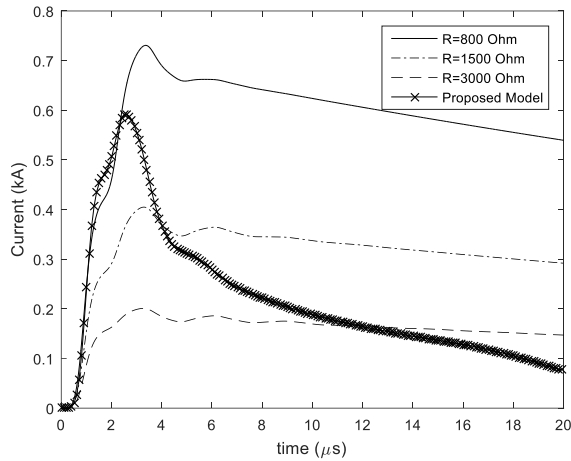


Fig.4.10 The current distribution at the top of the building

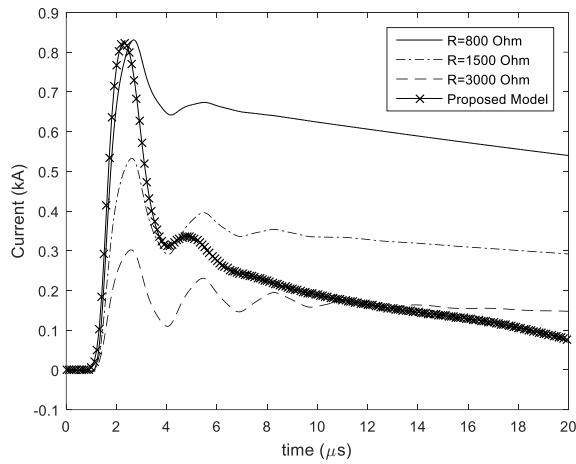


Fig.4.11 The current distribution at the bottom of the building

Both Fig.4.10 and Fig.4.11 show the currents at the top and the bottom of the cage structure of a building. The voltage source is added at the top of the building which generates a  $1/50 \mu\text{s}$  Heilder current. The channel is either represented by the proposed model or by the lumped resistance  $R=800, 1500, \text{ or } 3000 \text{ Ohm}$ . It is found out in Fig.9 and Fig.10 that the proposed method predicts a current with obvious fluctuation at the initial time. This is similar to the channel model with large lumped resistance. With the time increasing, the fluctuation of current, obtained by the proposed method, damps quickly. This is in coincidence with the behavior of small lumped resistance. From the view of fluctuation of the channel, the dynamic behavior of corona sheath and channel core is assembled to a nonlinear resistance decreasing with time quickly.

On the other hand, when considering the dynamic behavior of the corona sheath and channel core, the current obtained by the proposed model attempts to drop faster than the lumped resistance model.

#### 4.3.2. Lightning Strikes on a wind turbine

A typical wind turbine system is shown below. The modeling details of the blade and tower model are shown in [121]. The wind tower is 80m high and the length of the blade is 50m. Thus, the tip of the total wind turbine is about 130m from the ground. This thesis mainly discusses the influence of the lightning channel model on the potential along the wind turbine.

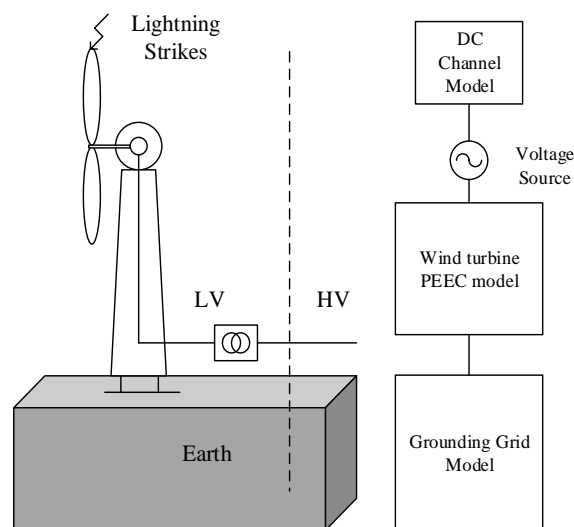


Fig.4.12 The modeling of lightning strikes on a wind turbine system

Fig.4.13 and Fig.4.14 show respectively the potentials at the tip and bottom of the wind turbine calculated with the lightning channel model with constant resistance  $R=400, 800, \text{ and } 1600\text{Ohm}$  respectively, and the proposed model. It is found that the rising part and peak value are nearly the same for the proposed model and the  $R=400$  lightning channel resistance model. But the reflection can be seen in the proposed model, which is like the  $R=800$  lightning channel resistance model. This means that the channel resistance is time-variant. To model both the peak potential and the fluctuation, the constant resistance model is not adequate. However, the potential at the bottom of the wind turbine is not much influenced by the channel model. This is coincidence with the experiment result that the ground reflection coefficient is not influenced by the top structure of the ground structure [93].

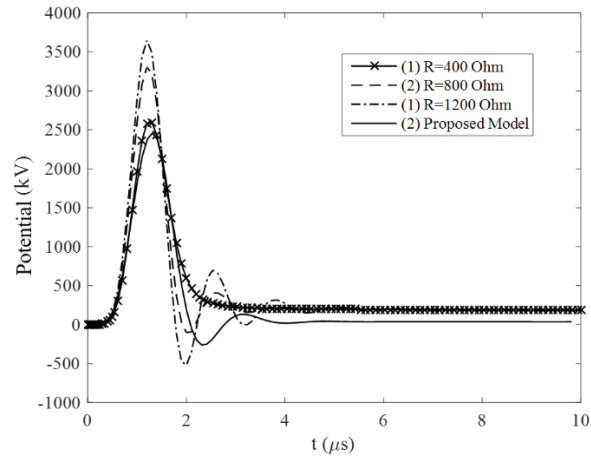


Fig.4.43 Calculation results for modeling the lightning channel with constant resistance or proposed model. The potential at the tip of the wind turbine.

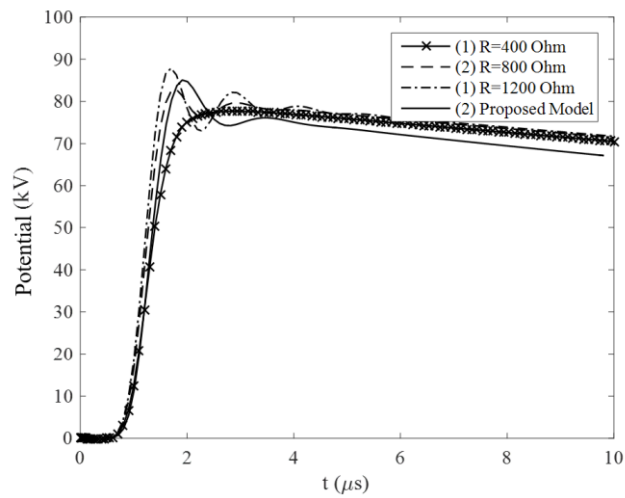


Fig.4.14 Calculation results for modeling the lightning channel with constant resistance or proposed model. The potential at the bottom of the wind turbine.

Fig.4.15 shows the comparison results between the proposed model and the channel model with an ideal current source, which is also a widely adopted channel model. It can be seen in Fig.4.15 that the strong fluctuation can be found if the channel model has infinite resistance. Meanwhile, the peak value is significantly overestimated because of the oscillation.

Fig.4.16 and Fig.4.17 show the influence of the breakdown electric field and the channel initial radius on the potential on the wind turbine. It is found out that both the breakdown electric field and initial core radius have nearly non-influence on the potential on the wind turbine.

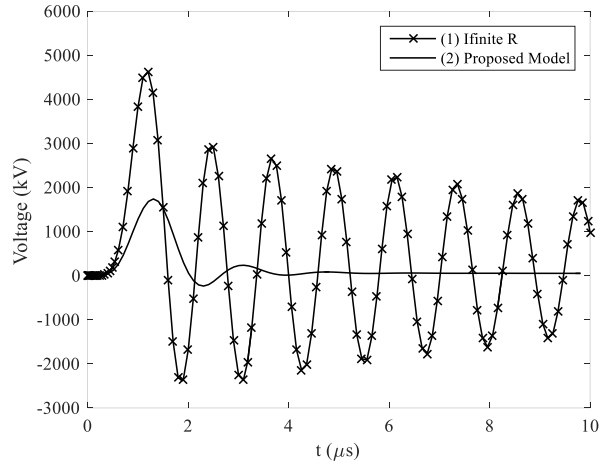


Fig.4.15 Calculation results for modeling the lightning channel with infinite resistance or proposed model. The potential at the tip of the wind turbine.

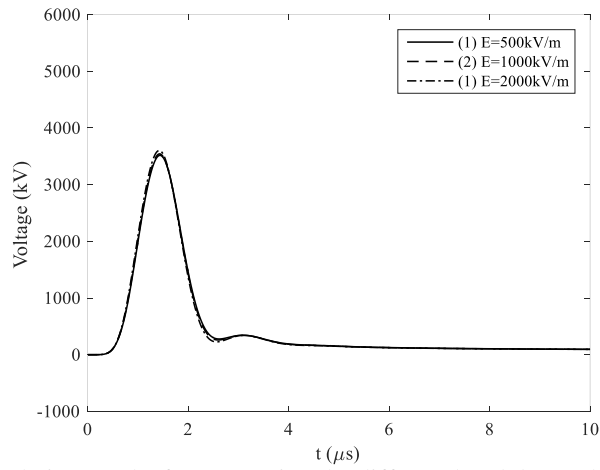


Fig.1.16 Calculation results for comparing the different breakdown electric field values.

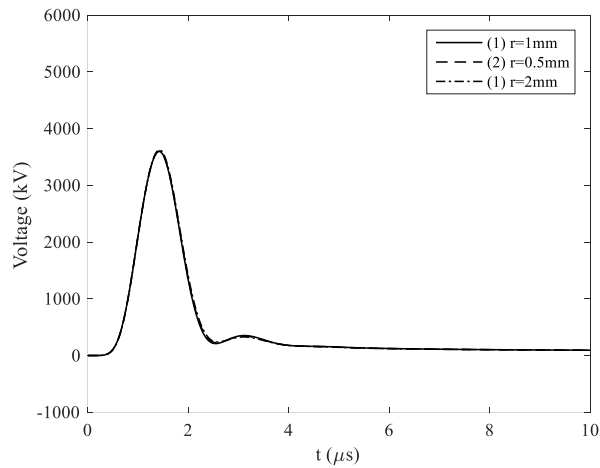


Fig.4.17 Calculation results for comparing the different initial core radius value.

## 4.4 Conclusions

In this chapter, a novel integrated model for lightning channel and ground structures is proposed. It is based on the distributed circuit (DC) model and partial equivalent element circuit (PEEC) method. The dynamic behavior of the corona sheath is included in the integrated model. As the dynamic corona discharge involves significant nonlinear behavior, the piecewise-linearization (PL) method combined with the march-on-in technique is used to solve the modified-nodal-analysis (MNA) matrix of PEEC.

It is found out that the breakdown electric field and initial radius of the lightning channel have little influence on the current and potential distribution of the striking object. However, the lumped resistance of the lightning channel will influence the waveform of the lightning current at the tip of the striking object. The equivalent impedance of the lightning channel is nonlinear and varies with time. It is not enough and accurate to be expressed by a simple constant resistance.

# 5 Conclusions and Future work

## 5.1 Conclusions

In Chapter 3, the extended time-domain-traveling-wave (TDTW) theory is introduced. Similar to the traditional traveling wave theory, it is used to describe the propagation of non-transverse-electromagnetic-mode (non-TEM) waves. The overall mathematical expression is simple and accurate. This theory can be used in a typical dipole antenna with a lumped loading technique or a ground multi-level stage tower. Once the current distribution is obtained with the closed-form expression, both the radiated electromagnetic field of antenna or lightning striking object can be computed quickly. From the view of lightning protection, the proposed TDTW theory can be used to build a more general and reasonable engineering model. From the view of antenna design, it can be used to fast calculate the input impedance and radiation pattern of long wire antenna with lumped loading technique.

In Chapter 4, a novel integrated model for lightning channel and ground structures is proposed. It is based on the distributed circuit (DC) model and partial equivalent element circuit (PEEC) method. The dynamic behavior of the corona sheath is included in the integrated model. As the dynamic corona discharge involves significant nonlinear behavior, the piecewise-linearization (PL) method combined with the march-on-in technique is used to solve the modified-nodal-analysis (MNA) matrix of PEEC. The influence of the parameters of the lightning channel on the current and potential distribution of the ground structures is discussed. The situation is based on lightning strikes on a commercial house and the wind turbine.

## 5.2 Future Work

The following issues should be settled:

- 1) For transient analysis in a complicated ground structure, it is also necessary to study the modeling of both conductors above the and under the ground, including grounding grids, buried cables, and others. A complete model for these conductors needs to be developed.

2) To expand the application of the PEEC method, it would be necessary to develop a model for interconnects linking both wires and long wires. The short wires are modeled by the PEEC method, while the long wires can be represented using the transmission line equations. Therefore, lightning analysis in a more complicated wire structure could be possible.

3) More research work needs to be carried out for the application of the PEEC method in other areas, such as lightning transient analysis in railway stations, radio base stations, wind turbines, solar power plants, etc.

# Reference

- [1] M. A. Uman, *Lightning* (Advanced physics monograph series), McGraw-Hill Book 1969
- [2] G. Maslowski and V.A. Rakov, "A study of the lightning channel corona sheath," *J. Geophys. Res.*, Vol. 111, D14110, doi:10.1029/2005 JD006858, 2006
- [3] IEEE SA-998: Guide for Direct Lightning Stroke Shielding of Substations, 2012
- [4] Y. Xu and M. Chen, "A 3-D self-organized leader propagation model and its engineering approximation for lightning protection analysis," *IEEE Trans. on PWRD*, vol. 28, no. 4, pp. 2342–2355, Oct. 2013
- [5] P. Chowdhuri, "Lightning induced voltages on multiconductor overhead lines." *IEEE Trans on PWRD*, 1990, 5(2):658~667.
- [6] Yutthagowith, P., Ametani, A., Nagaoka, N., & Baba, Y "Application of the partial element equivalent circuit method to analysis of transient potential rises in grounding systems." *IEEE Trans on EMC* 53.3 (2011): 726-736
- [7] Antonini, Giulio, S. Cristina, and Antonio Orlandi. "PEEC modeling of lightning protection systems and coupling to coaxial cables." *IEEE Trans on EMC* 40.4 (1998): 481-491
- [8] F. Rachidi, W. Janischewskyj, A. M. Hussein, C. A. Nucci, S. Guerrieri, B. Kordi and J. S. Chang. "Current and electromagnetic field associated with lightning-return strokes to tall towers." *IEEE Transactions on EMC* 43.3 (2001): 356-367. Application of the antenna theory model to a tall tower struck by lightning
- [9] B. Kordi, R. Moini, W. Janischewskyj, A. M. Hussein, V. O. Shostak and V. A. Rakov. "Application of the antenna theory model to a tall tower struck by lightning." *JGR: Atmospheres* 108.D17 (2003).
- [10] Clavel, E., Roudet, J., Feuerharmel, A. K. H., de Luca, B., Gouichiche, Z.,

- & Joyeux, P. "Benefits of the ground peec modeling approach—example of a residential building struck by lightning". *IEEE Transactions on EMC*, 61(6), 1832-1840, (2019).
- [11] Ruehli A E. "An Integral Equation Equivalent Circuit Solution to a Large Class of Interconnect Systems," Ph. D Thesis. University of Vermont, 1972.
- [12] Ruehli A E and Brennan P A. "Efficient Capacitance Calculations for Three-dimensional Multiconductor Systems," *IEEE Trans. on Microwave Theory And Techniques*, vol. 21, no. 2, 1973, pp.76-82
- [13] Ruehli, A. "Equivalent Circuit Models for Three-Dimensional Multiconductor Systems," *IEEE Transactions on Microwave Theory and Techniques*, vol. 22, no. 3, 1974, pp.216-221.
- [14] Wolff PK and Ruehli A E. "Inductance Computations for Complex Three Dimensional Geometries," In *Proc. of the IEEE Int. Symp. on Circuits and Systems*, 1981, pp. 16-19.
- [15] Heeb H and Ruehli A E. "Approximate Time-domain Models of Three-dimensional Interconnects," In *Proc. of the IEEE Int. Conf. on Computer Design*, 1990, pp. 201-205.
- [16] R. E. Collin, "Field Theory of Guided Waves". New York, NY, USA: McGraw-Hill, 1960.
- [17] K. A. Michalski and D. Zhang, "Electromagnetic scattering and radiation by surfaces of arbitrary shape in layered media, Part I: Theory," *IEEE Tran. AP*, vol.38, no. 3, pp. 335-344, Mar. 1990.
- [18] R. Qi, Y. Du, and M. Chen. "A Full-Wave PEEC Model of Thin-Wire Structures Above the Lossy Ground." *IEEE Transactions on EMC* (2019).
- [19] Y. Du, and M. Chen. "Influence of building structures on the lightning return stroke current." *IEEE transactions on power delivery* 25.1 (2009): 307-315.
- [20] K. Tanabe, A. Asakawa, M. Sakae, M. Wada, and H. Sugimoto, "Verifying the computational method of transient performance with respect to

grounding systems based on the FD–TD method,” *IEEJ Trans. Power Energy*, vol. 123, no. 3, 2003, pp. 358–367 (in Japanese).

- [21] Y. Baba, N. Nagaoka, and A. Ametani, “Modeling of thin wires in a lossy medium for FDTD simulation,” *IEEE Trans. Electromagn. Compat.*, vol. 47, no. 1, 2005, pp. 54–60
- [22] M. Akbari, K. Sheshyekani, A. Pirayesh, F. Rachidi, M. Paolone, A. Borghetti, and C.A. Nucci, “Evaluation of lightning electromagnetic fields and their induced voltages on overhead lines considering the frequency dependence of soil electrical parameters,” *IEEE Trans on EMC*, vol. 55 no. 6, 2013, pp. 1210-1219
- [23] Denno, K. “Computation of electromagnetic lightning response using moments of method. *IEEE Transactions on Magnetics*,” vol. 20, no. 5, 1984, pp.1953-1955.
- [24] Nguyen T T , Holt R . “Lightning protection of transmission lines: optimal shielding design procedure,” *IEE Proceedings-Generation, Transmission and Distribution*, vol. 150, no. 6, 2003, pp.659-0.
- [25] Banjanin, M., Savić, M. and Stojković, Z. “Lightning protection of overhead transmission lines using external ground wires,” *Electric Power Systems Research*, vol. 127, 2015, pp.206-212.
- [26] C. A. Nucci, S. Guerrieri, M. T. Correia de Barros, and F. Rachidi, “Influence of corona on the voltages induced by nearby lightning on overhead distribution lines,” *IEEE Trans. Power Del.*, vol. 15, pp. 1265–1273, 2000.
- [27] M., Grzegorz, and V. A. Rakov. "A study of the lightning channel corona sheath." *Journal of Geophysical Research: Atmospheres* 111.D14 (2006).
- [28] F. Heidler, “Traveling current source model for LEMP calculation,” in *Proc. Int. Symp. on EMC, Zurich, Switzerland, 1985*, vol. 29F2, pp. 157–162.
- [29] D. Conti, A. Fernando, H. Silveira, and S. Visacro. "A study on the influence of corona on currents and electromagnetic fields predicted by a nonlinear lightning return-stroke model." *Journal of Geophysical Research:*

Atmospheres 119.9 (2014): 5142-5156.

- [30] Kordi, B., Moini, R., Janischewskyj, W., Hussein, A. M., Shostak, V. O., & Rakov, V. A. "Application of the antenna theory model to a tall tower struck by lightning." *Journal of Geophysical Research: Atmospheres* 108.D17 (2003).
- [31] V. Cooray, "Charge and voltage characteristics of corona discharges in a coaxial geometry," *IEEE Trans. Dielectr. Electr. Insul.*, vol. 7, pp. 734–743, 2000.
- [32] V. Cooray, and T. Nelson. "Pulse propagation along transmission lines in the presence of corona and their implication to lightning return strokes." *IEEE transactions on antennas and propagation* 56.7 (2008): 1948-1959.
- [33] R. B. Raysaha, U. Kumar, and R. Thottappillil. "A macroscopic model for first return stroke of lightning." *IEEE transactions on electromagnetic compatibility* 53.3 (2011): 782-791.
- [34] S. Visacro, and A. Soares. "HEM: A model for simulation of lightning-related engineering problems." *IEEE Transactions on power delivery* 20.2 (2005): 1206-1208.
- [35] L. Baker, Return-stroke transmission line model, In *Lightning Electromagnetics*, edited by R. L. Gardner, pp. 63–74, Hemisphere, New York, 1990.
- [36] C. E. Baum, C. E. and L. Baker, Analytic return-stroke transmission-line model, In *Lightning Electromagnetics*, edited by R. L. Gardner, pp. 17–40, Hemisphere, New York, 1990.
- [37] D. Conti, A. Fernando, H. Silveira, and S. Visacro. "Lightning strikes to tall objects: A study of wave interactions at the return-stroke front using a nonlinear transmission line model." *Journal of Geophysical Research: Atmospheres* 120.13 (2015): 6331-6345.
- [38] Baba, Y. and V. A. Rakov (2005), On the mechanism of attenuation of current waves propagating along a vertical perfectly conducting wire above ground: Application to lightning, *IEEE Trans. Electromagn. Compat.*, 47(3), 105

- [39] D. Pavanello, F. Rachidi, W. Janischewskyj, M. Rubinstein, A. M. Hussein, E. Petrache, V. Shostak, I. Boev, C. A. Nucci, W. A. Chisholm, M. Nyffeler, J. S. Chang and A. Jaquier. "On return stroke currents and remote electromagnetic fields associated with lightning strikes to tall structures: 1. Computational models." *Journal of Geophysical Research: Atmospheres* 112.D13 (2007).
- [40] F. Rachidi, V. A. Rakov, C. A. Nucci and J. L. Bermudez. "Effect of vertically extended strike object on the distribution of current along the lightning channel." *Journal of Geophysical Research: Atmospheres* 107.D23 (2002): ACL-16.
- [41] J. L. Bermudez, M. Rubinstein, F. Rachidi, F. Heidler and M. Paolone. "Determination of reflection coefficients at the top and bottom of elevated strike objects struck by lightning." *Journal of Geophysical Research: Atmospheres* 108.D14 (2003).
- [42] Y. Baba And V. A. Rakov, "On The Mechanism of Attenuation of Current Waves Propagating Along a Vertical Perfectly Conducting Wire Above Ground: Application To Lightning," *IEEE Trans on EMC*, Vol. 47, No. 3, Pp. 521–532, Aug. 2005.
- [43] L. Greev, and R. Farhad. "On tower impedances for transient analysis." *IEEE Transactions on PWRD* 19.3 (2004): 1238-1244.
- [44] R. Lundholm, R. B. Finn, and W. S. Price, "Calculation of transmission line lightning voltages by field concepts," *Trans. Amer. Inst. Electr. Eng. Part III, Power App. Syst.*, vol. 76, pp. 1271–1281, 1957.
- [45] A. Shoory, F. Vega, P. Yutthagowith, F. Rachidi, Rubinstein, Y. Baba and A. Ametani., "On the mechanism of current pulse propagation along conical structures: Application to tall towers struck by lightning," *IEEE Trans. Electromagn. Compat.*, vol. 54, no. 2, pp. 332–342, Apr. 2012.
- [46] J. Takami, T. Tsuboi, and S. Okabe, "Measured distortion of current waves and electrical potentials with propagation of a spherical surge in an

electromagnetic field," IEEE Trans. Electromagn. Compat., vol. 52, no. 3, pp. 753–756, Aug. 2010.

- [47] C. A. Jordan, "Lightning Computation for Transmission Line with Ground Wires," General Electric Review, vol. 34, 1934, pp. 180-185
- [48] R. Lundholm, R. B. Finn, W. S. Price, "Calculation of Transmission Line Lightning Voltages by Field Concepts," Power Apparatus and Systems, Part III. Transactions of the American Institute of Electrical Engineers, vol. 76, pp. 1271-1281, 1957.
- [49] C. F. Wagner and A. R. Hileman, "A New Approach to Calculation of Lightning Performance of Transmission Lines-Ii," Power Apparatus and Systems, Part III." Transactions of the American Institute of Electrical Engineers, vol. 78, 1959, pp. 996-1020
- [50] M. A. Sargent and M. Darveniza, "Tower Surge Impedance," IEEE Trans. on PAS, vol. PAS-88, 1969, pp. 680-687
- [51] H. Motoyama and H. Matsubara, "Analytical and experimental study on surge response of transmission tower," IEEE Trans. on Power Delivery, vol. 15, 2000, pp. 812-819
- [52] K.C Chen, "Transient Response of an Infinite Cylindrical antenna," IEEE Trans. on AP, vol. 31, no. 1, Jan. 1983, pp. 170-172
- [53] R.K. Pokharel and M. Ishii, "Applications of Time-Domain numerical Electromagnetic Code to Lightning Surge Analysis," IEEE Trans. on EMC, Vol 49 No. 3, August 2007, pp 623-631.
- [54] Y. Baba and M. Ishii, "Numerical Electromagnetic Field Analysis of Lightning Current in tall Structures," IEEE Trans. on PWRD, Vol 16 no. 2, April 2001, pp.324-328
- [55] P. Yutthagowith, A. Ametani, F. Rachidi, N. Nagaoka, Y. Baba, "Application of a partial element equivalent circuit method to lightning surge analyses," EPSR, Vol. 94, 2013, pp. 30–37
- [56] Y. Du, W. Xinghua, and C. Mingli, "Numerical investigation of transient

surge impedance of a vertical conductor over a perfect ground," *EPSR*, vol. 94, 2013, pp. 106–112

- [57] Xinghua Wang, Y. Du, Mingli Chen, Xiaohong Huang, "Surge behavior at the discontinuity of a vertical line over the ground," *EPSR*, Vol. 113, 2014, pp. 129–133
- [58] Grcev and F. Rachidi, "On tower impedances for transient analysis," *IEEE Trans. on Power Delivery*, vol. 19, pp. 1238-1244, 2004.
- [59] G. D. Breuer, A. J. Schultz, R. H. Scholomann, W. S. Price, "Field Studies of the Surge Response of a 345-Kv Transmission Tower and Ground Wire," *AIEE Trans. on PAS, Part III*, vol. 76, 1957, pp. 1392-1396
- [60] R. W. Caswell, I. B. Johnson, E. F. Koncel, N. R. Schultz, "Lightning Performance of 138-kV Twin-Circuit Transmission Lines of Commonwealth Edison Company - Operating Experience and Field Studies," *AIEE Trans. on PAS, Part III*, vol. 76, 1957, pp. 1480-1489
- [61] M. Kawai, "Studies of the Surge Response on a Transmission Line Tower," *IEEE Trans. on PAS*, vol. 83, 1964, pp. 30-34
- [62] A. De Conti, S. Viscaro, A. Soares, Jr. and M. Schroeder, "Revision, Extension, and Validation of Jordan's Formula to Calculate the Surge Impedance of Vertical Conductors," *IEEE Trans. on EMC*, Vol 48 no. 3, August 2006, pp. 530-536
- [63] Y. Baba and V. A. Rakov, "On the mechanism of attenuation of current waves propagating along a vertical perfectly conducting Wire above ground: application to lightning," *IEEE Trans. on EMC*, vol. 47, 2005, pp. 521-532
- [64] A. Shoory, F. Vega, P. Yutthagowith, F. Rachidi, M. Rubinstein, Y. baba, V. A. Rakov, K. Sheshyekani, A. Ametani, "On the Mechanism of Current Pulse Propagation along Conical Structures: Application to Tall Towers Struck by Lightning," *IEEE Trans. on EMC*, vol. 2011, pp. 1-11
- [65] J. Takami, T. Tsuboi, S. Okabe, "Measured Distortion of Current Waves and Electrical Potentials with Propagation of a Spherical Surge in an Electromagnetic Field," *IEEE Trans. on EMC*, vol. 52, 2010, pp. 753-756

- [66] C. Menemenlis and C. Zhu Tong, "Surge Propagation on Nonuniform Lines," IEEE Trans. on PAS, vol. PAS-101, 1982, pp. 833-839
- [67] "Guide to Procedures for Estimating the Lightning Performance of Transmission Lines," CIGRE SC33-WG01 Report, 1991
- [68] J. D. Kraus and K. R. Carver "Electromagnetics", p485-489, second edition, 1984.
- [69] S. Tkatchenko, R. Farhad, and I. Michel. "Electromagnetic field coupling to a line of finite length: Theory and fast iterative solutions in frequency and time domains." IEEE Transactions on EMC 37.4 (1995): 509-518.
- [70] Y. Du and Y. Ding, "Lightning surge propagation on a single conductor in free space," IEEE Trans. on EMC, vol. 59 no. 1, 2017, pp.119-127
- [71] T. Noda and S. Yokoyama, "Thin wire representation in finite difference time domain surge simulation," IEEE Trans. on PWRD, vol. 17, 2002, pp. 840-847
- [72] Y. Du, Xinghua Wang and Mingli Chan, "Circuit Parameters of Vertical Wires above a Lossy Ground in PEEC Models," IEEE Trans. on EMC vol. 54 no. 4, 2012, pp. 871-879
- [73] Xinghua Wang, Y. Du, Mingli Chen and Xiaohong Huang, "Surge behavior at the discontinuity of a vertical line over the ground", EPSR, vol. 113, 2014, pp. 129-133.
- [74] A. Ametani, N. Nagaoka, Y. Baba and T. Ohno, Power system transients: theory and applications, CRC Press, 2013
- [75] Liao, Yi, Todd H. Hubing, and Donglin Su. "Equivalent circuit with frequency-independent lumped elements for coated wire antennas." IEEE Trans on AP, vol. 60 no.11, 2012, pp. 5419-5423.
- [76] K. Chen, "Transient response of an infinite cylindrical antenna." IEEE Trans on AP vol. 31, no.1, 1983, pp. 170-172.
- [77] T. Hara, And O. Yamamoto. "Modelling of A Transmission Tower For Lightning-Surge Analysis." IEE Proceedings-Generation, Transmission And

Distribution 143.3 (1996): 283-289.

- [78] T. Yamada, A. Mochizuki, J. Sawada, E. Zaima, T. Kawamura, A. Ametani and S. kato. "Experimental Evaluation of A UHV Tower Model For Lightning Surge Analysis." IEEE Trans on PWRD 10.1 (1995): 393-402.
- [79] W. A. Chisholm, Y. L. Chow, And K. D. Srivastava. "Lighting Surge Response Of Transmission Towers." IEEE Trans on PAS 9 (1983): 3232-3242.
- [80] J. A. Martinez and F. Castro-Aranda. "Tower modeling for lightning analysis of overhead transmission lines." IEEE Power Engineering Society General Meeting, 2005. IEEE, 2005.
- [81] F. Rachidi, W. Janischewskyj, A. M. Hussein, C. A. Nucci, S. Guerrieri, B. Kordi and J. S. Chang. "Current and electromagnetic field associated with lightning-return strokes to tall towers." IEEE Transactions on EMC 43.3 (2001): 356-367. Application of the antenna theory model to a tall tower struck by lightning
- [82] B. Kordi, R. Moini, W. Janischewskyj, A. M. Hussein, V. O. Shostak and V. A. Rakov. "Application of the antenna theory model to a tall tower struck by lightning." JGR: Atmospheres 108.D17 (2003).
- [83] C.F. Wagner and A.R. Hileman, "A new approach to the calculation of the lightning performance of transmission lines – Part III," AIEEE Trans. Part III, vol. 79, no. 3, pp. 589-603, October 1960.
- [84] M.A. Sargent and M. Darveniza, "Tower surge impedance," IEEE Trans. on Power Apparatus and Systems, vol. 88, no. 3, pp. 680-687, May 1969.
- [85] W.A. Chisholm, Y.L. Chow and K.D. Srivastava, "Travel time of transmission towers," IEEE Trans. on Power Apparatus and Systems, vol. 104, no. 10, pp. 2922-2928, October 1985.
- [86] A. Ametani et al., "Frequency-dependent impedance of vertical conductors and a multiconductor tower model," IEE Proc.-Gener. Transm. Distrib., vol. 141, no. 4, pp. 339-345, July 1994.

- [87] T. Hara and O. Yamamoto, "Modelling of a transmission tower for lightning surge analysis," *IEE Proc.-Gener. Transm. Distrib.*, vol. 143, no. 3, pp. 283-289, May 1996.
- [88] J.A. Gutierrez et al., "Nonuniform transmission tower model for lightning transient studies," *IEEE Trans. on PWRD*, vol. 19, no. 2, pp. 490-496, April 2004.
- [89] Y. Baba and M. Ishii, "Numerical electromagnetic field analysis on lightning surge response of tower with shield wire," *IEEE Trans. On PWRD*, vol. 15, no. 3, pp. 1010-1015, July 2000.
- [90] T. Ito et al., "Lightning flashover on 77-kV systems: Observed voltage bias effects and analysis," *IEEE Trans. on PWRD*, vol. 18, no. 2, pp. 545-550, April 2003.
- [91] M. Srdjan, and J. Cvetic. "Conductivity of a lightning-channel corona sheath during return stroke." *IEEE transactions on plasma science* 37.6 (2009): 750-758.
- [92] G. Maslowski, and V. A. Rakov. "A review of recent lightning corona sheath dynamics research." 2011 7th Asia-Pacific International Conference on Lightning. IEEE, 2011.
- [93] J. Cvetic and P. Osmokrovic. "Dynamics of lightning discharge during return stroke." *IEEE transactions on plasma science* 37.1 (2008): 4-14.
- [94] H. C. Pocklington, "Electrical oscillations in wires," *Proc. Cambridge Phil. Soc.*, vol. 9, no. 7, pp. 324-332, 1897.
- [95] E. Hallén, *Theoretical investigations into the transmitting and receiving qualities of antennae*. Stockholm, Sweden: Almqvist & Wiksells, 1938.
- [96] R. W. P. King, *The theory of linear antennas: with charts and tables for practical applications*. Cambridge, MA, USA: Harvard Univ. Press, 1956.
- [97] E. Hallén, "Properties of a long antenna," *J. Appl. Phys.*, vol. 19, no. 12, pp. 1140-1147, 1948.

- [98] Kibret, Behailu, Assefa K. Teshome, and Daniel TH Lai. "A new perspective on the cylindrical antenna theory." *IEEE Trans on AP*, 64.7 (2016): 2981-2988.
- [99] Wu, T., and R. King. "The cylindrical antenna with nonreflecting resistive loading." *IEEE Trans on AP* 13.3 (1965): 369-373.
- [100] Nyquist, D., and Kun-Mu Chen. "The traveling-wave linear antenna with nondissipative loading." *IEEE Trans on AP*, 16.1 (1968): 21-31.
- [101] Esselle, Karu P., and Stanislaw S. Stuchly. "Pulse-receiving characteristics of resistively loaded dipole antennas." *IEEE Trans on AP* 38.10 (1990): 1677-1683.
- [102] Shlivinski, Amir, Ehud Heyman, and Raphael Kastner. "Antenna characterization in the time domain." *IEEE Trans on AP* 45.7 (1997): 1140-1149.
- [103] G. Franceschetti and C. H. Papas, "Pulsed antennas," *IEEE Trans. Antennas Propagat.*, vol. AP-22, pp. 651–661, Sept. 1974.
- [104] M. Sato, M. Iguchi, and R. Sato, "Transient response of coupled linear dipole antennas," *IEEE Trans on AP*, vol. AP-32, pp. 133–140, Feb. 1984.
- [105] D. M. Pozar, R. E. McIntosh, and S. G. Walker, "The optimum feed voltage for a dipole antenna for pulse radiation," *IEEE Trans on AP*, vol. AP-31, pp. 563–569, July 1983.
- [106] Y. W. Kang and D. M. Pozar, "Optimization of pulse radiation from dipole array for maximum energy in specified time interval," *IEEE Trans on AP*, vol. AP-34, pp. 1383–1386, Dec. 1986
- [107] Liao, Yi, Todd H. Hubing, and Donglin Su. "Equivalent circuit for dipole antennas in a lossy medium." *IEEE Trans on AP* 60.8 (2012): 3950-3953.
- [108] Liao, Yi, Todd H. Hubing, and Donglin Su. "Equivalent circuit with frequency-independent lumped elements for coated wire antennas." *IEEE Trans on AP*, vol. 60 no.11, 2012, pp. 5419-5423.

- [109] K. Chen, "Transient response of an infinite cylindrical antenna." IEEE Trans on AP vol. 31, no.1, 1983, pp. 170-172.
- [110] Y. Ding, Y. Du, and M. Chen. "Lightning surge propagation on a grounded vertical conductor." IEEE Transactions on EMC 60.1 (2017): 276-279.
- [111] F. Heidler. Traveling current source model for LEMP calculation. in Proc. 6th Int. Zurich Symp. EMC, Zurich, Switzerland, 1985:157~162.
- [112] Y. Du, B. Li and M. Chen, "The Extended Thin-Wire Model of Lossy Round Wire Structures for FDTD Simulations," in IEEE Transactions on PWRD, vol. 32, no. 6, pp. 2472-2480, Dec. 2017.
- [113] B. Li, Y. Du and M. Chen, "Thin-wire Models for Inclined Conductors with Frequency-dependent Losses," in IEEE Transactions on PWRD
- [114] A. De Conti, F. H. Silveira, and S. Visacro. "A study on the influence of corona on currents and electromagnetic fields predicted by a nonlinear lightning return-stroke model." Journal of Geophysical Research: Atmospheres 119.9 (2014): 5142-5156.
- [115] S. I. Braginskii, "Theory of the development of a spark channel", Sov. Phys. JETP, 34, 1068–1074, 1958.
- [116] N. Theethayi and V. Cooray, "On the representation of the lightning return stroke as a current pulse propagating along a transmission line", IEEE Trans. Power Del., 20(2), 823–837, 2005.
- [117] R. Moini, , B. Kordi, Gh. Z. Rafi, and V. A. Rakov, "A new lightning return stroke model based on antenna theory", J. Geophys. Res., 105, 29,693– 29,702, 2000.
- [118] A. Mosaddeghi, F. Rachidi, M. Rubinstein, et al. "Radiated fields from lightning strikes to tall structures: Effect of upward-connecting leader and reflections at the return stroke wavefront". IEEE transactions on electromagnetic compatibility, 2011, 53(2): 437-445.
- [119] F. H. Heidler. "Review and Extension of the TCS Model to Consider the Current Reflections at Ground and at the Upper End of the Lightning

Channel." IEEE Transactions on Electromagnetic Compatibility 61.3 (2019): 644-652.

[120] V. A. Rakov and M. A. Uman, "Review and evaluation of lightning return stroke models including some aspects of their application", IEEE Trans. EMC, 40(4), 403–426, 1998.

[121] A. Rafael, et al. "A comprehensive analysis of the effect of frequency-dependent soil electrical parameters on the lightning response of wind-turbine grounding systems." *Electric Power Systems Research* 175 (2019): 105927.

# Appendix

## Appendix A The Relationship between Current and Scalar Potential

The difference between potential  $\phi(z, t)$  at position  $z$  and time  $t$  and  $\phi(z_0, t)$  at position  $z_0$  and time  $t$  is the integral of vector potential as mentioned in (3.1), that is,

$$\phi(z, t) - \phi(z_0, t) = \int_z^{z_0} \frac{\partial}{\partial t} A_z(l, t) dl \quad (A1)$$

where reference position  $z_0$  is selected in such a way that the surge has not arrived at that point yet, that is,  $z_0 > ct$ . Therefore, potential  $\phi(z_0, t)$  is identically zero. Alternatively,  $z_0$  can be located at the infinity to which a virtual wire is extended from the conductor.

Note that two current surges propagate upwards and downwards on the conductor, respectively, as shown in Fig. 3.2(b). Assume that at time  $t$  the two surges arrive at  $ct$  on the lower segment of the conductor, and  $-ct$  on the upward segment. Potential  $\phi(z, t)$  in (A1) can be then expressed by

$$\phi(z, t) = \frac{\mu_0}{4\pi} \int_z^{ct} \left( \frac{\partial}{\partial t} \int_{-ct}^{ct} \frac{I(l', t - \frac{|l-l'|}{c})}{\sqrt{(l-l')^2 + r^2}} dl' \right) dl \quad (A2)$$

where  $l$  and  $l'$  are respectively the variables of integration along the conductor for scalar potential and vector potential. Potential  $\phi(z, t)$  is identically zero if  $z > ct$  (travel distance of the surge at time  $t$ ).

Considering there is no current attenuation on the conductor, the retarded current is expressed by

$$I(l', t - \frac{|l-l'|}{c}) = I(0, t - \frac{|l'|}{c} - \frac{|l-l'|}{c}) \quad (A3)$$

It is noted that the retarded time of  $t - |l'|/c - |l-l'|/c$  must be greater than zero at any point and any moment. The following inequalities yield

$$\begin{aligned}
ct &> l - 2l' \quad \text{for } l' < 0 \\
ct &\geq l + 2l' \quad \text{for } l' \geq 0
\end{aligned}
\tag{A4}$$

The upper and lower limits of variable  $l'$  can be worked out from (A4). Then potential  $\phi(z, t)$  in (A2) reduces to

$$\phi(z, t) = \frac{\mu_0}{4\pi} \cdot \int_z^{ct} \frac{\partial}{\partial t} \int_{\frac{l-ct}{2}}^{\frac{l+ct}{2}} \frac{I(0, t - \frac{|l'|}{c} - \frac{|l-l'|}{c})}{\sqrt{(l-l')^2 + r^2}} dl' dl
\tag{A5}$$

## Appendix B Lossless Propagation of Potentials

Note that the longitudinal  $E$  field is zero on a perfect conductor. In the  $n$ -dipole line model given in Fig. 3.2(a), both vector potential  $A_{xM}$  and scalar potential  $\phi_{xM}$  ( $x = a, b$  or  $b$ ) on the line satisfy the following equation,

$$\partial\phi_{xM}(z,t)/\partial z = -\partial A_{xM}(z,t)/\partial t \quad (\text{B1})$$

With Lorenz gauge, the following is obtained,

$$\begin{aligned} \partial\phi_{xM}(z,t)/\partial t &= -c^2 \nabla \cdot A_{xM}(z,t) \\ &= -c^2 \partial A_{xM}(z,t)/\partial z \end{aligned} \quad (\text{B2})$$

Note that (B1) and (B2) formulate a pair of coupled 1<sup>st</sup> order differential equations similar to the well-known telegrapher's equations. Then, the corresponding solution for the vector potential is given by [27]:

$$A_{xM}(z,t) = f_1(ct - z) + f_2(ct + z) \quad (\text{B3})$$

Under the zero initial condition, integrating (B3) along the time axis yields

$$\begin{aligned} \phi_{xM}(z,t) &= -c^2 \int_0^t \partial A_{xM}(z,t)/\partial z dt \\ &= c^2 \int_0^t [\partial f_1/c \partial t - \partial f_2/c \partial t] dt \\ &= cf_1(ct - z) - cf_2(ct + z) \end{aligned} \quad (\text{B4})$$

Thus, for a wave propagating in one direction, these vector potential and scalar potential satisfies:

$$\phi_{xM}(z,t) = cA_{xM}(z,t) \quad (\text{B5})$$

## Appendix C Wave Propagation in a Dipole Line Structure with Different Radius

The vector potential  $A_x$  on a single dipole line with the radius  $r_x$  shown in Fig. 3.17(c) is given by:

$$A_x(z,t) = \frac{\mu_0 c}{4\pi} \int_{(z-ct)/2}^{(z+ct)/2} \frac{I_x(|l'|, t_{d2})}{\sqrt{\Delta l'^2 + r_x^2}} dl' \quad (C1)$$

Note that the current can be written, using the attenuation coefficient, as  $I_x(|l'|, t_{d1}) = I_s(0, t_{d2})\alpha_x(|l'|, t_{d1})$  [26] and  $t_{d2} = t - |l' - z|/c$ . Then, the total vector potential  $A_x$  on a line structure in Fig. 3.17(c) is

$$A_x(z,t) = \frac{\mu_0}{4\pi} \int_{(z-ct)/2}^{(z+ct)/2} \frac{I_{s,0}(t_{d1})\alpha_x(|l'|, t_{d1})}{\sqrt{(l' - z)^2 + r_x^2}} dl' \quad (C2)$$

Now we replace  $\alpha_x(|l'|, t_{d1})$  in the integral of (C2) with  $\alpha_x(z, t) + [\alpha_x(|l'|, t_{d1}) - \alpha_x(z, t)]$ . According to the Bogerd's derivation for a finite antenna [33], the integral containing  $[\alpha_x(|l'|, t_{d1}) - \alpha_x(z, t)]$  is neglected. The remaining integral can be evaluated analytically under the assumption that  $(ct - z)^2 \gg r^2$ . Thus, the final expression for the total vector potential in (C2) is given as,

$$A_x(z,t) = I_{bM}(z,t) \frac{\mu_0}{2\pi} \left( \frac{z}{ct - z} \ln \frac{ct + z}{\sqrt{z^2 + r_x^2} + z} + \ln \frac{\sqrt{c^2 t^2 - z^2}}{r_x} - 1 \right) \quad (C3)$$

The corresponding transient impedance of the line structure in stage x is obtained as follows:

$$Z_x(z,t) = \frac{\mu_0 c}{2\pi} \left( \frac{z}{ct - z} \ln \frac{ct + z}{\sqrt{z^2 + r_x^2} + z} + \ln \frac{\sqrt{c^2 t^2 - z^2}}{r_x} - 1 \right) \quad (C4)$$

## Appendix D Wave Propagation in a Multiple Dipole Line Structure

To obtain characteristic equations for waves in a multiple dipole line structure shown in Fig. 3.27(a), the current in dipole line 1 is decomposed into two components, i.e.,  $-(n-1)I_{b1}$  and  $nI_{b1}$  as seen in Fig. 3.27(b) and 3.27(c). Therefore, there are  $n$  pairs of dipole lines or  $n$  transmission lines with dipole line 1 being the reference, as illustrated in Fig. 3.27(b). Each pair of the dipole lines carries two equal but opposite currents. In Fig. 3.27(c), there is one dipole line alone carrying the current of  $nI_{b1}$ . Note that all these currents are characterized by the same attenuation coefficient  $\alpha_{bM}(z, t)$ .

Now consider a pair of dipole lines 1 and  $i$  with spacing  $D_{b,1i}$ , as shown in Fig.3.27(b). These dipole lines are closely spaced and carry equal but opposite currents. The vector potential  $A_{DM}$  contributed by this pair of differential-mode currents is given in [32]:

$$A_{DM}(\rho, z, t) = \int I_{bM}(l', t_{d1})g(\rho, l', z)dl' \quad (D1)$$

$$g(\rho, \Delta l') = 1/\sqrt{\Delta l'^2 + \rho^2} - 1/\sqrt{\Delta l'^2 + (\rho - D_{b,1i})^2}$$

Where,  $\Delta l' = l' - z$  and the Green's function in [32]

$g(\rho, \Delta l') = 1/\sqrt{\Delta l'^2 + \rho^2} - 1/\sqrt{\Delta l'^2 + (\rho - D_{b,1i})^2}$  by neglecting the retardation time over the spacing distance between closely spaced dipole lines.

According to the symmetry,  $A_{DM}(r_b, z, t)$  can also be regarded as the vector potential difference between position  $(r_b, z)$  and  $(D_{b,1i}, z)$  caused by only one of the pair currents. Then, with Ampere's law, the vector potential resulting from a pair of dipole lines with the opposite currents is given by

$$\begin{aligned} A_{DM}(r_b, z, t) &= \int_{r_b}^{D_{b,1i}} B(r, z, t)dr \\ &\approx \frac{\mu_0}{2\pi n} \ln\left(\frac{D_{b,1i}}{r_b}\right) I_{bM}(z, t) \end{aligned} \quad (D2)$$

Vector potential  $A''_{b1}$  in Fig. 3.27(c) is contributed by the current on a single dipole line with a radius  $r_b$ . According to [26], it is expressed by

$$A''_{b1}(z, t) = \frac{\mu_0}{4\pi} \int_{(z-ct)/2}^{(z+ct)/2} \frac{I_{bM}(|l'|, t_{d1})}{\sqrt{(l' - z)^2 + r_b^2}} dl' \quad (D3)$$

where  $t_{d1} = t - |l' - z|/c$ .

Note that the current can be written, using the attenuation coefficient, as  $I_{bM}(|l'|, t_{d1}) = I_s(0, t_{d2})\alpha_{bM}(|l'|, t_{d1})$  [26] and  $t_{d2} = t - |l' - z|/c$ . Then, the total vector potential  $A_{bM}$  on an  $n$ -dipole line structure in Fig. 27(a) is obtained by summing both (D2) and (D3), as follows:

$$\begin{aligned} A_{bM}(z, t) &= A_{DM}(z, t) + A''_{b1}(z, t) \\ &= \frac{\mu_0}{4\pi} \int_{(z-ct)/2}^{(z+ct)/2} \frac{I_{s,0}(t_{d1})\alpha_{bM}(|l'|, t_{d1})}{\sqrt{(l' - z)^2 + r_b^2}} dl' - \\ &\quad I_{bM}(z, t) \frac{\mu_0}{2\pi n} \sum_{i=1}^n \ln\left(\frac{D_{i1}}{r_b}\right) \end{aligned} \quad (D4)$$

Now we replace  $\alpha_{bM}(|l'|, t_{d1})$  in the integral of (D3) with  $\alpha_{bM}(z, t) + [\alpha_{bM}(|l'|, t_{d1}) - \alpha_{bM}(z, t)]$ . According to the Bogerd's derivation for a finite antenna [33], the integral containing  $[\alpha_{bM}(|l'|, t_{d1}) - \alpha_{bM}(z, t)]$  is neglected. The remaining integral can be evaluated analytically under the assumption that  $(ct - z)^2 \gg r^2$ . Thus, the final expression for the total vector potential in (D4) is given as,

$$\begin{aligned} A_{bM}(z, t) &= I_{bM}(z, t) \frac{\mu_0}{2\pi n} \sum_{i=1}^n \ln\left(\frac{D_{i1}}{r_b}\right) + I_{bM}(z, t) \cdot \\ &\quad \frac{\mu_0}{2\pi} \left( \frac{z}{ct - z} \ln \frac{ct + z}{\sqrt{z^2 + r^2} + z} + \ln \frac{\sqrt{c^2 t^2 - z^2}}{r} - 1 \right) \end{aligned} \quad (D5)$$

Thus, the analytical expression for transient impedance can be obtained as

$$\begin{aligned} Z_{bM}(z, t) &= \frac{\phi_{bM}(z, t)}{I_{bM}(z, t)} = \frac{cA_{bM}(z, t)}{I_{bM}(z, t)} \\ &= Z_b(z, t) - \frac{\mu_0 c}{2\pi n} \sum_{i=1}^n \ln\left(\frac{D_{i1}}{r_b}\right) \end{aligned} \quad (D6)$$

where

$$Z_b(z, t) = \frac{\mu_0 c}{2\pi} \left( \frac{z}{ct - z} \ln \frac{ct + z}{\sqrt{z^2 + r^2} + z} + \ln \frac{\sqrt{c^2 t^2 - z^2}}{r} - 1 \right)$$

It is found that under the thin-wire approximation, the transient impedance of a multi-dipole line structure is not affected by the attenuation coefficient  $\alpha_{bM}$  of current. It is fully determined by the geometry of a wire structure. This impedance can be viewed as the impedance of a standalone dipole minus a quasi-static transmission line impedance.

## Appendix E Transient Impedance of Wave Propagation in a Multi-stage tower

Consider an  $n$ -dipole line structure with a change of wire spacing at  $z = z_0$ , as illustrated in Fig. E(a). With the same technique used in Appendix D, the current in dipole line 1 is substituted by  $-(n-1)I_{x1}$  and  $nI_{x1}$  in Fig. E(b) and  $nI_{x1}$  in Fig. E(c) ( $x = a, b$ , or  $c$ ).

Similar to (D1) in Appendix D, vector potential in Stage  $x$  contributed by a pair of opposite currents shown in Fig. E(b) is expressed by

$$\begin{aligned}
 A_{DM}(r_x, z, t) &= \int_{r_x}^{D_{x,li}} B(r, z, t) dr \\
 &= \frac{\mu_0}{2\pi n} \ln\left(\frac{D_{x,li}}{r_x}\right) I_{x1}(z, t)
 \end{aligned} \tag{E1}$$

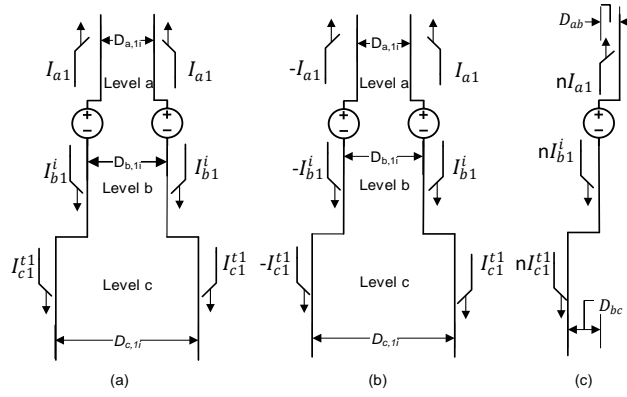


Fig. E Waves propagating in a multiple dipole line structure (a) original configuration (b)  $n$  pairs of dipole lines (c) a single dipole line

Similar to (D2), the vector potential  $A''_{x1}$  on a single dipole line with the radius  $r_x$  shown in Fig. 17(c) is given by:

$$\begin{aligned}
 A''_{xM}(z, t) &= \frac{\mu_0 c}{4\pi} \int_{(z-ct)/2}^{(z+ct)/2} \frac{I_{xM}(|l'|, t_{d2})}{\sqrt{\Delta l'^2 + r_x^2}} dl' + \\
 &\quad \frac{\mu_0 c}{4\pi} \int_{(z-ct)/2}^{(z+ct)/2} \frac{I_{yM}(|l'|, t_{d2})}{\sqrt{\Delta l'^2 + D_{xy}^2}} dl'
 \end{aligned} \tag{E2}$$

where y represents a stage other than stage x.  $D_{xy}$  is equal to  $(D_{y,ij} - D_{x,ij})/2$ .

Note that (E2) can also be written as:

$$A''_{xM}(z,t) = \frac{\mu_0 c}{4\pi} \int_{(z-ct)/2}^{(z+ct)/2} \frac{I_{xM}(|l'|, t_{d2}) + I_{yM}(|l'|, t_{d2})}{\sqrt{\Delta l'^2 + r_x^2}} dl' - \frac{\mu_0 c}{4\pi} \int_{(z-ct)/2}^{(z+ct)/2} I_{yM}(|l'|, t_{d2}) g(r_x, \Delta l') dl' \quad (E3)$$

where  $g(r_x, \Delta l')$  is the Green's function in (D1).

The total vector potential can then be obtained by summing both (E1) and (E3). The total transient impedance of the  $n$ -dipole line structure in stage x is obtained as follows:

$$Z_{xM}(z,t) = \frac{cA_{xM}(z,t)}{I_{xM}(z,t)} = Z_x(z,t) - \frac{\mu_0 c}{2\pi n} \sum_{i=1}^n \ln\left(\frac{D_{li}}{r_x}\right) + \frac{\mu_0 c}{4\pi} \int_{(z-ct)/2}^{(z+ct)/2} \frac{I_{yM}(|l'|, t_{d2})}{I_{xM}(z,t)} g(\rho, \Delta l') dl' \quad (E4)$$

Where

$$Z_x(z,t) = \frac{\mu_0 c}{2\pi} \left( \frac{z}{ct-z} \ln \frac{ct+z}{\sqrt{z^2+r_x^2}+z} + \ln \frac{\sqrt{c^2 t^2 - z^2}}{r_x} - 1 \right)$$

The integral in (E4) can be evaluated similar as (D1) and yields

$$\int_{(z-ct)/2}^{(z+ct)/2} \frac{I_{yM}(|l'|, t_{d2})}{I_{xM}(z,t)} g(\rho, \Delta l') dl' \approx \frac{I_{yM}(z,t)}{I_{xM}(z,t)} \ln\left(\frac{D_{b,li}}{r_b}\right) \quad (E5)$$

Note x and y represents different stages so that  $I_{yM}(z,t)$  is zero if observation point z belongs to the stage x. Thus, (E5) is always zero. The integral in (E4) can be removed.

Then the total transient impedance is simplified into

$$Z_{xM}(z, t) = Z_x(z, t) - \frac{\mu_0 c}{2\pi n} \sum_{i=1}^n \ln \left( \frac{D_{1i}}{r_x} \right) \quad (\text{E6})$$

The transient impedance in stage x of the tower with a discontinuity is determined by the single dipole line impedance together with the quasi-static transmission line impedance. Note that (E6) is the same as (D5).

## Appendix F The Lumped Capacitance Considering the Nonlinear and Dynamic Corona Sheath

Let  $q_c$  and  $q_s$  be the surface charge on the core and the volume charge in the sheath, respectively. Total charge  $Q$  in the channel then is equal to  $q_c$  and  $q_s$ . The electric field on the surface of the core arising from the core charge is expressed by

$$E = q_c / 2\pi\epsilon_0 r_c \quad (F1)$$

Assume that  $E_c$  is the breakdown electric field for maintaining the corona sheath. The charge on the core surface is given by

$$q_c = 2\pi\epsilon_0 r_c E_c \quad (F2)$$

Denote  $Q$  the total charge in the channel. Sheath charge  $q_s$  then is equal to. The potential of the lightning channel is contributed by both  $q_c$  and  $q_s$ , as follows:

$$\phi = q_c \cdot p_c + (Q - q_c) \cdot p_s \quad (F3)$$

Note that  $q_c = Q - q_s$ . Both  $p_c$  and  $p_s$  are the coefficients of potential  $q_c$  and  $q_s$ , respectively. They are evaluated with the integrals given below:

$$p_c = \frac{1}{4\pi\epsilon_0 \Delta l^2} \int_{z_3}^{z_4} \int_{z_1}^{z_2} \frac{1}{\sqrt{r_c^2 + (h_1 - h_2)^2}} dh_1 dh_2 \quad (F4a)$$

$$p_s = \frac{1}{4\pi\epsilon_0 \Delta l^2 (r_s - r_a)} \int_{r_a}^{r_s} \int_{z_3}^{z_4} \int_{z_1}^{z_2} \frac{\rho_s 2\pi r}{\sqrt{r^2 + (h_1 - h_2)^2}} dh_1 dh_2 dr \quad (F4b)$$

The double-line integral along the z axis is evaluated with

$$\sum_{i=1,2} \sum_{j=3,4} (\sqrt{\Delta z_{ij}^2 + r^2} - \Delta z_{ij} \ln(\Delta z_{ij} + \sqrt{\Delta z_{ij}^2 + r^2}))$$

And

$$\Delta z_{ij} = z_i - z_j$$

Assume the radial electric field is uniform within the corona sheath. The charge density in the corona sheath then varies inversely with  $r$  in the radial direction []. The outer sheath radius in (11) can be obtained by

$$r_s = Q/2\pi\epsilon_0 E_c \quad (\text{F5})$$

The equivalent potential coefficient is evaluated by

$$P(x,t) = \phi(x,t)/Q(x,t) \quad (\text{F6})$$

The capacitance is equal to the inverse of the potential coefficient, that is,

$$\begin{aligned} C(x,t) &= Q(x,t)/\phi(x,t) \\ &= \frac{Q}{q_c \cdot p_c + (Q - q_c) \cdot p_s} \end{aligned} \quad (\text{F7})$$

The dynamic capacitance due to corona sheath behavior is

$$C_{dyn}(x,t) = \frac{Q}{q_c \cdot p_c + (Q - q_c) \cdot p_s} - C_i(x,t) \quad (\text{F8})$$